THE UNIVERSITY OF CHICAGO

TOPICS IN GRAVITATIONAL LENSING OF THE COSMIC MICROWAVE BACKGROUND

A DISSERTATION SUBMITTED TO
THE FACULTY OF THE DIVISION OF THE PHYSICAL SCIENCES
IN CANDIDACY FOR THE DEGREE OF
DOCTOR OF PHILOSOPHY

DEPARTMENT OF PHYSICS

BY
PAVEL MOTLOCH

CHICAGO, ILLINOIS
AUGUST 2018

Dedicated to all my teachers throughout the ages, both formal and informal.

Amongst them, most of all to my parents.

In the beginning, the Universe was created. This made a lot of people very angry and has been widely regarded as a bad move.

Douglas Adams: The Restaurant at the End of the Universe

"Would you tell me, please, which way I ought to go from here?"

"That depends a good deal on where you want to get to," said the Cat.

"I don't much care where —" said Alice.

"Then it doesn't matter which way you go," said the Cat.

"— so long as I get *somewhere*," Alice added as an explanation.

"Oh, you're sure to do that," said the Cat, "if you only walk long enough."

Lewis Carroll: Alice's Adventures in Wonderland

With ideas it is like with dizzy heights you climb: At first they cause you discomfort and you are anxious to get down, distrustful of your own powers; but soon the remoteness of the turmoil of life and the inspiring influence of the altitude calm your blood; your step gets firm and sure and you begin to look — for dizzier heights.

Nikola Tesla: The Nikola Tesla Treasury

TABLE OF CONTENTS

LIST OF FIGURES

LIST OF TABLES

ACKNOWLEDGMENTS

Professor Hu, getting the chance to work with you is like winning a lottery. You have always been the paragon of excellence and professionality and I tried to soak up as much as possible. You showed me the importance of understanding things down to the tiniest detail, how to think about problems, how to present results in scientific papers and provided million other pieces of advice. I am infinitely grateful for everything you have done for me over the years and I cordially thank you.

Thank you Paolo for being my co-advisor for a while. You exposed me to a completely different leadership style and allowed me to gain insight into how experimentalists and experiments work, thus greatly enriching my education. Probably the most important of all, at the start of my graduate student career you gave me confidence I can be scientifically productive – who knows how the things would turn out if you did not.

Thank you LianTao. We did not communicate as often as I originally though we would, but you shared some true pearls of wisdom with me.

Thank you Professor Meyer, Professor Turner and Professor Wald for serving on my PhD committee and for providing good suggestions, especially about how to present.

Thank you to the many members of the Professor Hu's group – Silvia, Pierre, Dan, Chen, Austin, Macarena, Yin, Meng-Xiang, Andrew, Marilena, Alessandro, Vinicius, Hayato, Sam, and Marco – and Chihway and Kimmy for the camaraderie, Monday lunches and all the discussions, scientific or not.

Thank you Enrique and Jaime for your hospitality during my visit in Santiago and help.

Thank you Toshihiro for being my frequent travel companion, many of our adventures will remain cherished memories. Cinco empanadas de jamón por favor!

Thank you to all the people from the Kavli Institute for Cosmological Physics, Department of Physics and Department of Astronomy and Astrophysics for creating such a wonderful community and learning environment. And for the cookies. Thank you Ted, Helen, Aimee, Valeri, Elena and Kevin for doing all the enabling work. Thank you Stuart,

David, Tiffany and Nobuko for helping me adjust to the new educational system after my arrival. Thank you Professor Dodelson for your nuggets of advice, great class and the best cosmology book out there. Also, thank you Professor Collar for all the hilarious stories and rants, not only those about the coffee maker.

Thank you Department of Energy, National Science Foundation, National Aeronautics and Space Administration and Kavli Foundation for providing grants that made my research throughout the graduate school possible.

Thank you Matt and members of the Sophia Community for being such tremendous neighbours. Thank you 57^{th} Meeting of Friends for renting us a wonderful place I have called home for five years.

Thank you Mengfei, Tony and Zhaodi for being such great housemates and also for your polite toleration of all my quirks. Thank you Mengfei, Johnny, Tony, Albert, and my companions from the infamous 140's mafia – Kevin and Alex – for all the fun we have had over the years. And all the wood you were willing to trade for my sheep. Thank you Clai, Jungmin, Endao, Victor, Tom and Tommy for occasionally joining us.

Thank you mom, dad, Bruder and the other members of my family for your unconditional support throughout the way and all your care. You set up the best possible initial conditions for me, better than any inflation can produce. I have a feeling you did all the heavy lifting and I am just "going downhill". I could not have been born into a better family.

Finally, thank you Paula for all your encouragement and patience. Your amazing ability of always knowing how to make me laugh has pulled me out of quite a few bad moods. As they say, "some people come into our lives, leave footprints on our hearts and we are never, ever the same again." For me, you are such a person.

ABSTRACT

Gravitational lensing of the cosmic microwave background (CMB) has recently started to gain importance as a cosmological probe. With growing detection significance of this effect, it is necessary to further develop theoretical understanding of its consequences. Such studies are the main topic of this work, that is based on the papers [1, 2, 3].

We start by looking at correlations that the gravitational lensing induces between CMB temperature, polarization and reconstructed lensing potential and investigate how neglecting them in an analysis impacts constraints on cosmological parameters. We find that for the planned CMB Stage 4 experiment, neglecting these correlations can significantly underestimate variance of certain combinations of cosmological parameters, as well as lead to an increased frequency of mistakenly rejecting the underlying cosmological model.

Then we discuss a method we developed to directly measure the gravitational lensing potential from the CMB data and explain how to practically perform such measurement. This method helps us understand why it is necessary to include the lensing-induced covariances to get correct constraints on cosmological parameters. Additionally, comparing direct measurements of the lensing potential from various subsets of data or across experiments allows for powerful consistency checks that can be used to search for residual systematics and exotic new physics. When assuming a particular cosmological model, this technique can also be used to probe internal consistency of lensing within a single data set.

In the final part of this work, we apply this methodology to check lensing consistency of the Planck satellite data. We find that it is not possible to resolve the lensing anomalies seen in this data even when allowing for an arbitrary gravitational lensing potential, beyond the predictions of the standard cosmological model. Significances of these tensions are evaluated at above 2σ; one possible explanation are residual systematics in the Planck temperature power spectrum. Without large modifications, this technique can be applied to data from other current and especially future experiments, where its full power will become manifest.

CHAPTER 1

INTRODUCTION

In this chapter we aim to briefly overview the standard cosmological model, gravitational lensing of the cosmic microwave background (CMB) and how it is possible to reconstruct the gravitational lenses from the CMB power spectra data. All information in this chapter is well known and explained in more detail for example in the excellent textbook [4] and review of the gravitational lensing of the CMB [5].

1.1 ΛCDM

Various kinds of experimental evidence have lead to to the Λ cold dark matter (ΛCDM) cosmological model as the "standard model" of cosmology, that is[1] in good agreement with the available experimental data (e.g. [8, 9] and references therein).

It is based on the idea of a nearly homogeneous and isotropic Universe that has been evolving according to the laws of general relativity. On top of matter and radiation, the Universe is assumed to be filled with a mysterious "dark" energy that has recently become dominant in setting the expansion rate of the Universe [10, 11]; in ΛCDM this dark energy is just a cosmological constant Λ. As the Universe expands, the cosmic plasma, that with good precision appears to be in a thermal equilibrium early on, cools down. Because of this cooling, matter species eventually decouple from the plasma, leading to the observed abundances of heavy elements. Possibly, this is also a mechanism behind the observed abundance of the "dark matter", which in ΛCDM makes up the majority of the matter in the Universe (e.g. [8]).

The standard cosmological picture starts with an initial period of the so-called inflation (see [12] for a review), during which small inhomogeneities on top of the homogeneous

1. Up to several interesting tensions such as [6, 7] that may or may not be signs of new physics. See also Chapter 4.

background are generated by quantum effects. These perturbations have since been growing under the opposing influences of gravity and pressure, leading to the rich structure we observe in the Universe today.

While numerous cosmological probes are currently available, this work focuses on the cosmic microwave background. During the period of recombination at redshift of ≈ 1100, photons decoupled from matter and have been traversing the Universe almost freely since then. Today, we can measure CMB as a nearly perfect black-body with temperature $T_{\mathrm{CMB}} = (2.72548 \pm 0.00057)\,\mathrm{K}$ [13], nearly isotropic on the sky. The small perturbations produced by inflation imprint on the CMB as $O(10^{-5})$ anisotropies and their measurements both test the ΛCDM assumptions and constrain parameters of this model [8, 14, 15, 16].

1.2 Gravitational lensing of the CMB

As everything in the Universe, CMB photons are influenced by gravity. Traversing to us from the last scattering surface, they probe the gravitational potentials sourced by the matter between us and recombination. This way, they are sensitive to the growth of structure in the Universe and provide a new source of cosmological information that can be used to confirm or refute the ΛCDM model. The resulting photon deflections are on the order of a few arc minutes and are coherent on degree scales, which is the typical angular size of the matter structures responsible for the lensing. The current generation of the CMB experiments has achieved angular resolutions and levels of instrumental noise that can probe this effect with high statistical significance [14, 16, 17, 18, 19, 20, 21].

In the weak lensing regime we are interested in, gravitational lensing consists of remapping the unlensed temperature $\tilde{T}$ and Stokes parameters $\tilde{Q}, \tilde{U}$ into their lensed counterparts

according to

$$T(\hat{n}) = \tilde{T}(\hat{n} + \nabla\phi(\hat{n})) \tag{1.1}$$

$$Q(\hat{n}) = \tilde{Q}(\hat{n} + \nabla\phi(\hat{n})) \tag{1.2}$$

$$U(\hat{n}) = \tilde{U}(\hat{n} + \nabla\phi(\hat{n})), \tag{1.3}$$

where $\hat{n}$ is a position on the sky. The scalar field on the sphere $\phi(\hat{n})$ is called gravitational lensing potential and its gradient determines the deflections of the CMB fields. Gravitational lensing potential represents a weighted integral of the Weyl potential along the line of sight from us to the last scattering surface; its power spectrum $C_L^{\phi\phi}$ can be calculated within a considered cosmological model [5].

Information carried by the lensing potential ϕ can be recovered either by measuring its effect on the CMB power spectra, in particular the smoothing of the acoustic peaks [22] and generation of small scale B-modes, or by measuring higher point functions of the temperature and polarization maps. The latter is possible, because gravitational lensing generates a correlation between measured CMB fields and their gradients [23, 24, 25], modifying the simple Gaussian statistics of the unlensed CMB. In the next section we introduce the currently used technique to uncover lensing information from the non-Gaussian statistics of the CMB.

Because the gravitational lensing signal depends on growth of structure at low redshifts, it can be leveraged to break certain parameter degeneracies in the CMB data and used to better constrain sum of neutrino masses and other parameters in models beyond ΛCDM, such as properties of the dark energy. On the other side, B-modes generated by the gravitational lensing act as a foreground for detecting the primordial tensor modes from inflation [26].

1.3 Lensing reconstruction

As mentioned in the previous section, the non-Gaussian structure induced in the CMB by the gravitational lensing can be used to measure the lensing potential. In this section we briefly describe the ideas behind the quadratic reconstruction technique [27] that is used in the current analyses of CMB data. In the future, it will become advantageous to use improved estimators [28, 29, 30, 31]. Although the experimental data are getting to the point where polarization fields dominate the signal on reconstructed ϕ, we focus here only on the temperature-based quadratic estimator. Full details on estimators using the CMB polarization fields can be found for example in the original work [27]; the general logic behind these estimators is analogous to what is presented in this Section and our aim here is to give the reader a quick, not a complete, introduction.

Expanding the lensed CMB temperature (1.1) to the first order in the gravitational potential leads to

$$\delta T(\hat{n}) = T(\hat{n}) - \tilde{T}(\hat{n}) \approx \nabla_i \tilde{T}(\hat{n}) \nabla^i \phi(\hat{n}) + O(\phi^2). \tag{1.4}$$

Expanding all fields in the spherical harmonics and neglecting higher order terms in ϕ, we get

$$\delta T_\ell^m = \sum_{LM} \sum_{\ell' m'} \phi_L^M \tilde{T}_{\ell'}^{m'} I_{\ell L \ell'}^{m M m'}, \tag{1.5}$$

where the I symbol represents an integral over the spherical harmonics

$$I_{\ell L \ell'}^{m M m'} = \int \mathrm{d}\hat{n} Y_\ell^{m*} \nabla_i Y_L^M \nabla^i Y_{\ell'}^{m'}. \tag{1.6}$$

It is related to a Wigner 3-j symbol through

$$I_{\ell L \ell'}^{m M m'} = (-1)^m \begin{pmatrix} \ell & L & \ell' \\ -m & M & m' \end{pmatrix} F_{\ell L \ell'}, \tag{1.7}$$

where

$$F_{\ell L\ell'} = [L(L+1) + \ell'(\ell'+1) - \ell(\ell+1)]\sqrt{\frac{(2L+1)(2\ell+1)(2\ell'+1)}{16\pi}} \begin{pmatrix} \ell & L & \ell' \\ 0 & 0 & 0 \end{pmatrix}. \quad (1.8)$$

For a fixed deflection field, the temperature develops a nonzero covariance between the off-diagonal elements,

$$\left\langle T_\ell^m T_{\ell'}^{m'} \right\rangle = \sum_{LM} (-1)^M \begin{pmatrix} \ell_1 & \ell_2 & L \\ m_1 & m_2 & -M \end{pmatrix} f_{\ell_1 L \ell_2} \phi_L^M, \quad (1.9)$$

with

$$f_{\ell_1 L \ell_2} = C_{\ell_1}^{\tilde{T}\tilde{T}} F_{\ell_2 L \ell_1} + C_{\ell_2}^{\tilde{T}\tilde{T}} F_{\ell_1 L \ell_2}. \quad (1.10)$$

The most general estimator of the lensing potential that satisfies the expected rotational properties and is quadratic in the temperature field is the weighted sum of the multipole pairs

$$\hat{\phi}_L^M = N_L^{\rm qe} \sum_{\ell_1, m_1} \sum_{\ell_2, m_2} (-1)^M \begin{pmatrix} \ell_1 & \ell_2 & L \\ m_1 & m_2 & -M \end{pmatrix} g_{\ell_1 \ell_2}(L) T_{\ell_1}^{m_1} T_{\ell_2}^{m_2}, \quad (1.11)$$

with an arbitrary $g_{\ell_1 \ell_2}(L)$. In order to have an unbiased estimator in presence of a fixed ϕ field, we need

$$N_L^{\rm qe} = (2L+1) \left\{ \sum_{\ell_1 \ell_2} g_{\ell_1 \ell_2}(L) f_{\ell_1 L \ell_2} \right\}; \quad (1.12)$$

the minimal variance unbiased estimator is then the one corresponding to

$$g_{\ell_1 \ell_2}(L) = \frac{f_{\ell_1 L \ell_2}}{2 C_{\ell_1}^{TT} C_{\ell_2}^{TT}}. \quad (1.13)$$

Because of fluctuations in the unlensed CMB, the power spectrum of the estimated lensing potential has nonzero expectation value even in the absence of any lensing; this expectation value is called the $N^{(0)}$ bias. Its value is equal to $N_L^{\rm qe}$ (1.12) and in an analysis has to be

subtracted to avoid biasing the cosmological signal. In reality, one also has to address higher order biases [32]; we refer an interested reader to the original literature as detailed discussion of these biases is not directly relevant for the results of this work.

1.4 Conventions

We denote unlensed fields with a tilde, e. g. $\tilde{T}$. In the text, we usually omit the hat on top of the reconstructed lensing potential and write it simply as ϕ instead of $\hat{\phi}$, as the two can be distinguished from context.

Throughout this work we use capital letters X, Y, W, Z to represent either the CMB temperature or polarization field, i.e. an element from $\{T, E, B\}$, and lower case letters x, y, w, z to additionally include reconstructed lensing potential, i.e. an element from $\{T, E, B, \hat{\phi}\}$.

As a shorthand notation, we denote cosmological parameters of a given cosmological model as θ_A. We label $\tilde{\theta}_A$ a derived set of parameters that have the same effect on the unlensed CMB power spectra as θ_A, but do not change the lensing potential (see Section 3.1 for more details).

CHAPTER 2

LENS-SAMPLE COVARIANCE EFFECTS

Gravitational lensing correlates the lensed temperature and polarization data [32, 33]; neglecting these covariances can affect forecasts of constraining power of future experiments and analysis of their data. We start this chapter by introducing the experimental configuration considered in this and the next chapter, before summarizing an analytical model for the lensing-induced covariances and its extension that includes covariances with the reconstructed lensing potential. After detailing our analysis pipeline, we use this model to investigate how neglecting these lensing-induced covariances affects constraints on cosmological parameters.

2.1 Experimental setup

In this and the next chapter we investigate a simplified setup of a full sky experiment with specifications inspired by the proposed CMB Stage 4 (CMB-S4) experiment [26].

For the fiducial cosmology we take a flat 6 parameter ΛCDM model with minimal neutrino mass $\sum m_\nu$. For the ΛCDM parameters we take $\omega_b = \Omega_b h^2$, the physical baryon density; $\omega_c = \Omega_c h^2$, the physical cold dark matter density; n_s, the tilt of the scalar power spectrum; A_s, its amplitude; and τ, the optical depth to recombination. We choose θ_*, the angular scale of the sound horizon at recombination, as opposed to the Hubble constant h, as the sixth independent parameter. We also assume that tensor modes are negligible so that there is no unlensed B mode. Values of the cosmological parameters for the fiducial model used in this and the next chapter are summarized in Table 2.1.

For noise in temperature and polarizations, we assume a noise spectra [34]

$$N_\ell^{XY} = \Delta_{XY}^2 e^{\ell(\ell+1)\theta^2_{\rm FWHM}/8\ln 2}, \tag{2.1}$$

where Δ_{XY} is the instrumental noise (in μK-radian) and $\theta_{\rm FWHM}$ is the beam size (in radi-

Table 2.1: Fiducial parameters used in this and the next chapter

Parameter	Fiducial value
h	0.675
$\Omega_c h^2$	0.1197
$\Omega_b h^2$	0.0222
n_s	0.9655
A_s	2.196×10^{-9}
τ	0.06
$\sum m_\nu$	60 meV

ans). Throughout the text, we use capital letters X, Y, Z, W to represent either the CMB temperature or polarization field, i.e. an element from $\{T, E, B\}$. We consider a $1'$ beam, $\Delta_{TT} = 1\,\mu\mathrm{K}'$, $\Delta_{EE} = \Delta_{BB} = 1.4\,\mu\mathrm{K}'$, and $\Delta_{TE} = \Delta_{TB} = \Delta_{EB} = 0$ and consider measurements in the multipole range $\ell = 2 - 3000$.

For parts of this chapter we also assume measurements of $C_L^{\phi\phi}$ from $L = 2 - 5000$ with the reconstruction noise $N_L^{\phi\phi}$ of the minimal variance quadratic estimator [27], $N^{(0)}$ noise bias (see Section 1.3), and ignore other noise biases and trispectrum terms [32]. Comparison of the $C_L^{\phi\phi}$ with the reconstruction noise for our experiment $N_L^{\phi\phi}$ is plotted in Figure 2.1. Notice that for these specifications, the lens reconstruction is sample variance dominated for $L \lesssim 10^3$. This is one of the assumptions for our analysis of the lensing reconstruction from the CMB-S4-like experiment: that lens sample variance will in the future dominate the measurements of the lens power spectrum at low multipoles.

2.2 Lens-sample covariance

In this section, we present an analytical model describing non-Gaussian covariances between the C_ℓ^{xy} power and cross spectra observables induced by gravitational lensing through the same lenses on the sky. Here these x, y represent either the CMB temperature, polarization or reconstructed lensing potential. Covariances predicted by this model have been tested against numerical simulations in [33] for the temperature and polarization power spectra

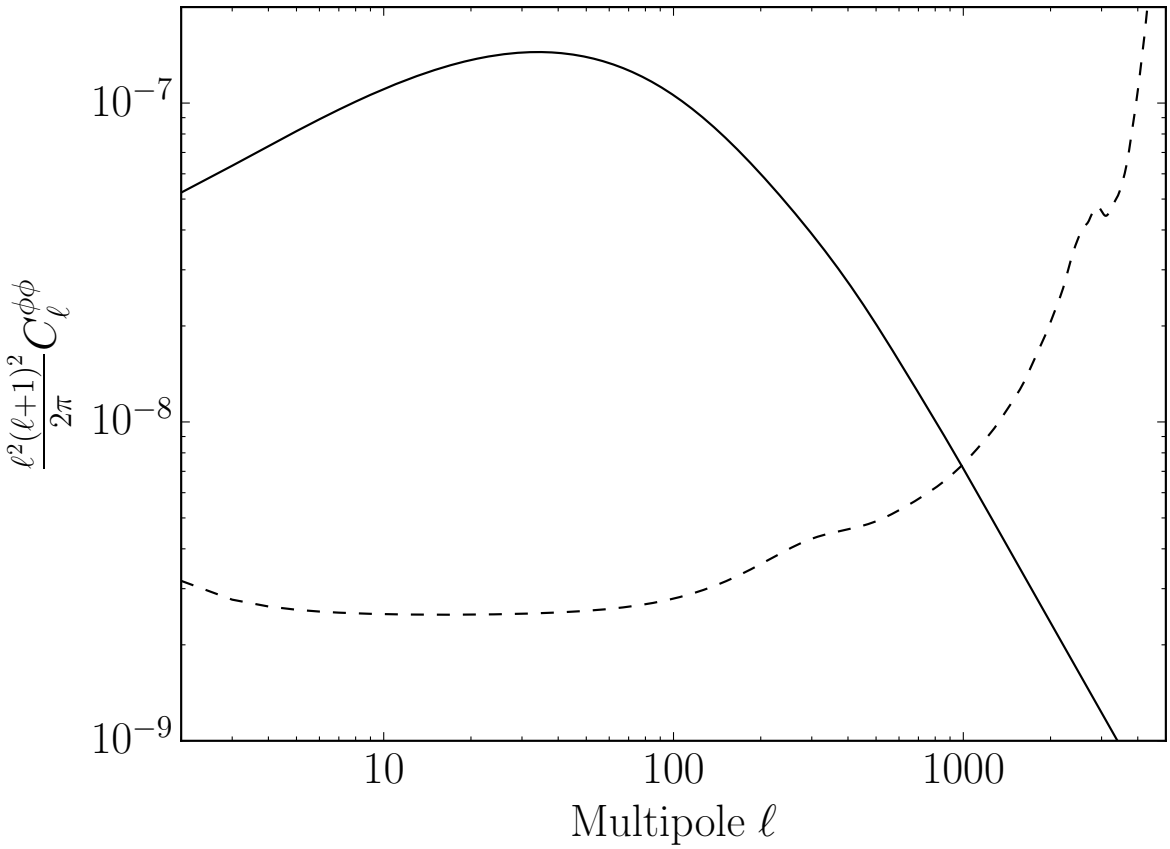

Figure 2.1: Comparison of the lensing potential power spectra $C_\ell^{\phi\phi}$ (solid) with the reconstruction noise forecast for the mock CMB-S4 experiment investigated here (dashed, see text for details). The forecast is lens sample variance limited for $\ell \lesssim 10^3$.

XY; here we use the physical intuition gained in [33] to extend the same model to include their covariance with measurements of $\phi\phi$. A similar model has recently been also used in [35, 36].

In this model the correlation matrix is split into a "Gaussian part" $\mathcal{G}$ that is diagonal in multipole space and $\mathcal{N}$ which describes non-Gaussian correlations between multipoles,

$$\mathrm{Cov}^{xy,wz}_{\ell\ell'} = \mathcal{G}^{xy,wz}_{\ell\ell'} + \mathcal{N}^{xy,wz}_{\ell\ell'}. \tag{2.2}$$

The Gaussian part is modelled after the covariance of Gaussian random fields as

$$\mathcal{G}^{xy,wz}_{\ell\ell'} = \frac{\delta_{\ell\ell'}}{2\ell+1}\left[C^{xw}_{\mathrm{exp},\ell}C^{yz}_{\mathrm{exp},\ell} + C^{xz}_{\mathrm{exp},\ell}C^{yw}_{\mathrm{exp},\ell}\right], \tag{2.3}$$

where the expectation value of the experimentally measured lensed CMB power spectra C^{xy}_{exp} includes the noise power spectrum N^{xy}_{ℓ}

$$C^{xy}_{\mathrm{exp},\ell} = C^{xy}_{\ell} + N^{xy}_{\ell}. \tag{2.4}$$

Even if we assume that the unlensed CMB fields $\tilde{X}$ and ϕ are Gaussian, the lensed CMB fields X are not. In our model, we take two non-Gaussian terms to compose the full covariance,

$$\mathcal{N}^{xy,wz}_{\ell\ell'} = \mathcal{N}^{(\phi)xy,wz}_{\ell\ell'} + \mathcal{N}^{(E)xy,wz}_{\ell\ell'}, \tag{2.5}$$

which we now describe.

Gravitational lensing induces non-Gaussian covariances between the data because all power spectra are affected by the same realization of the lensing potential; sample variance fluctuations of the lensing power produce coherent changes in all the observed power spectra. The effect accumulates over the whole multipole range of the lenses and is largest for those

C_ℓ^{XY} which are the most strongly affected by lensing. It is modeled by adding an extra term

$$\mathcal{N}_{\ell\ell'}^{(\phi)xy,wz} = \sum_L \frac{\partial C_\ell^{xy}}{\partial C_L^{\phi\phi}} \mathrm{Cov}_{LL}^{\phi\phi} \frac{\partial C_{\ell'}^{wz}}{\partial C_L^{\phi\phi}} \tag{2.6}$$

to the non-Gaussian covariance $\mathcal{N}$. The power spectra derivatives are in practice calculated using a two point central difference scheme from results obtained using CAMB[1] [37]. For the reconstructed potential we take $\mathcal{N}_{\ell\ell'}^{(\phi)\phi\phi,\phi\phi} = 0$ as the corresponding variance is part of the Gaussian term.

Sample variance of the unlensed $\tilde{E}\tilde{E}$ power spectrum and its coherent propagation into the lensed power spectra through gravitational lensing produces similar but typically weaker effects. Following [33], we include this contribution only for $\mathrm{Cov}_{\ell\ell'}^{XY,BB}$, with

$$\mathcal{N}_{\ell,\ell'}^{(E)XY,BB} = \sum_L \frac{\partial C_\ell^{XY}}{\partial C_L^{\tilde{X}\tilde{Y}}} \mathrm{Cov}_{L,L}^{\tilde{X}\tilde{Y},\tilde{E}\tilde{E}} \frac{\partial C_{\ell'}^{BB}}{\partial C_L^{\tilde{E}\tilde{E}}}. \tag{2.7}$$

Other sample covariance effects from unlensed fields on XY are negligible in comparison [33]. We also assume that the analogous terms involving the reconstruction noise, e.g. $\partial N_l^{\phi\phi}/\partial C_L^{\tilde{E}\tilde{E}}$ and other non-Gaussian reconstruction terms are negligible. This should be a good approximation in the lens sample dominated regime $\ell \lesssim 10^3$.

The covariances $\mathrm{Cov}^{XY,WZ}$ we obtain for the CMB power spectra qualitatively agree with those plotted in Fig. 1 of [33] for the same analytical model for covariances but for a slightly different cosmological model. The less well studied covariances $\mathrm{Cov}^{XY,\phi\phi}$ are shown in Figure 2.2; for illustrative purposes we plot the correlation coefficient

$$R_{\ell\ell'}^{XY,\phi\phi} = \frac{\mathrm{Cov}_{\ell\ell'}^{XY,\phi\phi}}{\sqrt{\mathrm{Cov}_{\ell\ell}^{XY,XY}\,\mathrm{Cov}_{\ell'\ell'}^{\phi\phi,\phi\phi}}}. \tag{2.8}$$

In this plot we assume experimental and reconstruction noise for our reference experiment.

1. `https://github.com/cmbant/CAMB/`

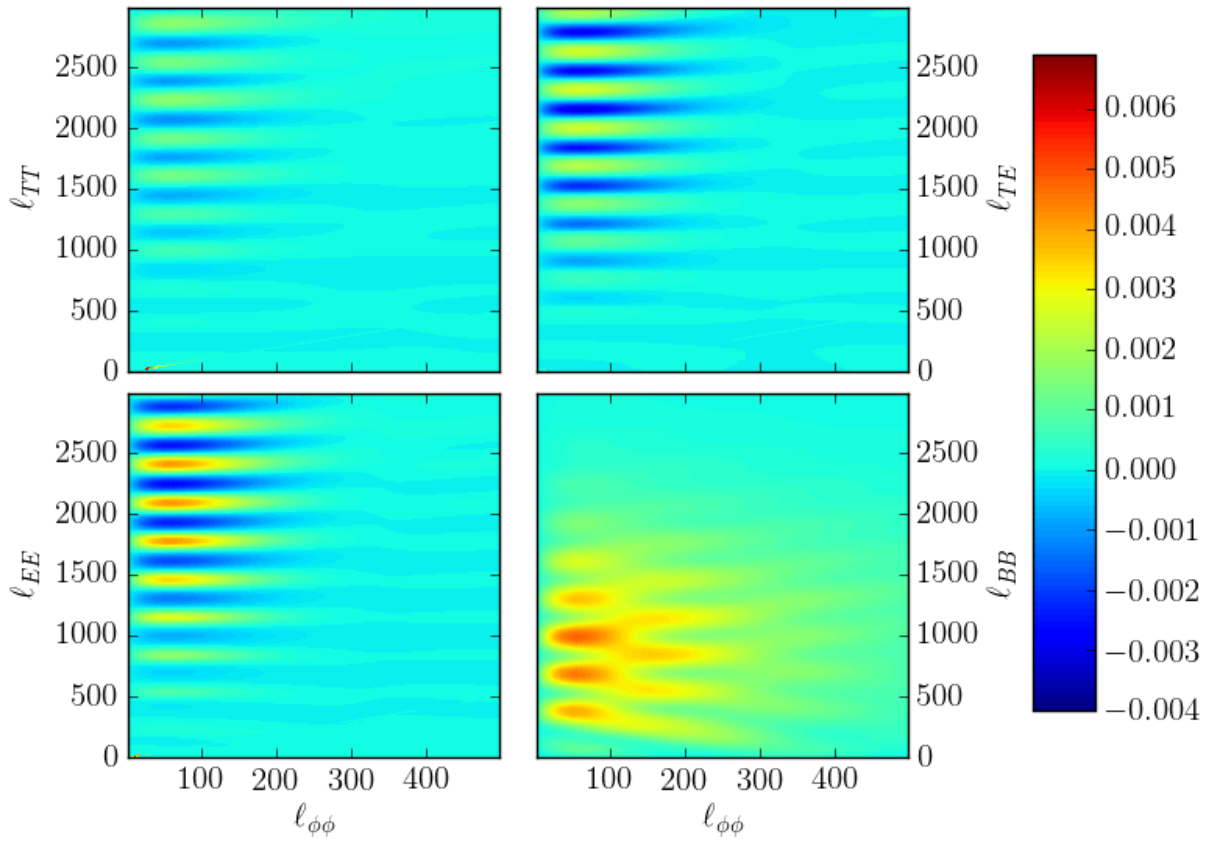

Figure 2.2: Correlation matrix $R^{XY,\phi\phi}_{\ell_{XY},\ell_{\phi\phi}}$ (2.8) between the C_ℓ^{XY} CMB power spectra and the power spectra of the reconstructed lensing potential $C_\ell^{\phi\phi}$. Barely visible features for $\ell_{XY} = \ell_{\phi\phi} \lesssim 50$ in the first three panels represent contributions from the Gaussian terms due to nonzero $C_\ell^{T\phi}, C_\ell^{E\phi}$.

We see that the covariances peak for $\ell' = \ell_{\phi\phi} \sim 100 - 200$ which reflects the fact that most of the lensing is caused by lenses at these scales. In covariances with TT, TE and EE there are alternating regions of positive and negative correlations, corresponding to smearing of the peaks and troughs; correlation with BB also shows acoustic features due to oscillations in the unlensed $C_\ell^{\tilde{E}\tilde{E}}$ on top of a positive definite contribution. The broad band BB power thus coherently covaries with the lens power [38]. These results also agree with Ref. [35, 36].

A similar analytic approach to modelling covariances was recently compared against numerical simulations [36]. That model was found to work well after realization-dependent noise subtraction. As can be seen from their Figs. 3 and 4, these subtractions affect mostly correlations with lensing power spectra above $\ell \sim 1000$ and would be hidden by reconstruction noise in our approach. They also show that the other trispectrum terms to the covariance, which we neglect, are subdominant. Potentially more troublesome is their finding that there are some differences between the analytical model and simulations, especially in $\mathrm{Cov}^{BB,\phi\phi}$ at low ℓ_{BB} which they claim appears to be statistically significant [39]. If confirmed, then our analysis implicitly assumes that such additional effects have negligible effect on our results.

2.3 Simulated data and their analysis

To test importance of the lensing-induced covariances for getting correct cosmological parameter constraints, we simulate lensed CMB skies, compute the related power spectra $\hat{C}_\ell^{XY}$ and analyze them in a Markov Chain Monte Carlo analysis using likelihoods that either include or omit the non-Gaussian covariances caused by gravitational lensing. In this section we provide details of our analysis pipeline.

2.3.1 Simulated data

To simulate lensed CMB data we use the publicly available code Lenspix[2] [40] with unlensed CMB power spectra calculated by CAMB. We modified the code to lower its memory demands and speed up the calculation, see Appendix A for details on these modifications. Once the lensed CMB maps are generated, we add normally distributed instrumental noise and calculate power spectra to form a simulated data set $\hat{C}_\ell^{XY}$.

2.3.2 Markov Chain Monte Carlo analysis

We investigate the simulated CMB power spectra using the Markov Chain Monte Carlo (MCMC) code CosmoMC[3] [41], which for a given realization of the data samples the posterior probability in the space of cosmological parameters. We assume uniform priors in the cosmological parameters and use the likelihood described below. In the MCMC runs we sample the posterior until the Gelman-Rubin statistic $R-1$ [42] drops below 0.01.

To avoid biasing results, we calculate the unlensed fiducial spectra which enter Lenspix simulations with the same precision settings which is later used in CosmoMC. We checked that increasing precision with which the lensing operation in CosmoMC is calculated (increasing `accuracy_boost` in the lensing routine) does not have any effect on the resulting parameter constraints.

2.3.3 Likelihood for $\hat{C}_\ell^{XY}$

An accurate likelihood for CMB power spectra data $\hat{C}_\ell^{XY}$ has to capture both lensing-induced covariance $\mathrm{Cov}_{\ell,\ell'}^{XY,WZ}$ and the non-normal distribution of the power spectra at low multipoles. Here we illustrate these effects with simulated data and then describe our model for the likelihood.

2. https://github.com/cmbant/lenspix

3. https://github.com/cmbant/CosmoMC

Using 2000 Lenspix simulations, it is possible to illustrate that the lensed CMB data are indeed correlated. Because this number of simulations is insufficient to show correlation of individual power spectra multipoles, we look at correlation between band powers

$$P^{XY}_{\ell_1,\ell_2} = \frac{1}{\ell_2 - \ell_1} \sum_{\ell=\ell_1}^{\ell_2} \frac{\ell(\ell+1)\Delta C^{XY}_\ell}{2\pi}, \tag{2.9}$$

where

$$\Delta C^{XY}_\ell = \hat{C}^{XY}_\ell - C^{XY}_{\mathrm{exp},\ell} \tag{2.10}$$

is the deviation of the experimentally measured power spectrum from its expectation value. As an example, in Figure 2.3 we plot the distribution of two BB band powers as determined from our simulations, together with theoretical curves showing 68% and 95% confidence intervals derived from our model for the covariance $\mathrm{Cov}^{XY,WZ}_{\ell,\ell'}$. We see that the data are indeed strongly correlated and that the model describes this correlation well.

Fortunately for the likelihood construction, non-Gaussian covariances $\mathcal{N}^{XY,WZ}_{\ell\ell'}$ of the low ℓ data are considerably smaller than the corresponding Gaussian part of the covariance. Indeed, the largest correlation coefficient

$$\mathcal{R}^{XY,WZ}_{\ell\ell'} = \frac{\mathcal{N}^{XY,WZ}_{\ell\ell'}}{\sqrt{\mathrm{Cov}^{XY,XY}_{\ell\ell}\,\mathrm{Cov}^{WZ,WZ}_{\ell'\ell'}}} \tag{2.11}$$

with $\ell < 30$ is 8×10^{-4}. We shall therefore neglect lensing-induced covariances in the likelihood for the large scale data.

As pointed out above, the low ℓ data are not normally distributed. For example, in Fig. 2.4 we plot the distribution of B-mode power spectra including noise for $\ell = 2, 30$ obtained in the same Lenspix simulations. In the same plot we show a normal distribution centered on the expected mean of the data, with standard deviation given by the Gaussian

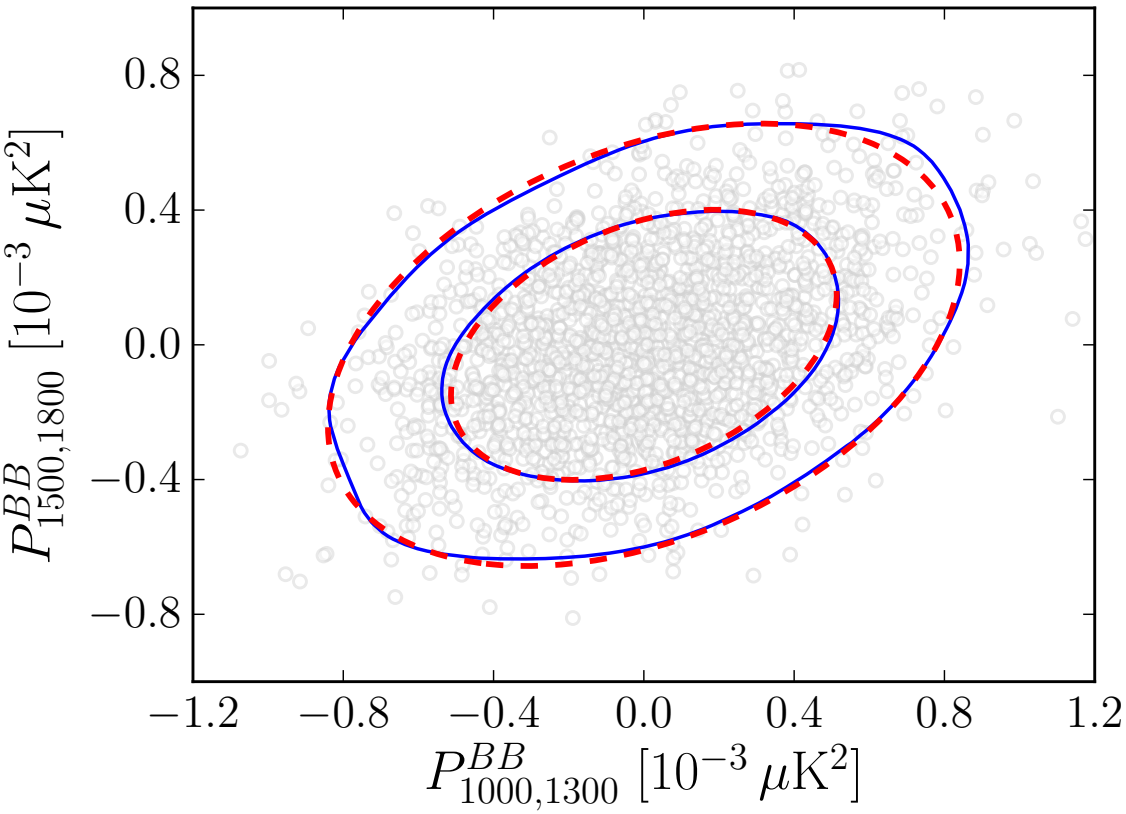

Figure 2.3: Light gray circles show the correlated values of the binned power spectra $P^{BB}_{1000,1300}$ and $P^{BB}_{1500,1800}$ as determined from 2000 Lenspix simulations. Blue lines encompass regions of 68% and 95% confidence determined from these simulations. For comparison, dashed red lines show the same confidence intervals based on our theoretical model for covariance.

expectation (2.3)

$$\sigma_\ell^{BB} = \sqrt{\frac{2}{2\ell+1}} C_{\mathrm{exp},\ell}^{BB}. \tag{2.12}$$

It is clear that for $\ell = 2$ the normal distribution is a poor description of the data. Instead, as expected, $\chi^2_{2\ell+1}$ distribution scaled by σ_ℓ^{BB} fits the data well. In the case of large scale B-modes this reflects the fact that they get most of their power from $\tilde{E}, \phi$ modes at ℓ of several hundred. Each coefficient in the spherical harmonic expansion of the B map is then a combination of many random fields and thus approximately normally distributed, which leads to a χ^2 distributed power spectra. For low ℓ TT, TE and EE, the distributions just mirror the unlensed CMB fields, due to negligible effects of lensing on these fields. Above $\ell \sim 30$ the normal distribution becomes a good description for both the χ^2 distribution and the data.

Based on these considerations, our model for the likelihood treats $\hat{C}_\ell^{XY}$ from the largest scales ($\ell < \ell_{\mathrm{break}}$) and from smaller scales separately and independently. The choice of the division point is somewhat arbitrary; in this work we use $\ell_{\mathrm{break}} = 30$.

Below ℓ_{break} we neglect lensing-induced covariance $\mathcal{N}_{\ell,\ell'}^{XY,WZ}$ and assume there is no correlation between B modes and T, E modes. Data with different multipoles ℓ, ℓ' then decouple. The likelihood of measuring the data vector $\hat{C}_\ell^{XY}$ (including instrumental noise) when the expected power spectra are $C_{\mathrm{exp},\ell}^{XY}$ is then a product of inverse Wishart distributions,

$$\begin{aligned} \mathcal{L}_{\ell<\ell_{\mathrm{break}}} \quad \propto \quad & \prod_{\ell=2}^{\ell_{\mathrm{break}}-1} \left| C_{\mathrm{exp},\ell}^{XY} \right|^{-(2\ell+1)/2} \\ & \times \exp\left(-\frac{2\ell+1}{2} \sum_{X,Y} \left(C_{\mathrm{exp},\ell}^{XY} \right)^{-1} \hat{C}_\ell^{XY} \right). \end{aligned} \tag{2.13}$$

Here $|\cdot|$ is a determinant of $\cdot$ viewed as a matrix, here in the X, Y space.

For $\ell \geq \ell_{\mathrm{break}}$ we neglect the non-normality of the distribution of each multipole and

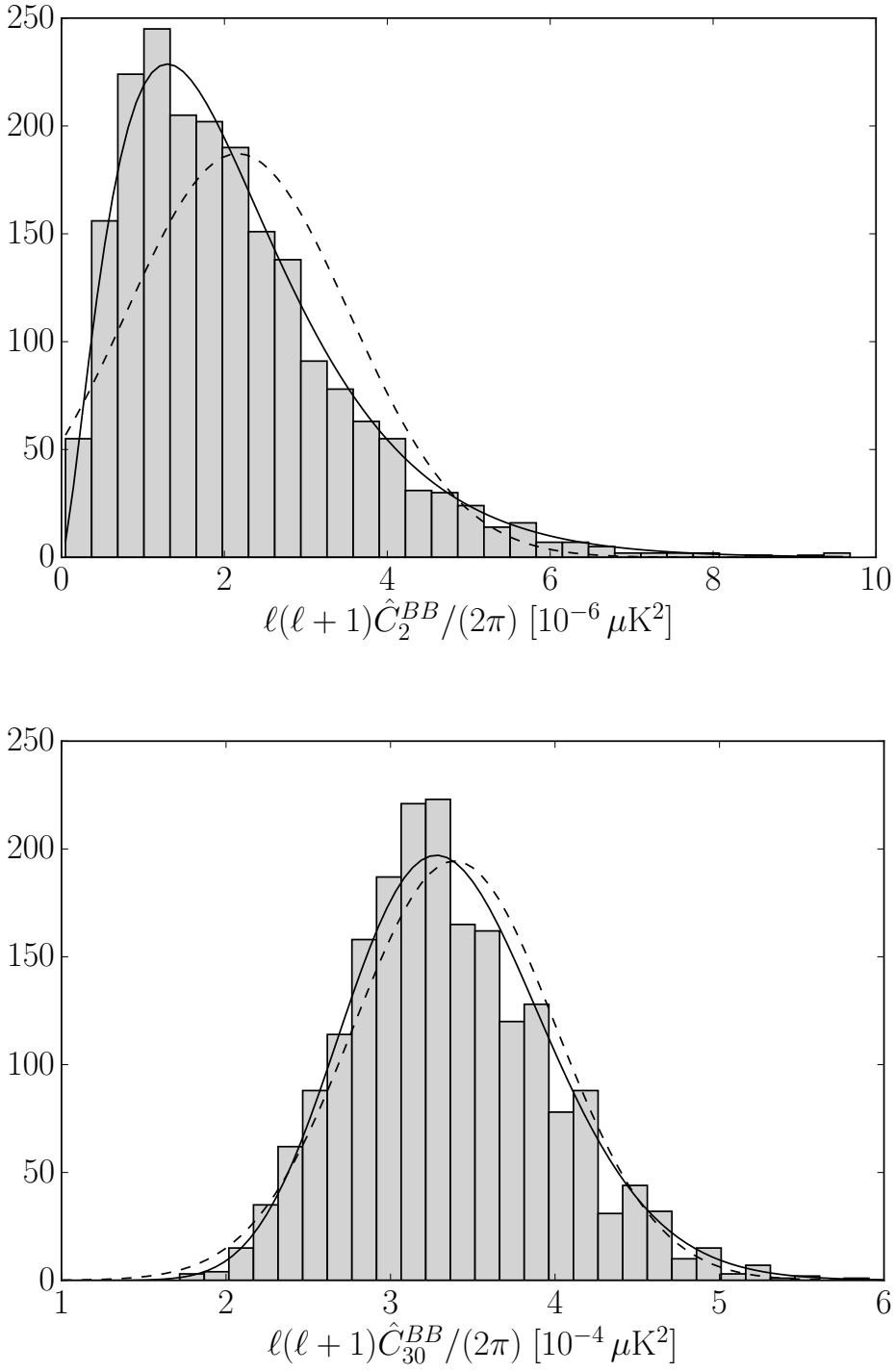

Figure 2.4: Distribution of $\hat{C}_2^{BB}, \hat{C}_{30}^{BB}$ obtained from 2000 Lenspix simulations compared against a χ^2 distribution with the Gaussian variance $(\sigma_\ell^{BB})^2$ (solid) and a normal distribution with the same variance centered on the expected mean of the data (dashed). The normal distribution becomes a good approximation for $\ell \gtrsim 30$.

instead model the lensing-induced covariance between multipoles:

$$\mathcal{L}_{\ell\geq\ell_{\rm break}} \propto |{\rm Cov}|^{-1/2} \exp\left[-\frac{1}{2}\sum_{\substack{\ell,\,\ell'\geq\ell_{\rm break}\\ XY,\,WZ}} \Delta C_\ell^{XY}\left({\rm Cov}_{\ell,\ell'}^{XY,WZ}\right)^{-1}\Delta C_{\ell'}^{WZ}\right]. \tag{2.14}$$

In all analyses of simulated data we neglect the dependence of the covariance matrix on the cosmological parameters; we evaluate it at the fixed fiducial model of Tab. 2.1.

To assess the impact of non-Gaussian covariance, we also investigate the likelihood $\mathcal{L}_{{\rm g},\ell\geq\ell_{\rm break}}$ in which the non-Gaussian covariance ${\rm Cov}_{\ell,\ell'}$ is replaced by the Gaussian covariance $\mathcal{G}_{\ell,\ell'}$.

By joining the large and small scale portions independently, we then form the total likelihood for the data

$$\ln\mathcal{L} = \ln\mathcal{L}_{\ell<\ell_{\rm break}} + \ln\mathcal{L}_{\ell\geq\ell_{\rm break}} \tag{2.15}$$

and

$$\ln\mathcal{L}_{\rm g} = \ln\mathcal{L}_{\ell<\ell_{\rm break}} + \ln\mathcal{L}_{{\rm g},\ell\geq\ell_{\rm break}}, \tag{2.16}$$

up to irrelevant additive constants.

2.4 Parameter constraints from temperature and polarization power spectra

In this section we investigate how neglecting lensing-induced covariance affects constraints on cosmological parameters when considering only the CMB temperature and polarization power spectra.

The lensing-induced covariance is an additional source of correlated noise so constraints based on the likelihood with the Gaussian covariance are typically too optimistic. Similar studies on the impact of non-Gaussian covariances have been previously performed mainly

using the Fisher approximation [33, 36, 43]. We focus here on the six parameter flat ΛCDM cosmological model and its two extensions where either the sum of the masses of neutrinos $\sum m_\nu$ (ΛCDM+$\sum m_\nu$) or the dark energy equation of state parameter w (ΛCDM+w) is allowed to vary. We find that in at least one case (ΛCDM+w) the Fisher approximation significantly underestimates the impact of the lensing-induced covariance.

For ΛCDM we on simulations also explicitly illustrate how neglecting lensing-induced covariance leads to a significant increase in the fraction of realizations in which the parameters of the underlying cosmological model are excluded at 95% confidence, which is potentially important for concordance studies.

2.4.1 ΛCDM

Neglecting lensing-induced covariances for a typical simulated CMB dataset affects constraints on ΛCDM parameters as shown in Fig. 2.5. Shifts in the best fit parameter values are typically not very significant; the major effect of including lensing covariances is a weakening of the best constrained directions between degenerate parameters, most notably that between $\Omega_c h^2$ and A_s. We comment on the origin of this effect in Section 3.3.

Because of marginalization of other parameters, the two-parameter posteriors in Fig. 2.5 hide some of the effects of the non-Gaussian covariance. To uncover the maximal possible effect on a single quantity, we construct the linear combination of the cosmological parameters

$$M = \sum_A \mathcal{K}_A \left(\theta_A - \theta_A^{\rm fid}\right) \tag{2.17}$$

that maximizes the ratio of Gaussian to non-Gaussian errors. Here $\mathcal{K}_A = \{5.8, -13.4, 18.4, -1.1, -2.6, 3.1\}$ for the parameter ordering $\{100\theta_*, \Omega_c h^2, \Omega_b h^2, n_s, \ln A_s, \tau\}$. As we discuss in greater detail in Section 3.3, M can be interpreted as a combination of cosmological parameters which mainly changes the lensing potential, especially at low ℓ.

Dashed red lines in Fig. 2.6 show posterior probabilities for M, as determined from a

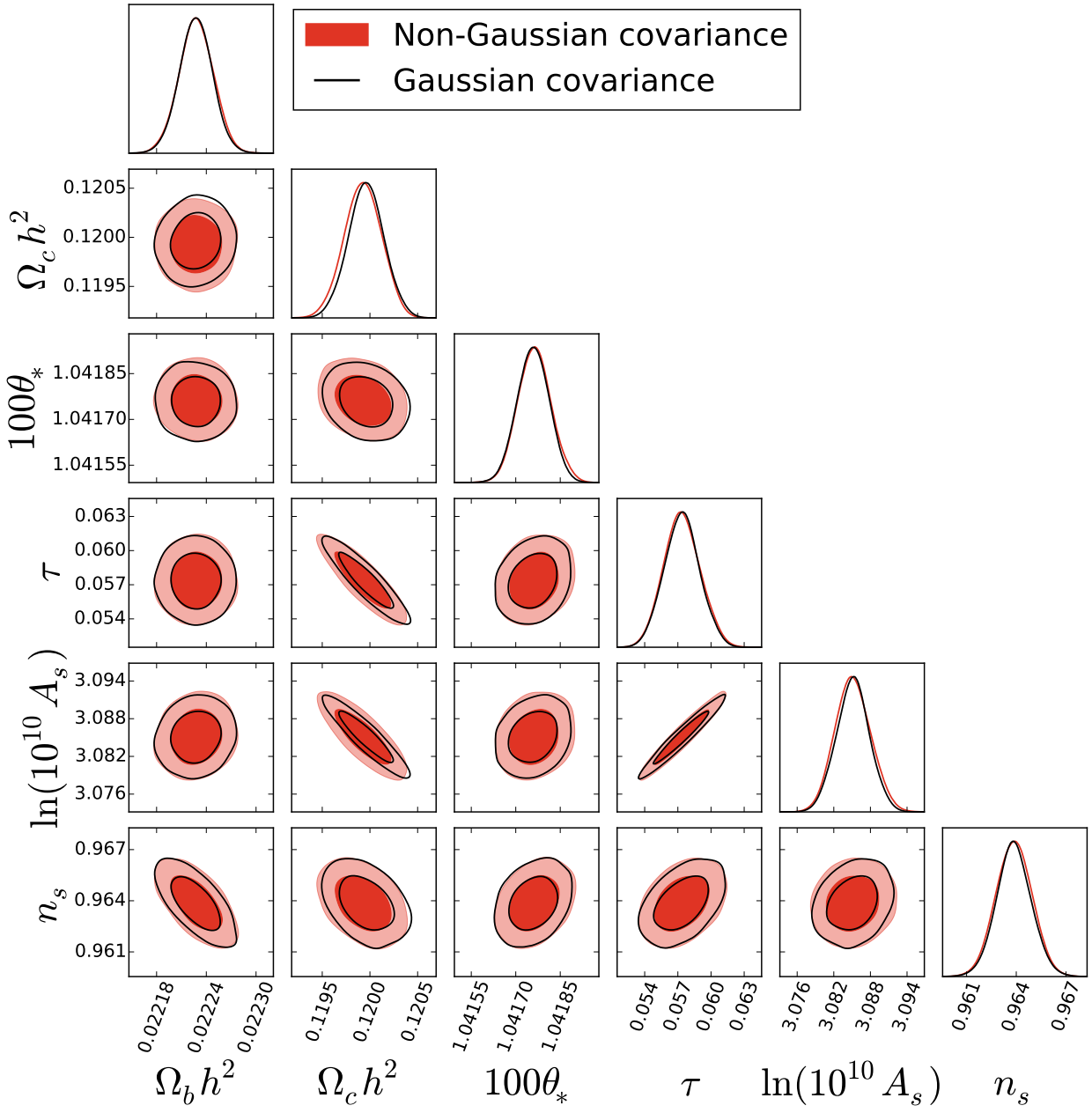

Figure 2.5: Comparison of MCMC constraints on ΛCDM parameters with analysis based on Gaussian (black curves) and non-Gaussian covariance (red shaded). Here and throughout contours enclose regions of 68% and 95% confidence intervals unless otherwise specified.

single MCMC run based on $\mathcal{L}$ (top) and $\mathcal{L}_{\rm g}$ (bottom). The same simulated CMB sky as in Fig. 2.5 is used, the maximum has been shifted to zero for future convenience, and the y-axis units are arbitrary. The standard deviations of these two posteriors are $\sigma_M^{\rm ng} = 2.1 \times 10^{-3}$ and $\sigma_M^{\rm g} = 1.0 \times 10^{-3}$, both within 3% of the Fisher forecast prediction displayed in Fig. 2.6 by a solid blue line. The analysis based on a Gaussian likelihood $\mathcal{L}_{\rm g}$ therefore underestimates the errors of M by over a factor of 2.

While the impact of this direction is hidden in the marginalized errors of the base ΛCDM parameters, it reveals itself in an increased frequency of Type 1 errors: falsely rejecting the true model. This effect would be particularly problematic for concordance studies searching for tensions between various cosmological datasets.

Since a full study of Type 1 errors in thousands of data realizations is computationally expensive, we illustrate this problem by analytically approximating the best fit values of the parameters, including M, for each realization. We assume the data are sufficiently close to the fiducial model that it is possible to approximate the C_ℓ^{XY} as linear in the parameter deviations $\theta_A - \theta_A^{\rm fid}$. Neglecting for the moment complications arising from presence of the low ℓ data by assuming all the data are distributed according to a multivariate normal distribution with covariance (2.2), we obtain the maximum likelihood or best fit estimate for a cosmological parameter $\theta_A^{\rm bf}$ as[4]

$$\begin{aligned} \Delta\theta_A &\equiv \theta_A^{\rm bf} - \theta_A^{\rm fid} \\ &= \sum_{B,i,j} F_{AB}^{-1} \frac{\partial D_i}{\partial \theta_B} \left({\rm Cov}^{-1}\right)_{ij} \left(\hat{D}_j - D_j^{\rm fid}\right). \end{aligned} \tag{2.18}$$

Here the power spectrum data are indexed as $D_i = C_\ell^{XY}$ with i running over all XY, ℓ

4. Numerical maximization of the likelihood in ten simulations provides an average shift in M below $0.08\,\sigma_{M,{\rm bf}}$ with respect to the analytic formula (2.18) for either covariance. The analytic treatment is thus sufficiently accurate for our purposes.

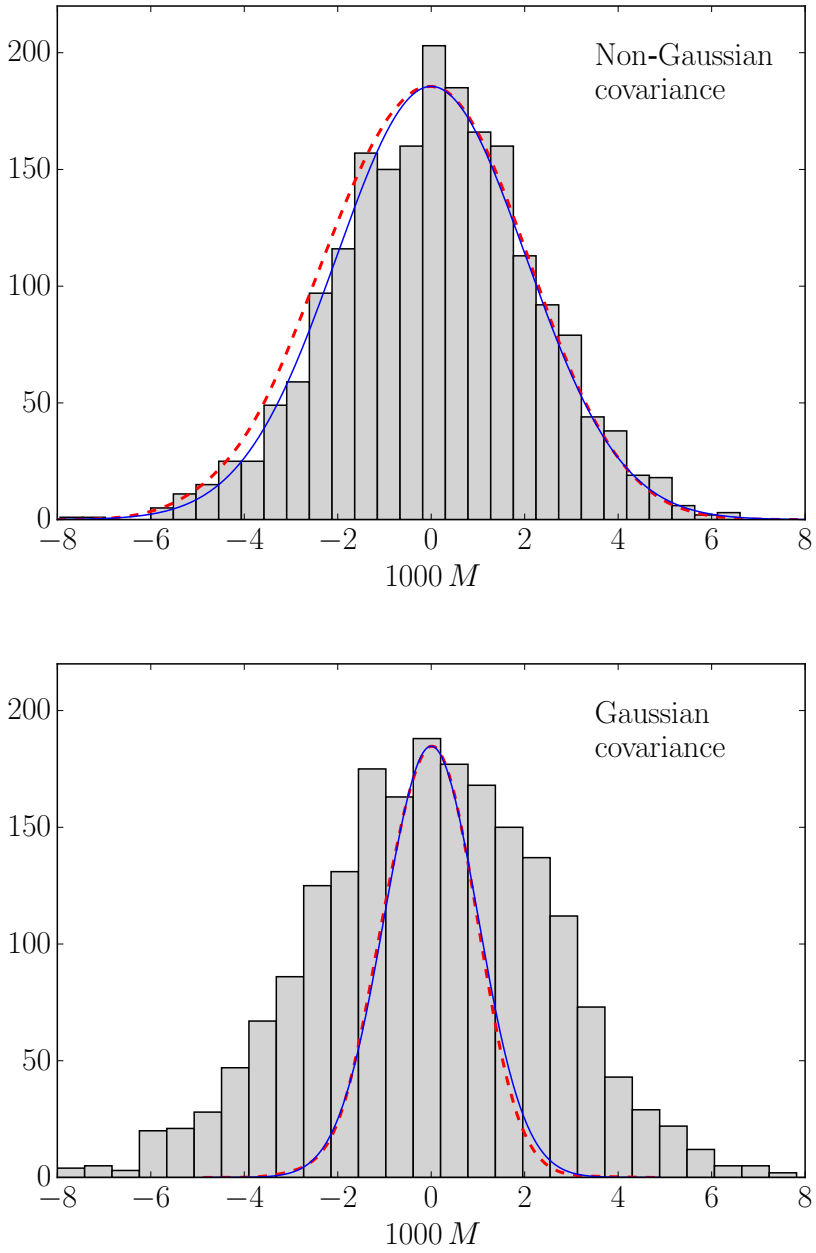

Figure 2.6: Histograms showing best fit values of M determined from 2000 lensed CMB skies using an analytic approach (see text) for analysis based on non-Gaussian (top) and Gaussian covariance (bottom). The dashed red curves show the 1D posterior probability for M, as determined from a single CMB realization, shifted to zero for better comparison. Despite the Fisher forecast (solid blue curves) agreeing in both cases, the posterior probability does not reflect the much wider best-fit distribution in the Gaussian case.

elements and B runs over ΛCDM parameters. The Fisher information matrix,

$$F_{AB} = \sum_{ij} \frac{\partial D_i}{\partial \theta_A} \left(\mathrm{Cov}\right)^{-1}_{ij} \frac{\partial D_j}{\partial \theta_B}, \tag{2.19}$$

and parameter derivatives are evaluated around the fiducial model.

With the best fit values of cosmological parameters we can directly calculate the best fit values of M for both the non-Gaussian and Gaussian analysis. The two differ only in the choice of covariance matrix in Eqs. (2.18) and (2.19).

Best fit values of M determined from 2000 simulated CMB skies are shown in histograms in Fig. 2.6 for the non-Gaussian (top) and Gaussian (bottom) covariance analyses. In the non-Gaussian case, this distribution has a standard deviation $\sigma^{\rm ng}_{M,\rm bf} = 2.1 \times 10^{-3}$ which is in excellent agreement with the prediction from the posterior $\sigma^{\rm ng}_M$ determined from the MCMC analysis of single realization as well as the Fisher approximation. On the other hand, in the Gaussian analysis the best fit values of M scatter with standard deviation $\sigma^{\rm g}_{M,\rm bf} = 2.5 \times 10^{-3}$, which is 2.5 times the width of $\sigma^{\rm g}_M$ despite the latter agreeing with its Fisher approximation. This mismatch can lead to Type 1 errors in cases where the best fit M fluctuates away from the fiducial value zero.

Notice that the best fit distribution is wider in the Gaussian than non-Gaussian case by a factor of ~ 1.2 which further exacerbates the probability of Type 1 errors. This is not surprising, Eq. (2.18) is a minimum variance estimator only if the assumed model of the covariances is correct which it is not in the Gaussian case.

To quantify the probability of Type 1 errors considering all parameters that specify the ΛCDM model, we can also compute χ^2 between the best fit and the true fiducial model assuming the errors from the posterior

$$\chi^2(\Delta\theta_A) = \sum_{AB} \Delta\theta_A \mathrm{Cov}^{-1}_{AB} \Delta\theta_B \approx \sum_{AB} \Delta\theta_A F_{AB} \Delta\theta_B. \tag{2.20}$$

In order to estimate χ^2 for each of the 2000 lensed CMB simulations, we again use the Fisher matrix as an approximation to the inverse covariance.[5] The variable $\chi^2(\Delta\theta_A)$ should be χ^2_6 distributed, where 6 is the number of cosmological parameters in ΛCDM.

Histograms of $\chi^2(\Delta\theta_A)$ for the Gaussian and non-Gaussian analysis are compared in Fig. 2.7 to the theoretical expectation. It is clear that in the Gaussian analysis, the mises-timate of the parameter covariance as well as the suboptimal estimate of the best fit causes a strong disagreement with the expected χ^2_6 distribution.

For example, when the analysis is based on the Gaussian covariance, more than 30% of the simulations show $\chi^2(\Delta\theta_A) > 12.59$; for χ^2_6 this value is exceeded only in 5% of the cases. As pointed out above, this can be potentially dangerous for concordance studies. The non-Gaussian covariance leads to much better agreement ($\sim 6.9\%$ of simulations have $\chi^2(\Delta\theta_A) > 12.59$) and moreover there is no long tail to very high $\chi^2(\theta_A)$.

In the Appendix B we comment on small changes to some of the conclusions of this section for an experimental configuration which observes only part of the sky and does not measure data at multipoles $\ell < 30$.

2.4.2 $\Lambda CDM + \sum m_\nu$

In this section we release the neutrino mass from its fiducial value and investigate a seven-parameter extension of ΛCDM. In this case, the two parameter contour plots, shown in Fig. 2.8, show much smaller effects of non-Gaussian covariance than in ΛCDM, though the impact is visible in the lower limit for $\sum m_\nu$. Ref. [36] also found only small effects for this case.

However, this does not mean non-Gaussian covariance can be neglected in this case, only that its effects are hidden by marginalizations. As for ΛCDM, we can form a combination

5. Using the ten simulations in which we find actual best fit ΛCDM parameters and use actual posterior covariance for the parameters, we can estimate what is the error from using in (2.20) the analytic estimator for $\Delta\theta_A$ and Fisher matrix. The average change in $\chi^2(\theta_A)$ we observe is 0.7, sufficiently smaller than the width of the final distributions. Most of this difference comes from the analytic estimator (2.18).

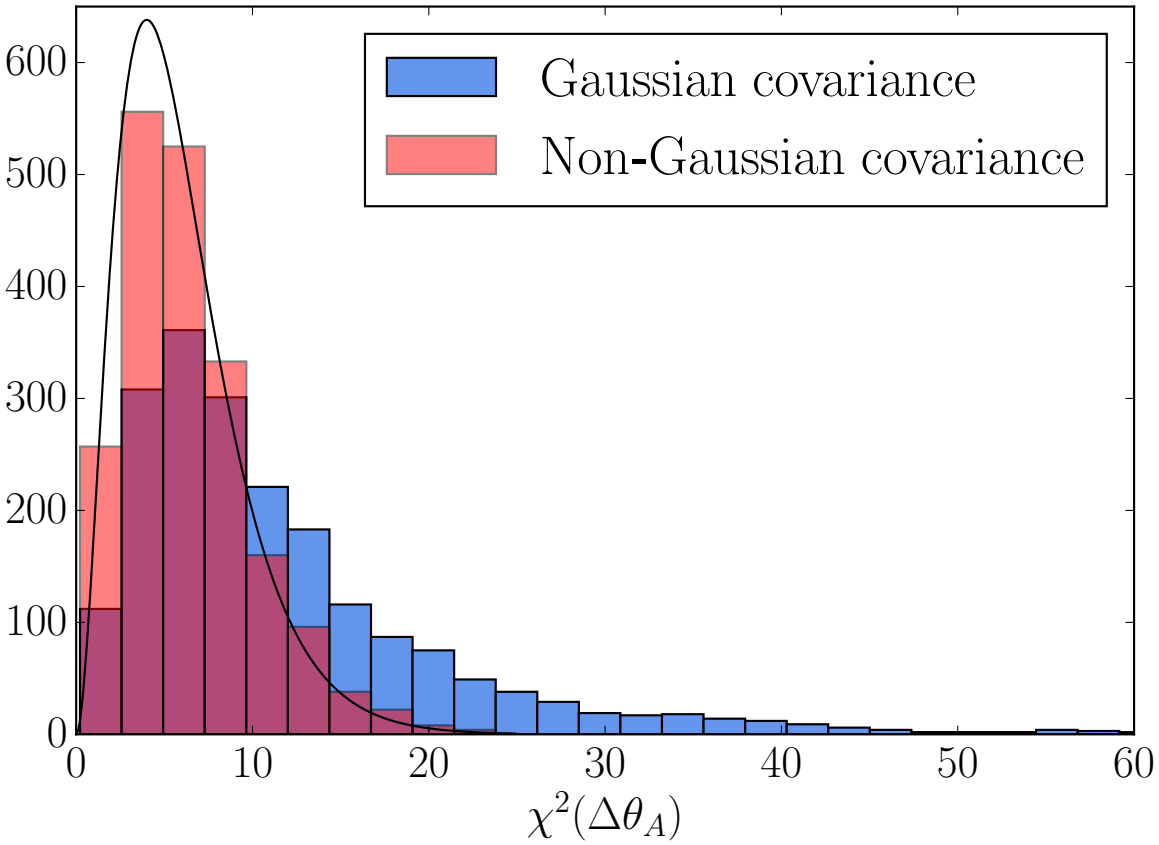

Figure 2.7: Histogram of $\chi^2(\Delta\theta_A)$ for the parameter deviations of the best fit from the true model (2.20), as determined from our simulations with Gaussian (blue) and non-Gaussian (red) covariance. For comparison, the solid line is proportional to probability density function of χ^2_6. The long tail in the Gaussian case leads to anomalously frequent Type 1 errors where the true model is rejected at high confidence (see text).

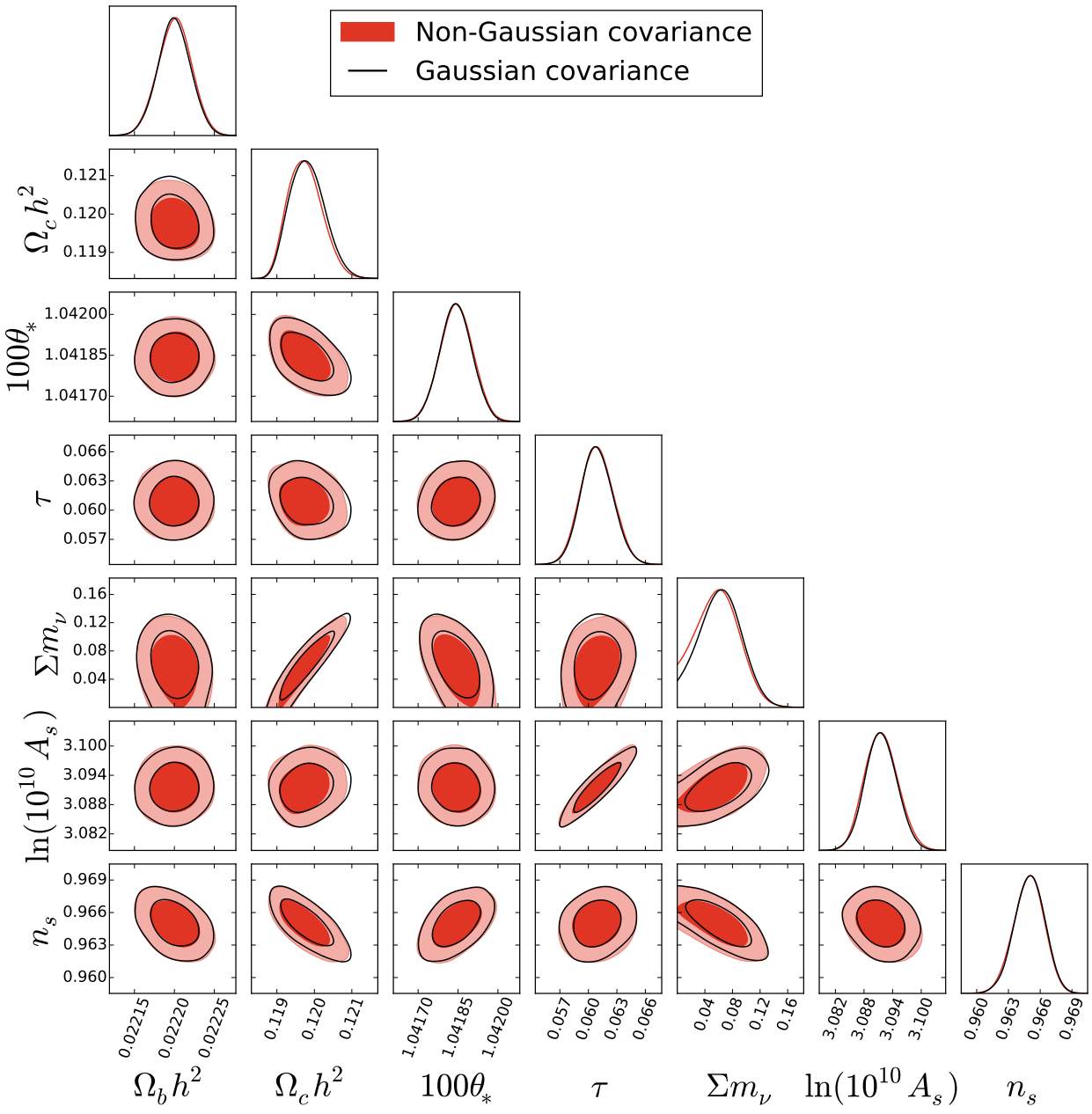

Figure 2.8: Comparison of MCMC constraints on ΛCDM+$\sum m_\nu$ parameters with analysis based on Gaussian (black curves) and non-Gaussian covariance (red shaded).

of the cosmological parameters which is predicted by the Fisher forecast to show the largest effect of non-Gaussian covariance,

$$M^\nu = \sum_A \mathcal{K}_A^\nu \left(\theta_A - \theta_A^{\rm fid}\right) \tag{2.21}$$

with $\mathcal{K}_A^\nu = \{5.7, -13.3, 18.4, -1.1, -2.6, 3.1, 0.29\,\mathrm{eV}^{-1}\}$, for the ordering $\{100\theta_*, \Omega_c h^2, \Omega_b h^2, n_s, \ln A_s, \tau, \sum m_\nu\}$. In Fig. 2.9 we can see 1D posterior probabilities for M^ν from MCMC analyses based on Gaussian and non-Gaussian covariance. It is clear M^ν constraints are nearly as strongly affected by the lensing-induced covariance as M for ΛCDM, with standard deviation degrading from 1.1×10^{-3} to 2.2×10^{-3}, even though this effect does not show up in any pair of base parameters. Likewise, the Gaussian analysis is prone to Type 1 errors as in the ΛCDM case.

The standard deviations of M^ν quoted in the previous paragraph differ somewhat from their Fisher forecasts: 1.0×10^{-3} and 2.1×10^{-3} for the Gaussian and non-Gaussian cases respectively. This occurs in part because the posterior is non-normal due to the presence of the physicality prior $\sum m_\nu > 0$ which hides some of the non-Gaussian covariance effects (cf. Fig. 2.8). In CMB realizations where neutrino mass is detected with high significance and the effect of the prior boundary is smaller, M^ν constraints are in good agreement with the Fisher prediction.

2.4.3 ΛCDM + w

In the model where we allow the dark energy parameter of state to vary, the effect of non-Gaussian covariance is more pronounced and clearly visible already on posterior probability distribution for w, see Fig. 2.10. The two analyses, based on $\mathcal{L}$ and $\mathcal{L}_{\rm g}$, strongly disagree in the low w tail; by neglecting the covariance induced by the gravitational lensing one would wrongly rule out low values of w. For example, for this particular realization lower 95% confidence limits (two sided) for the non-Gaussian and Gaussian likelihoods are -1.55 and

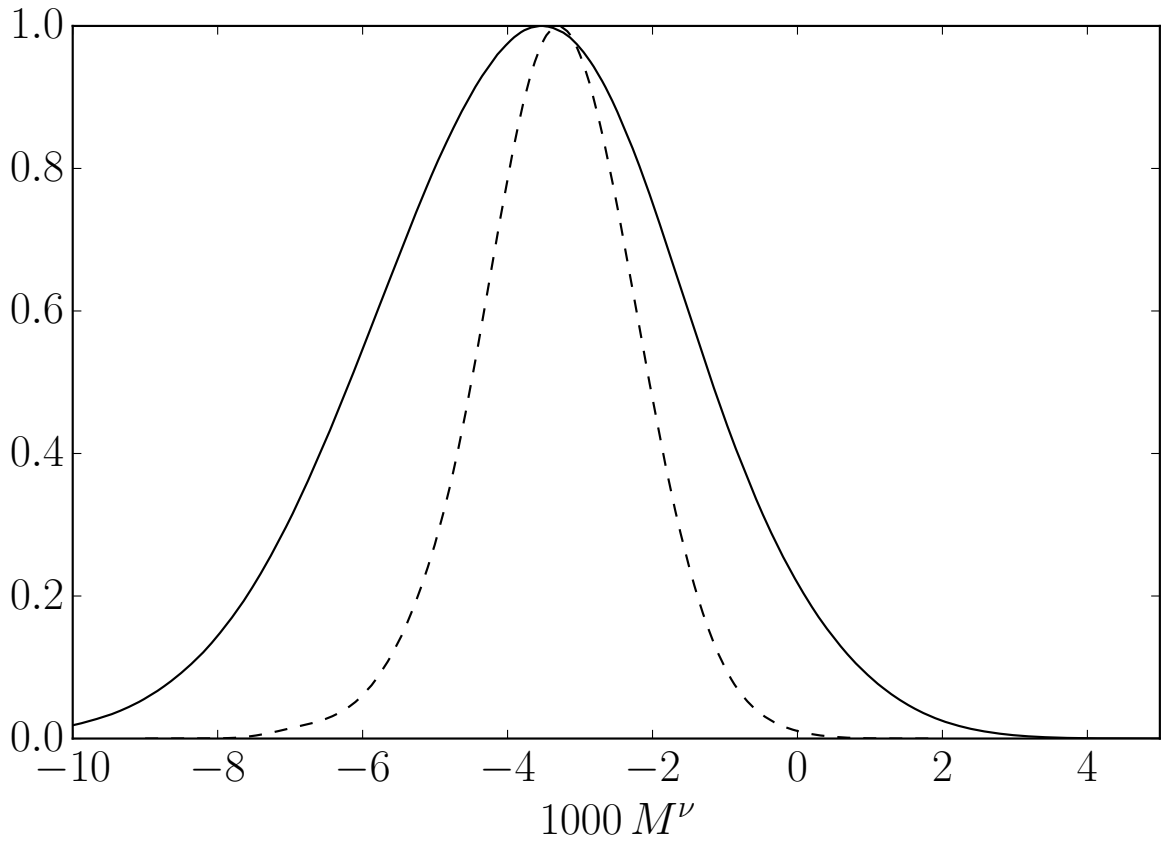

Figure 2.9: Effect of the non-Gaussian covariance on constraints on a parameter combination M^ν (2.21) within ΛCDM+$\sum m_\nu$; the combination was chosen to maximize this effect. Solid line shows MCMC constraints with non-Gaussian covariance, dashed line with the Gaussian covariance.

-1.37 respectively. In Section 3.3 we look deeper into this behavior.

The impact of the non-Gaussian covariance depends to some extent on the best fit value of w; simulations with lower best fit values of w typically show larger effects of non-Gaussian covariance. To illustrate this, in Fig. 2.11 we show marginalized constraints on w for six different simulations, both with Gaussian and non-Gaussian likelihood.

In the Fisher approximation, ΛCDM+w was investigated for essentially the same experimental configuration in [43]. It was found that non-Gaussian covariances should increase errors on w by only about 24%, which is considerably less than what we uncovered in the full MCMC analysis. In this case, the local approximation thus gives misleading results, due to the non-normal posterior which the Fisher approximation can not faithfully capture. The origin of this behavior can be traced back to how dark energy affects lensing. As w decreases, its effect on the lensing potential quickly diminishes, as dark energy ceases to be important at redshifts where the lensing kernel peaks. Because in this case the parameter combination constrained by lensing is significantly changing throughout the allowed parameter posterior, the Fisher analysis fails to capture the full significance of the non-Gaussian covariance.

The maximally impacted linear combination of base parameters also shows an enhanced non-Gaussian effect compared with ΛCDM and ΛCDM+$\sum m_\nu$. It reads

$$M^w = \sum_A \mathcal{K}^w_A \left(\theta_A - \theta^{\rm fid}_A\right), \tag{2.22}$$

where $\mathcal{K}^w_A = \{5.7, -12.8, 18.0, -1.0, -2.5, 2.9, 0.087\}$ for the ordering $\{100\theta_*, \Omega_c h^2, \Omega_b h^2, n_s, \ln A_s, \tau, w\}$. Posterior probabilities for M^w from MCMC analyses based on Gaussian and non-Gaussian covariance are shown in Fig. 2.12. In this case, the standard deviations $\sigma^{\rm ng}_{M^w,{\rm Fish}} = 2.3 \times 10^{-3}$ and $\sigma^{\rm g}_{M^w,{\rm Fish}} = 1.0 \times 10^{-3}$ derived using a Fisher approximation show that the relative impact of non-Gaussian covariance is in reasonable agreement with the MCMC results $\sigma^{\rm ng}_{M^w} = 7.6\times10^{-3}$ and $\sigma^{\rm g}_{M^w} = 3.4\times10^{-3}$, but the overall scale is still strongly underestimated by the Fisher analysis as is the extent of the lower tail. These mismatches

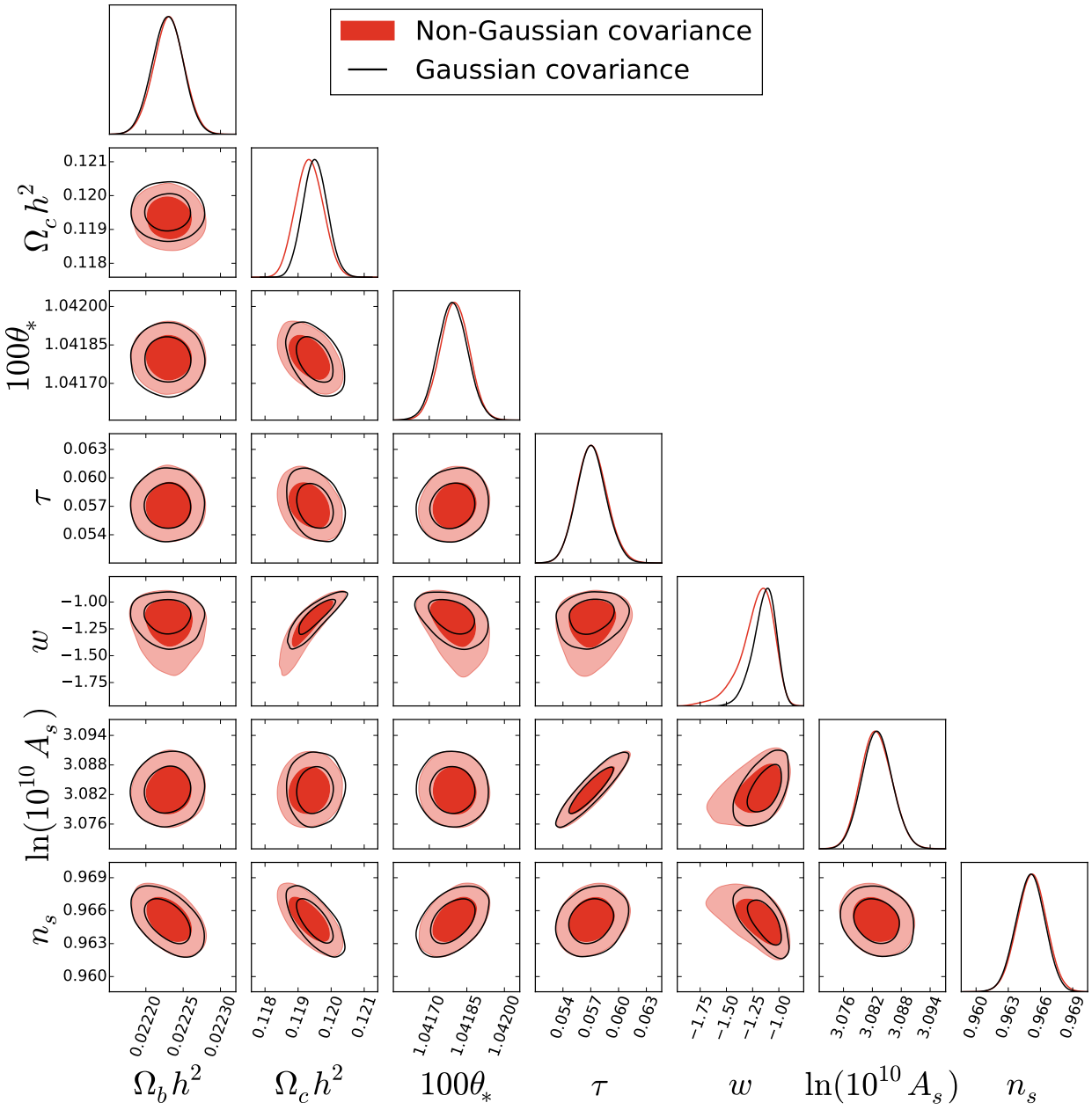

Figure 2.10: Comparison of MCMC constraints on ΛCDM+w parameters with analysis based on Gaussian (black curves) and non-Gaussian covariance (red shaded). The impact of non-Gaussian covariance is clearly apparent in constraints involving w.

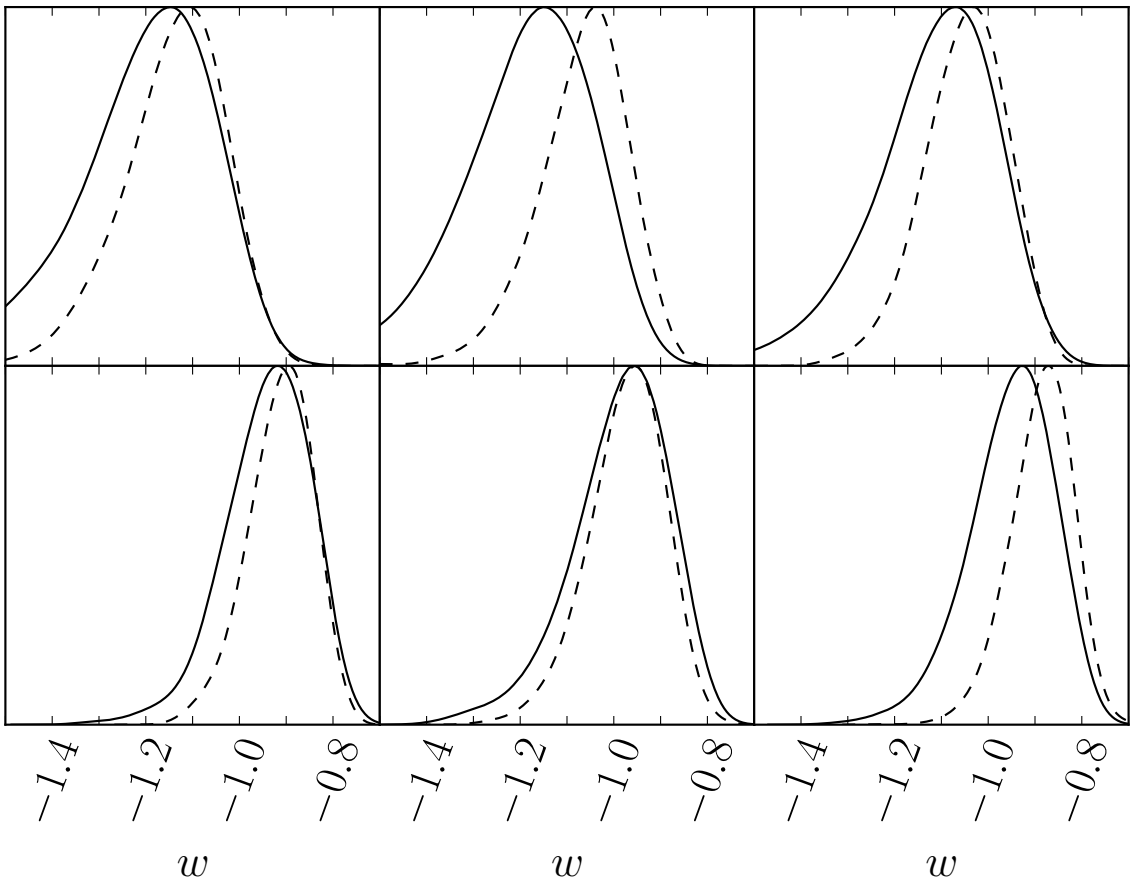

Figure 2.11: MCMC constraints on w for our experimental setup; each panel represents a different ΛCDM simulation of the CMB sky with that of Fig. 2.10 in the top left corner. The Gaussian analysis (dashed) increasingly deviates from the non-Gaussian analysis (solid) as the maximum likelihood value of w decreases.

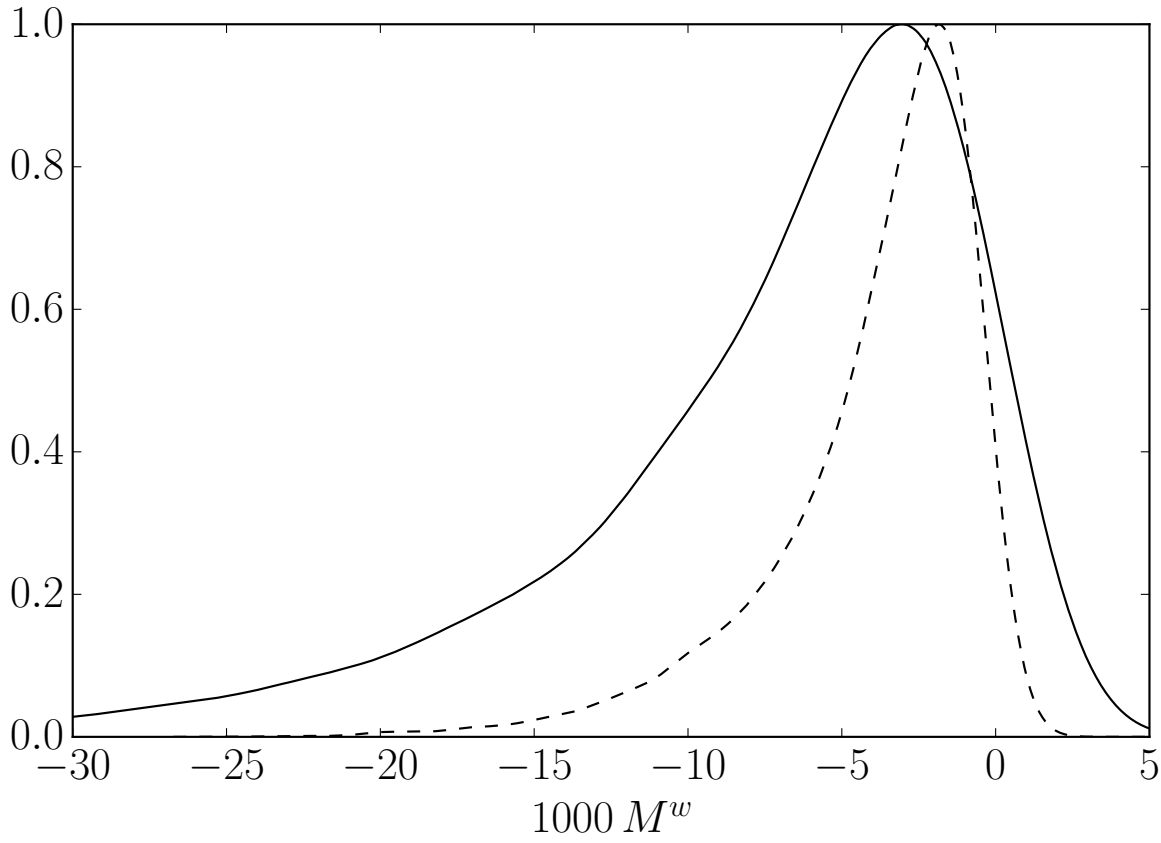

Figure 2.12: Effect of the non-Gaussian covariance on constraints on a parameter combination M^w (2.22) within ΛCDM+w; the combination was chosen to maximize this effect locally around the fiducial model. Solid line shows MCMC constraints with non-Gaussian covariance, dashed line with the Gaussian covariance.

are expected for the same reason that they appear in w alone, namely due to parameter nonlinearity within the allowed region. Likewise, M^w defined by (2.22) only captures the parameter combination which is the most affected by the lensing-induced covariance locally at the fiducial model parameters, not necessarily globally (see Section 3.3).

2.5 Adding lensing reconstruction

As pointed out in Section 2.2, lensing also correlates the XY power spectra with the power spectra of the reconstructed lensing potential. In this section we use the Fisher forecast tech-

nique to probe effects of these covariance terms $\mathrm{Cov}^{XY,\phi\phi}$ on the constraints of cosmological parameters; full analysis using lensing reconstruction from simulated CMB data is beyond the scope of this work. Although the $T\phi$ and $E\phi$ spectra are also observable we omit them as a source of information due to their small constraining power.

In Figure 2.13 we compare how the Fisher forecasts on two eight-parameter extensions of ΛCDM change when we neglect the effect of $\mathrm{Cov}^{XY,\phi\phi}$. In these plots, ΛCDM parameters are marginalized over. While for the extension with w and $\sum m_\nu$ the effect is sizable and amounts to $\sim 20\%$, for model with both spatial curvature Ω_K and $\sum m_\nu$ the effect is much smaller. These differences reflect parameter degeneracies in the lensing observables, as will be explained in the next chapter.

We also show in Figure 2.13 the same constraints with the 6 ΛCDM parameters fixed. It is clear that the best constrained direction is limited by degeneracies with ΛCDM parameters, especially with $\Omega_c h^2$ [43]. The worst constrained direction is limited instead by the ability of lensing or other constraints to separate the two additional parameters.

Conversely, in the ΛCDM model with only the 6 standard parameters varied, parameter errors change by less that 4% when neglecting $\mathrm{Cov}^{XY,\phi\phi}$. This reflects the fact that these parameters are well-constrained even in the absence of lensing.

Note also that constraints on cosmological parameters depend strongly on how well τ is constrained whereas those on the lensing power spectrum $C_L^{\phi\phi}$ itself do not [43]. For the measurements to cleanly separate $C_L^{\phi\phi}$ information, we primarily need the unlensed CMB in the acoustic regime $C_\ell^{\tilde{X}\tilde{Y}}$ to be well-characterized. On the other hand, in terms of cosmological parameters, the amplitude of these spectra in this regime is proportional to $A_s e^{-2\tau}$. The leverage on cosmological parameters gained through comparing the initial amplitude A_s to the growth-dependent lensing amplitude depends on how well τ is measured. In our experimental setup we assumed for simplicity that polarization information will be obtained for the full range of multipoles $\ell = 2 - 3000$, which results in a nearly cosmic variance limited constraint on τ of $\sigma(\tau) \approx 0.002$. This is about five times better than

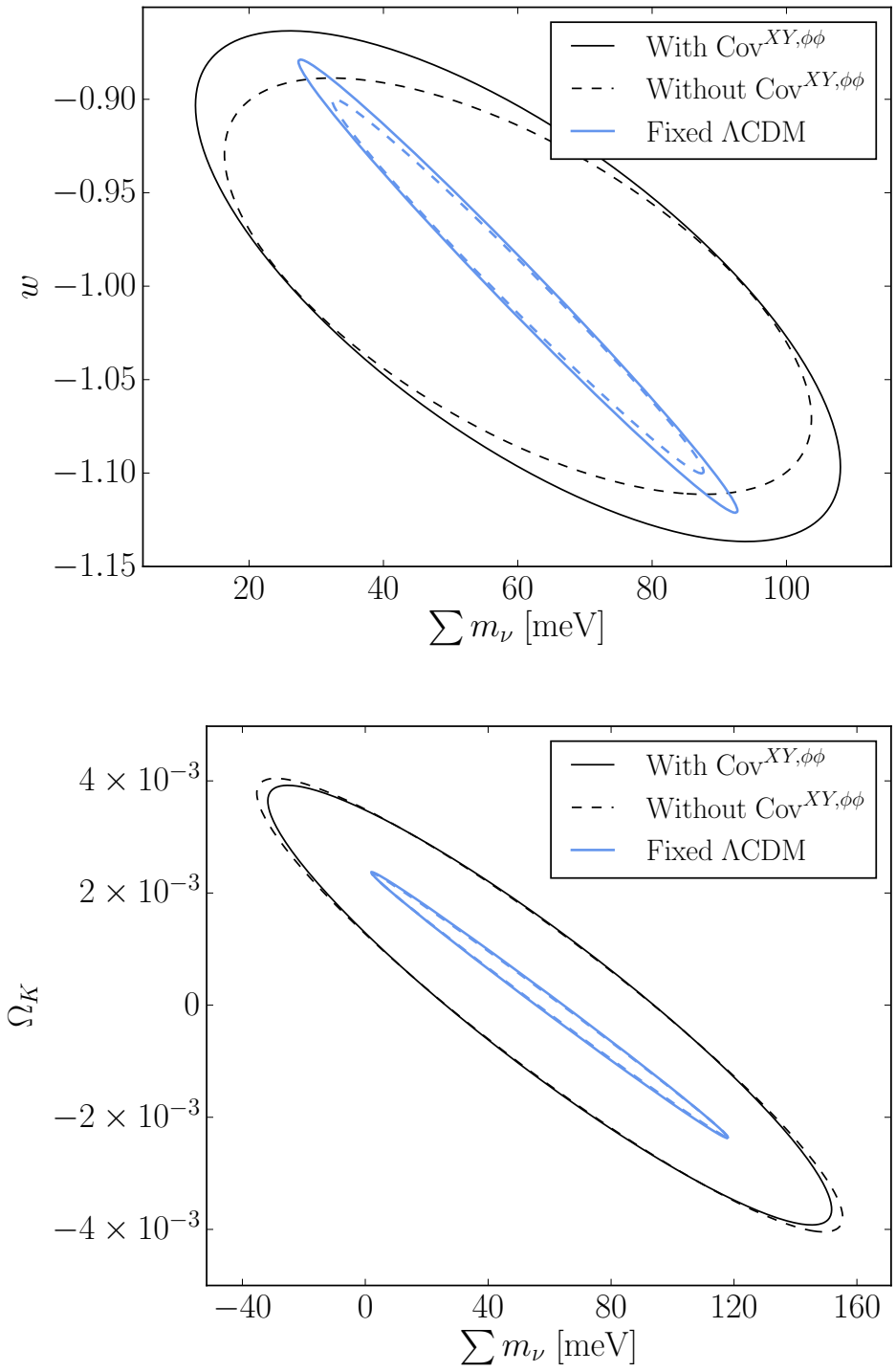

Figure 2.13: Forecasts for 2 parameter extensions to ΛCDM: w-$\sum m_\nu$ (top) and Ω_K-$\sum m_\nu$ (bottom). Black curves show $\Delta\chi^2 = 1$ constraints considering the full covariance (solid) and with covariances Cov$^{XY,\phi\phi}$ neglected (dashed); ΛCDM parameters are marginalized over. The blue curves show the same constraints with ΛCDM parameters fixed to their fiducial values.

current best constraints from Planck [44] and furthermore assume a fixed functional form for reionization [45, 46]. If the final Planck release does not improve these constraints to substantially below $\sigma(\tau) \sim 0.01$, this uncertainty will dominate the interpretation of lensing constraints for cosmological parameters [43, 47] since it will be difficult to improve using ground-based instruments.

More concretely, removing polarization data from $\ell < 30$ from our forecasts and replacing it with a prior of $\sigma_\tau = 0.01$, the errors in the worst constrained direction in Figure 2.13 do not significantly change, while those in the best constrained direction degrade by roughly a factor of two.

2.6 Discussion

Future measurements of lensed CMB temperature and polarization power spectra will be increasingly affected by the lens sample variance and this effect will have to be included into data analysis pipelines once polarization measurements approach the sample variance limit. We have developed such a pipeline, starting from simulated full sky lensed CMB maps with a CMB-S4 level instrumental noise and proceeding all the way through to constraints on cosmological parameters.

With this pipeline we investigated parameter constraints derived from simulated lensed CMB maps in our fiducial ΛCDM model with the lens sample variance effects either included or omitted. We obtain MCMC constraints on parameters of the ΛCDM as well as of its two extensions, ΛCDM+$\sum m_\nu$ and ΛCDM+w. The dominant effect of the lensing-induced covariance in all of the models is more than four-fold increase in variance of particular combinations of cosmological parameters M, M^ν, M^w. As a consequence, if the analysis of the real data was performed using Gaussian covariance in the likelihood, instead of the proper non-Gaussian covariance, there is a high chance of committing Type 1 error - mistakenly ruling out true cosmological model. This would potentially affect concordance studies comparing constraints from various datasets. Shifts in the best fit basis parameters and change

in constraints of the other parameter combinations are typically not as significant due to marginalization. The exception is ΛCDM+w where a significant degradation in the lower limit for w is manifest in the MCMC results. This degradation is hidden from the local Fisher forecasts as well as previous studies due to the strongly non-normal posterior distribution of w.

Using the Fisher forecast technique, we also investigated the impact on parameter constraints of covariances between the reconstructed lensing potential and the lensed power spectra. There is only a small effect within the ΛCDM model as its parameters are well constrained even without lensing. For extension with w and $\sum m_\nu$, double counting of the lensing information would lead to constraints overly optimistic by $\sim 20\%$, the extension with Ω_K and $\sum m_\nu$ shows much smaller effect of the lens sample variance on the marginalized constraints.

CHAPTER 3

DIRECT MEASUREMENTS OF $C_L^{\phi\phi}$

In this chapter we consider separately the cosmological information from gravitational lensing potential and from the unlensed CMB power spectra. We first use this way of thinking to explain the effects of the lens-induced covariance on constraints of the cosmological parameters that were discussed in the last section. Then we show how it enables us to compress the full information in the CMB temperature and polarization power spectra data into a small Gaussian likelihood, simplifying checks on some classes of cosmological models beyond ΛCDM in case deviations from ΛCDM are found. Separating the lensing information also allows us to directly measure the gravitational lensing potential from the CMB power spectra in a model-independent way. As we present in more detail at the end of this chapter, such direct measurements of $C_L^{\phi\phi}$ enable us to test consistency of lensing in the data and thus search for residual systematics and new physics.

3.1 Method

CMB information on a given cosmological parameter comes both from its effect on the unlensed CMB power spectra $C_\ell^{\tilde{X}\tilde{Y}}$ with $\tilde{X}\tilde{Y} \in \{\tilde{T}\tilde{T}, \tilde{T}\tilde{E}, \tilde{E}\tilde{E}, \tilde{B}\tilde{B}\}$ and on the lenses $C_L^{\phi\phi}$. It is conceptually useful to separate these two sources of information. Indeed, beyond the cosmological parameters considered in the previous chapter, the total information in the CMB observables is carried by all two point functions for $\tilde{T}, \tilde{E}, \tilde{B}, \phi$, assuming they obey Gaussian statistics; recovery of this complete set of information is the ultimate goal of the CMB delensing efforts.

In principle, the full implementation of this approach would be to consider every multipole in $C_\ell^{\tilde{X}\tilde{Y}}$ and $C_L^{\phi\phi}$ as a parameter in its own right. However, since the high redshift universe is well described by a ΛCDM-like model, we choose to parameterize the unlensed power spectra $C_\ell^{\tilde{X}\tilde{Y}}$ in terms of a small number of parameters $\tilde{\theta}_A$. These $\tilde{\theta}_A$ change the unlensed

power spectra in exactly the manner of the ΛCDM parameters θ_A, but unlike those, they have no effect on $C_L^{\phi\phi}$.

The lens power spectrum is instead described by a more complete set of parameters p_α, reflecting the wider range of possibilities during the acceleration epoch. For practical reasons, instead of considering each multipole $C_L^{\phi\phi}$ of the lensing potential as a parameter, we assume that the power spectrum is sufficiently smooth in L that we can approximate it with binned perturbations around the fiducial model. We then define a set of parameters p_α by

$$\ln C_L^{\phi\phi} \approx \ln C_L^{\phi\phi}\Big|_{\rm fid} + \sum_{\alpha=1}^{N_\phi} p_\alpha B_\alpha^{\phi,L}, \tag{3.1}$$

where $B_\alpha^{\phi,L}$ describes the binning and is defined as

$$B_\alpha^{\phi,L} = \begin{cases} 1 & L_\alpha \le L < L_{\alpha+1} \\ 0 & \text{otherwise} \end{cases}. \tag{3.2}$$

Expansion in $\ln C_L^{\phi\phi}$ is chosen to assure positivity of the power spectrum. Any cosmological model which predicts a smooth variation of $\ln C_L^{\phi\phi}$ from the fiducial model can be captured in these parameters as

$$p_\alpha = \frac{1}{\Delta L_\alpha} \sum_L B_\alpha^{\phi,L} \delta \ln C_L^{\phi\phi}, \tag{3.3}$$

where $\Delta L_\alpha = L_{\alpha+1} - L_\alpha$ is the width of bin α. We consider uniform binning with bins of width 5 in this work; we do not expect binning to have any effect on our conclusions. Changes to the lensing potential are allowed up to $L = 5000$, given by the L range in which we assume the reconstruction data are measured.

The largest set of parameters which we will consider is then

$$P_{\rm tot} = \{\tilde\theta_1, \tilde\theta_2, \dots, p_1, p_2, \dots\}, \tag{3.4}$$

where $\tilde{\theta}_A$ only affect the unlensed power spectra and p_α only affect the lensing potential. A given cosmological parameter θ_A jointly changes $\tilde{\theta}_A$ and p_α.

In models beyond ΛCDM, changes in the integrated Sachs-Wolfe (ISW) effect would typically affect data on the largest scales. In this work, we are interested only in lensing-like effects and leave the ISW contribution at its ΛCDM value. To fully represent a cosmological parameter we would also have to account for the covariance between the lens power spectrum and the unlensed CMB spectra induced by $C_\ell^{\tilde{T}\phi}, C_\ell^{\tilde{E}\phi}$ – the ISW-lens and reionization-lens correlations respectively. We could in principle add these as parameters to form a complete description. However, these appear only on the largest, severely cosmic variance limited scales which will also be difficult to extract due to foregrounds and systematics. For this reason we completely neglect the cosmological information contained in them.

3.2 Principal component implementation

There are practical obstacles to measuring the full lensing power spectrum $C_L^{\phi\phi}$ through p_α from the temperature and polarization power spectra XY alone, given the many ill-constrained modes. In this section, we re-examine the lensing principal component decomposition introduced in Ref. [43] and show that a small set of parameters completely characterizes the lensing information in the XY data.

The forecasted covariance matrix of the p_α lensing parameters as measured by XY power spectra is given by inverse of the Fisher matrix

$$F_{\alpha\beta}^{\rm TEB} = \frac{\delta_{\alpha\beta}}{\sigma_{p_\alpha}^2} + \sum_{\substack{\ell,\,\ell' \\ XY,\,WZ}} \frac{\partial C_\ell^{XY}}{\partial p_\alpha} \left({\rm Cov}_{\ell\ell'}^{XY,WZ}\right)^{-1} \frac{\partial C_{\ell'}^{WZ}}{\partial p_\beta}. \tag{3.5}$$

Because the XY power spectra provide only integrated constraints on $C_L^{\phi\phi}$, we imposed a mild theoretical prior of $\sigma_{p_\alpha} = 1$ to forbid numerical problems and degeneracies induced by unphysically large features in $C_L^{\phi\phi}$.

The orthonormal eigenvectors $K_\alpha^{(i)}$ of this covariance matrix represent an alternate basis for the measurements

$$\Theta^{(i)} = \sum K_\alpha^{(i)} p_\alpha, \tag{3.6}$$

that in principle yield uncorrelated parameters, rank ordered by their variance. By keeping only the eigenvectors that are predicted to have low variance, we can measure the relevant information with a much smaller set of principal components (PCs).

The efficiency of the PC approach depends on the number of components needed to completely characterize the relevant information. For the experimental configuration considered here, we find eigenvalues

$$10^3\lambda \;=\; 1.0, 4.0, 12, 19, 93, \ldots, \tag{3.7}$$

which indeed shows that relative importance of the components decreases rapidly; only a few PCs are constrained better than the $\sigma_{p_\alpha} = 1$ prior.

The lensing PCs, $\Theta^{(i)}$, can be thought of as a more incisive generalization of the standard approach where a scaling parameter $C_L^{\phi\phi} \to A_L C_L^{\phi\phi}$ is added to test consistency of a model with lensing; PCs parametrize the lensing information more completely. Moreover, the PCs decouple the information on the lensing power spectrum from the parameters that control the unlensed spectrum, whereas A_L multiplies a $C_L^{\phi\phi}$ that depends on such parameters. PCs can therefore be more directly compared with other measurements of $C_L^{\phi\phi}$, most notably from lensing reconstruction using the higher point information in the temperature and polarization fields themselves (see Section 3.5 and the next Chapter).

The five most important components for the considered experimental configuration are shown in Figure 3.1. The low order modes peak where the lenses have their largest impact on XY and the higher modes are increasingly oscillatory, because they have to be orthogonal to the more important eigenmodes. For practical applications it is sufficient to keep only several best constrained principal components to characterize the impact of lensing in the

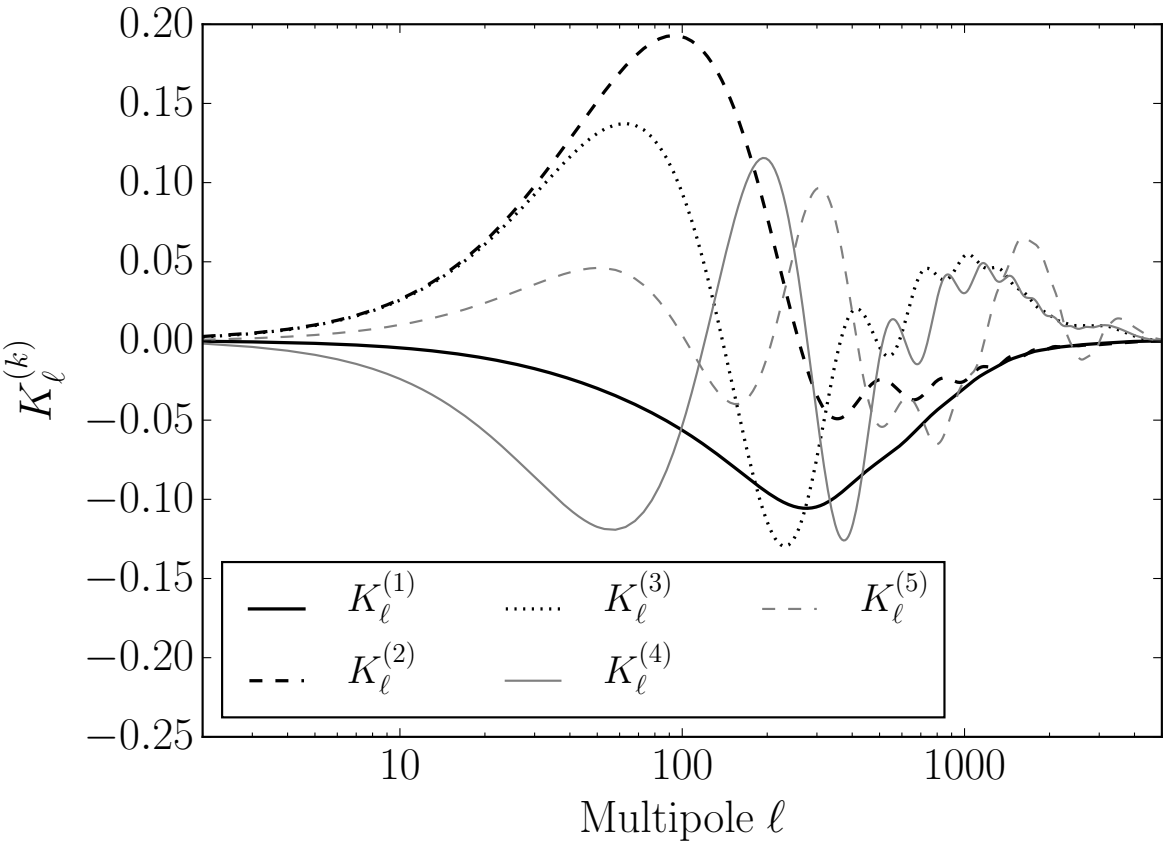

Figure 3.1: Five principal components $K_\ell^{(i)}$ of the lensing potential best measured by the lensed power spectra for our mock CMB-S4-like experiment.

XY power spectra. For reasons detailed in Appendix C, the 5 best measured PCs suffice for the data and models considered here.

As we introduce the lens principal components using a Fisher forecast, their properties need to be validated on numerical simulations. To achieve this, we run MCMC analyses on 50 independent lensed CMB sky simulations to determine properties of the parameters $\tilde{\theta}_A, \Theta^{(i)}$ and also to check our likelihood model. The simulations, analysis techniques and the likelihood we are using are explained in detail in Section 2.3.

This check is nontrivial, as so far we have made numerous assumptions. For example, we assumed that our models for the likelihood and non-Gaussian covariance are correct, that the Fisher-based construction of the PCs suffices, that neglecting higher $\Theta^{(i)}$ does not

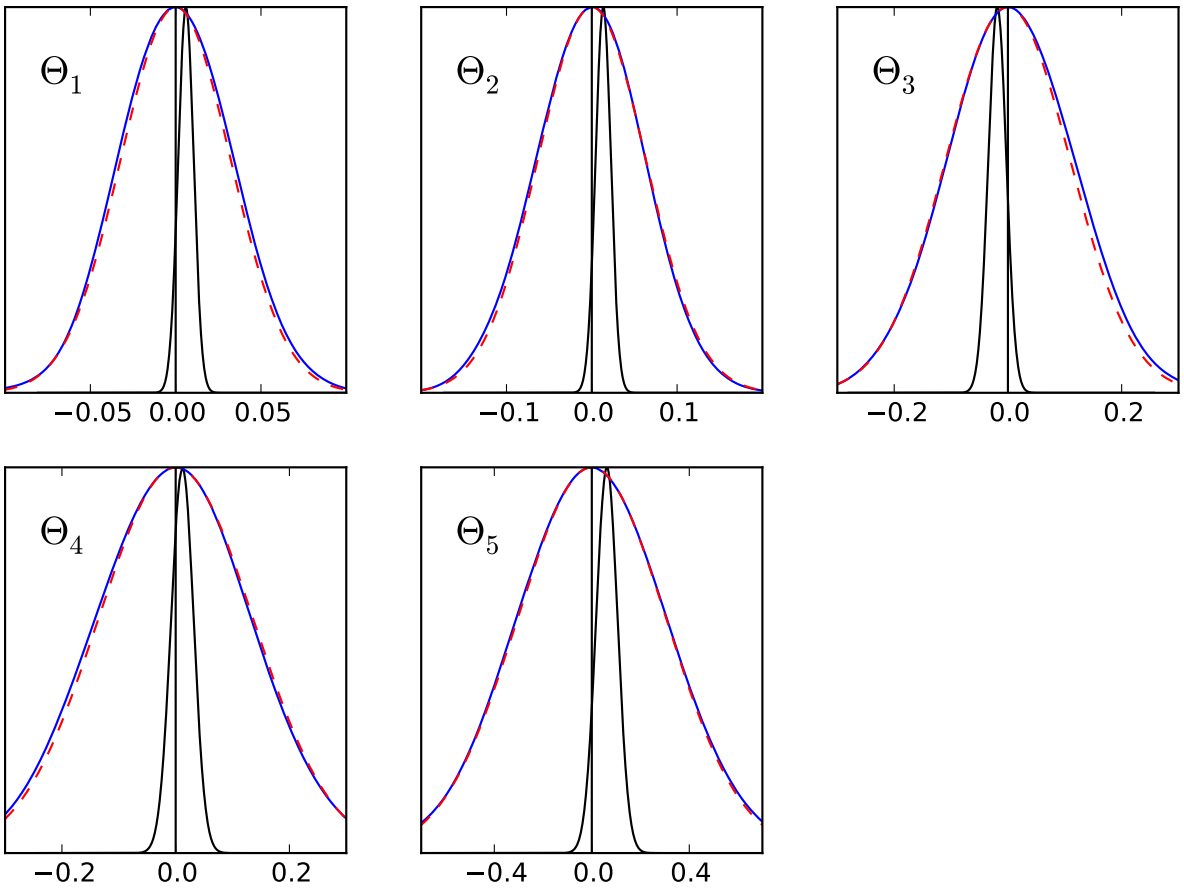

Figure 3.2: Joint posterior distribution for PCs $\Theta^{(1-5)}$ (black) as a product of the individual posteriors from 50 independent all-sky simulations. The joint posterior is unbiased to a small fraction of the width of the distribution of a single simulation (blue) and its Fisher prediction (red dashed).

affect the constraints and that agreement between theoretical and simulated power spectra is sufficient (see Appendix A). It is thus an important check of our analysis to ascertain that the constraints on $\Theta^{(i)}, \tilde{\theta}_A$ are unbiased with respect to the fiducial model. To verify this, we multiplied 50 MCMC posterior probabilities for $\Theta^{(i)}, \tilde{\theta}_A$. The results for $\Theta^{(i)}$ are shown in Fig. 3.2 and show no significant bias relative to the standard deviation of a single MCMC posterior; the same conclusion is valid also for $\tilde{\theta}_A$.

The Fisher analysis also predicts that $\Theta^{(i)}$ as determined by the data should be uncorrelated. This assertion can be checked by averaging covariance matrix of the cosmological parameters $\Theta^{(i)}, \tilde{\theta}_A$ over the MCMC analyses. Correlation coefficients of $\Theta^{(i)}$ obtained from

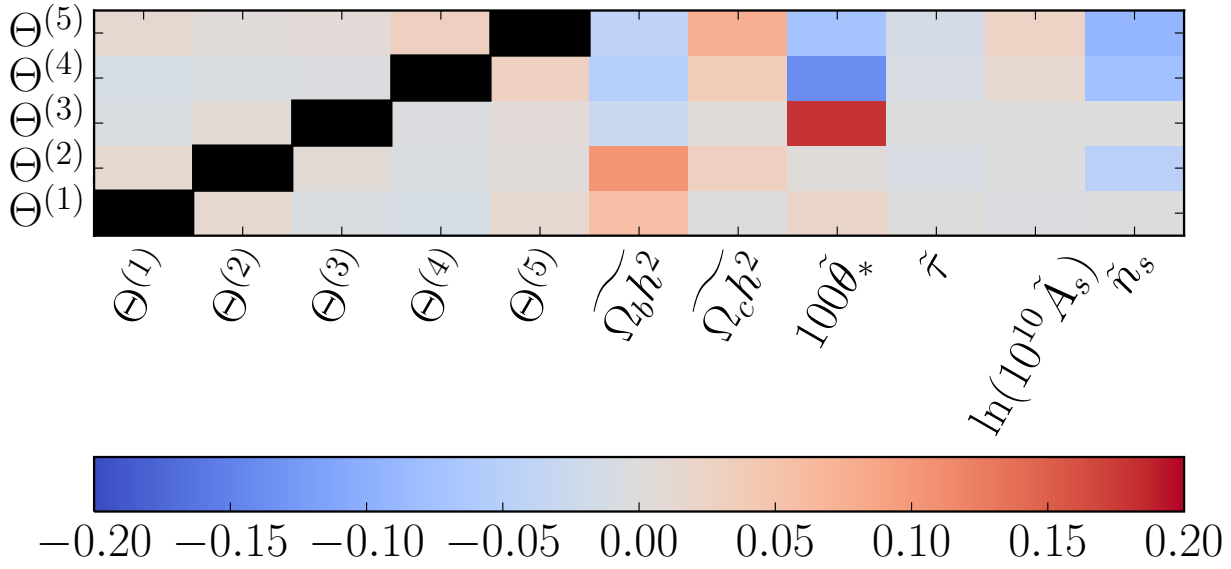

Figure 3.3: Correlation matrix for $\Theta^{(i)}$ averaged over 50 MCMC analyses. Black squares represent ones on the diagonal. The tilded parameters affect only the unlensed CMB, as explained in the text.

this covariance matrix are shown in Fig. 3.3. As expected, the lensing principal components are only very weakly mutually correlated. Additionally, they are also only mildly correlated with the unlensed parameters $\tilde{\theta}_A$. Most significant of these are $R = 0.18$ correlation between $\Theta^{(3)}$ and θ_* and $R = -0.14$ correlation between $\Theta^{(4)}$ and θ_*. This is somewhat counter-intuitive, as θ_* shifts the angular scale of acoustic features whereas lensing mainly smears the peaks by superimposing magnified and demagnified regions. While largely true, the effect of lenses that are on scales smaller than the acoustic scale $\ell \gtrsim 200$ is not purely a smearing effect, causing a component that is slightly out of phase with the peaks in the unlensed power spectra, leading to the observed correlation.

The full results for all pairs of the 11 parameters in a single simulation are shown in Fig. 3.4. Note that the posterior distribution for the parameters $\Theta^{(i)}, \tilde{\theta}_A$ seems to be very well approximated by a multivariate normal distribution. This implies that the Fisher approximation should be quite accurate in this space as we explicitly verify in Fig. 3.2. We exploit the multivariate normal nature of the posterior in the $\Theta^{(i)}, \tilde{\theta}_A$ variables in Section 3.4.

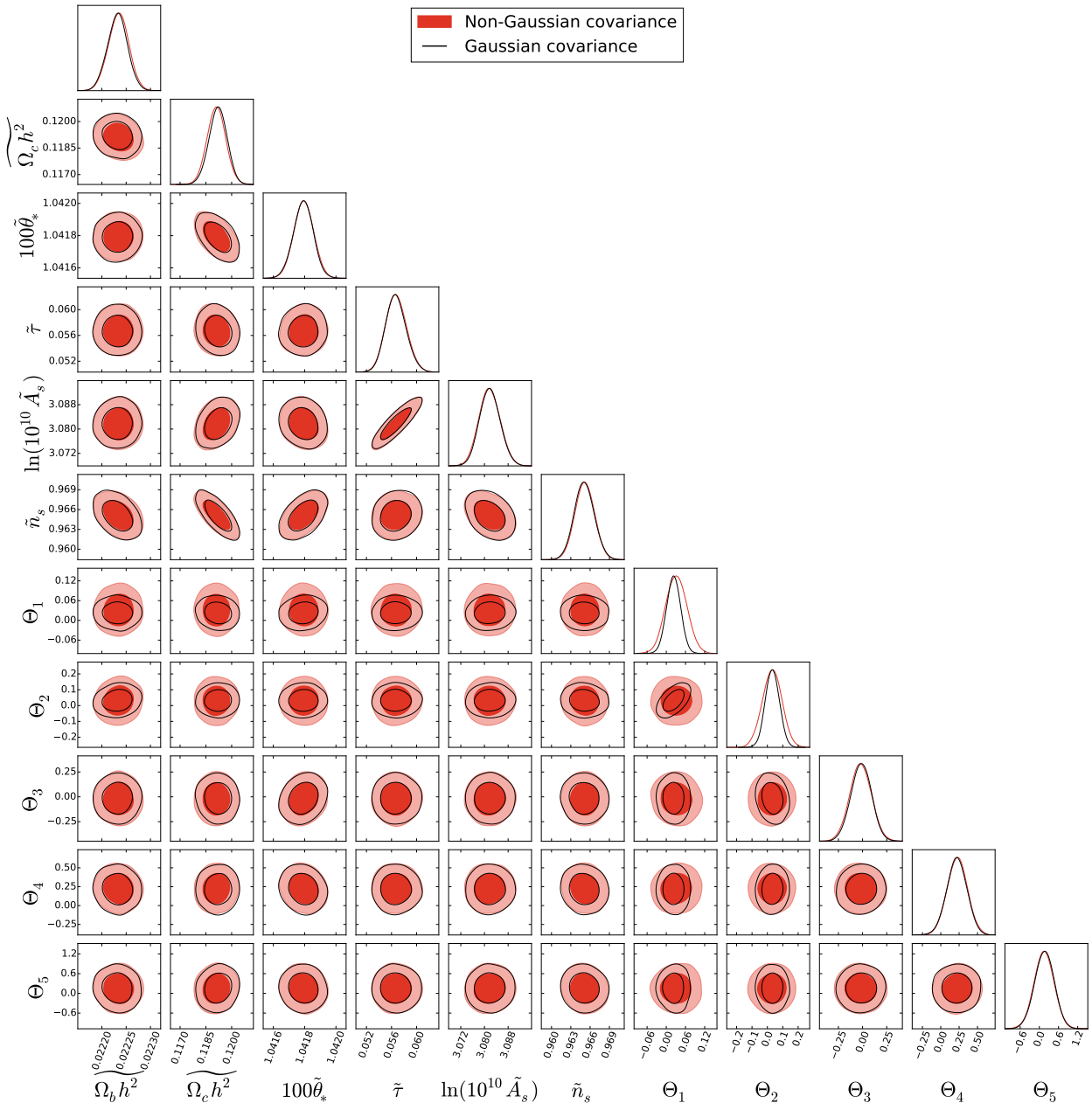

Figure 3.4: MCMC constraints on the lens and unlensed parameters $\Theta^{(i)}, \tilde{\theta}_A$ in a typical simulation with a Gaussian (black curves) and non-Gaussian covariance (red shaded) analysis.

3.3 Explaining lens-sample covariance effects on parameter constraints

In this section we use the insights gained from separating information from the unlensed CMB, as parameterized in terms of $\tilde{\theta}_A$, and from the gravitational lensing to explain effects of the lens-sample covariance on cosmological parameter constraints, investigated in Sections 2.4 and 2.5

3.3.1 Temperature and polarization power spectra

In Fig. 3.4 we additionally show the effect of the non-Gaussian covariance in the 11D lens and unlensed parameter space; only $\Theta^{(1)}$ and $\Theta^{(2)}$ show significant effects of neglecting the non-Gaussian likelihood. These two measurements are strongly affected, because significant portion of the noise in these measurements arises from the sample variance of the lenses. Neglecting lensing-induced terms in the data covariance effectively omits this noise contribution, which leads to overly optimistic estimates on $\Theta^{(1)}, \Theta^{(2)}$. Measurements of other lensing principal components and $\tilde{\theta}_A$ are limited by other sources of noise – instrumental noise and cosmic variance of the unlensed CMB – and the resulting constraints are thus not strongly affected by the non-Gaussian part of the covariance.

If the eleven parameters $\Theta^{(i)}, \tilde{\theta}_A$ contain all information about a particular cosmological model, a Karhunen-Loève (KL) analysis [1] applied to the Fisher information matrices reveals that non-Gaussian covariances can degrade the standard deviation of any linear combination of these parameters by maximally 2.53.[2] This generalizes the discussion of the most degraded linear combination M of cosmological parameters from Section 2.4. This PC based quantification of the effect of non-Gaussian covariances is not restricted to the models inves-

1. The KL transform is often used in cosmology to define signal-to-noise eigenmodes for optimal data compression [48, 49, 50]; our use follows [43] in comparing information in two different covariance matrices.

2. Using covariance matrices of $\Theta^{(i)}, \tilde{\theta}_A$ from 10 MCMC simulations we checked this prediction is on average correct to ± 0.04.

tigated here and can be applied to more general extensions of ΛCDM. It is also not necessary to assume a *linear* relationship between these effective parameters and the bare cosmological parameters, or the validity of the Fisher approximation for the latter.

Moreover, we can use $\Theta^{(1,2)}$ to directly translate the effect of lensing-induced covariance on cosmological parameter constraints. Those combinations of cosmological parameters which are limited by our knowledge of $\Theta^{(1,2)}$, in other words those constrained by the (mostly low ℓ) lensing information, will be strongly affected if we neglect the non-Gaussian covariance.

For example in ΛCDM, lensing information helps mainly ω_c and A_s constraints. Increasing either of these parameters increases $C_L^{\phi\phi}$, lensing information thus helps constrain the direction of simultaneously increasing ω_c and A_s. As we can see in Fig. 2.5, adding non-Gaussian covariance weakens exactly this parameter combination the most. The reason becomes clear when we examine how change in the parameter combination M, the most sensitive to the non-Gaussian covariances, projects onto the changes in the effective parameters $\Delta\Theta^{(i)}, \Delta\tilde{\theta}_A$. As expected, the main effect is a shift in $\Theta^{(1)}, \Theta^{(2)}$, which are the variables showing most of the effect of the non-Gaussian covariance; this shift is captured in Fig. 3.5. In comparison, shifts in the other effective parameters $\Theta^{(i)}, \tilde{\theta}_A$ are at least a factor of few smaller, as measured by the sizes of the marginalized posterior. This means that already within ΛCDM it is possible to construct a parameter combination which has a dominant effect of changing the lensing potential $(\Theta^{(1)}, \Theta^{(2)})$ and keeps the unlensed power spectra $(\tilde{\theta}_A)$ relatively intact. Because of that, the relative change in the standard deviation for M brought about by the non-Gaussian covariance, 2.03, is already close to the maximal possible value of 2.53.

By extending the cosmological model to ΛCDM+$\sum m_\nu$, we increase the parameter freedom, which enables us to find a parameter combination which is slightly more limited by the lens sample covariance and shows degradation of 2.05. From the perspective of the effective parameters $\Theta^{(i)}, \tilde{\theta}_A$ this occurs because it is possible to achieve the same change of the

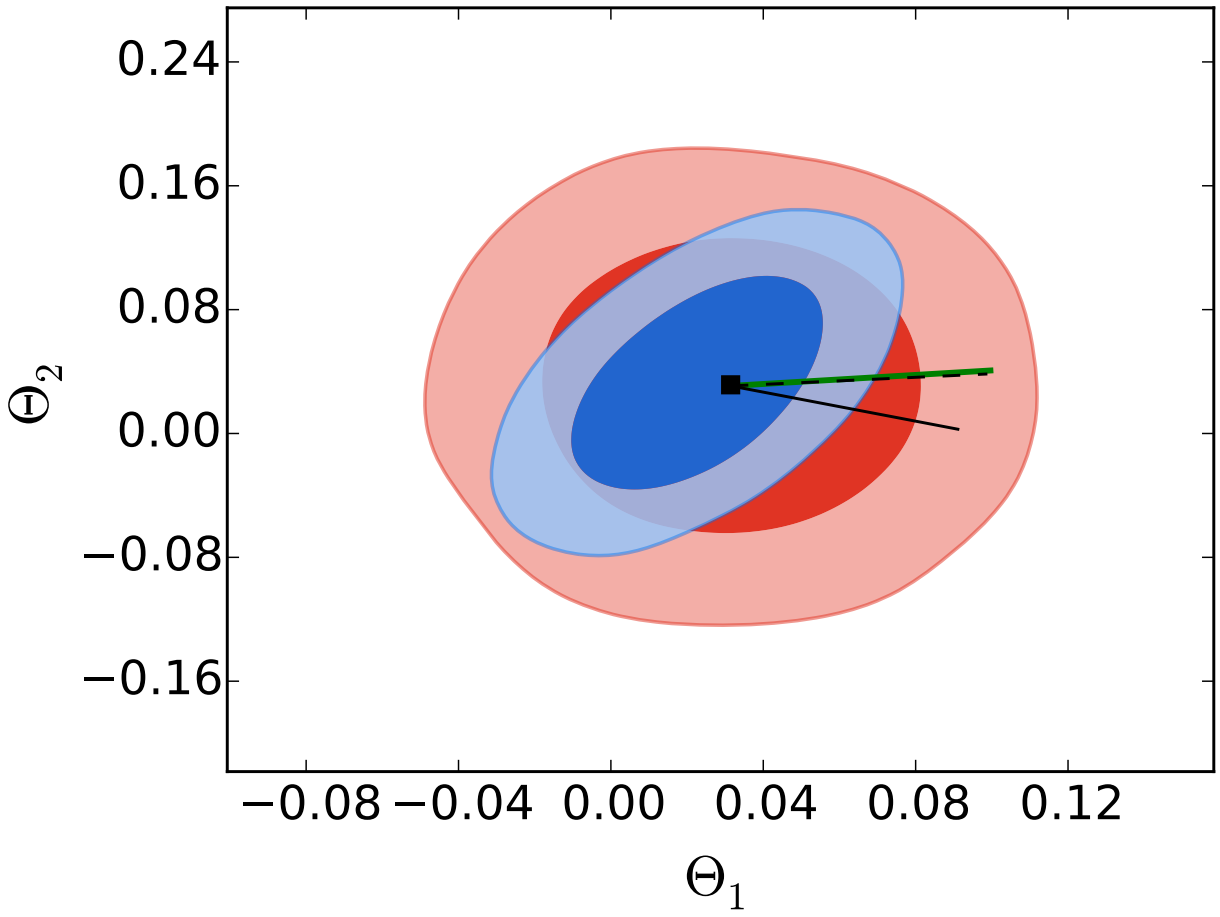

Figure 3.5: Lines show how $\Theta^{(1)}$ and $\Theta^{(2)}$ change when we increase M (black dashed), M^{ν} (green) or M^{w} (black solid); length of the lines is arbitrary. For comparison, in the background we show typical constraints on these two parameters in an MCMC analysis based on non-Gaussian (red) and Gaussian (blue) covariance.

lensing potential, as seen in the nearly identical directions of M and M^ν in Fig. 3.5, with a smaller change in the unlensed power spectra. This increases relative importance of the low ℓ lensing information $\Theta^{(1)}, \Theta^{(2)}$ in constraining M^ν, which directly leads to a larger impact of non-Gaussian covariance.

Moreover, lensing information is now important for three parameters $\{\omega_c, A_s, \sum m_\nu\}$ unlike two in ΛCDM. Because the degeneracy structure involves three parameters, the non-Gaussian effect is hidden from the covariance of any two, once the third is marginalized. In a three-dimensional likelihood for these three parameters, the effect of non-Gaussian covariance is clearly visible.

For ΛCDM+w the analysis is similar. Again, by adding a new parameter on top of ΛCDM we can find M^w which shows degradation larger than what is seen in ΛCDM, in this case 2.28. For ΛCMD+w this happens, because the projection of M^w onto $\{\Theta^{(1)}, \Theta^{(2)}\}$ is more aligned with the direction maximally impacted by the non-Gaussian covariance, see Fig. 3.5.

3.3.2 Adding lensing reconstruction

As we discuss in the previous section, variance of two $C_L^{\phi\phi}$ modes measured by the temperature and polarization power spectra in our mock CMB-S4 experiments are strongly affected by the lens sample variance. Lensing reconstruction will achieve comparable or better measurement precision and cross-correlation between the two kinds of data then has to be included to avoid double counting of the common lensing information. Failing to do so would affect those conclusions for which measurements of these two $C_L^{\phi\phi}$ modes are important.

We can understand the different parameter behaviors seen in Fig. 2.13 by examining the impact of parameters on p_α or $\ln C_L^{\phi\phi}$ (see Fig. 3.6). Although the measurements determine the amplitude of the $C_L^{\phi\phi}$ well at $L \gtrsim 500$, they are unable to separate out the contributions from the various cosmological parameters. In particular, linear combinations of $\ln A_s$ and $\Omega_c h^2$ can mimic the impact of the extended ΛCDM parameters [43]. Therefore, while the

best constrained direction in the 2-dimensional extended spaces correspond to combinations of the parameters that coherently change $C_L^{\phi\phi}$ at $L \gtrsim 500$, the constraint itself is limited by how well $\ln A_s$ and $\Omega_c h^2$ are measured not by how well $C_L^{\phi\phi}$ is measured (see Fig. 2.13). The degenerate or worst constrained direction corresponds to when the parameter variations cancel in their effect.

At $L \lesssim 500$ the degeneracy between w and $\sum m_\nu$ observed at high L starts to break, which allows us to meaningfully constrain also the perpendicular direction in the parameter space. These are the scales where the $\Theta^{(1)}$ and $\Theta^{(2)}$ get significant contribution (Fig. 3.1), which explains why the lens-induced covariance effects are important for this parameter combination.

For Ω_K and $\sum m_\nu$ this degeneracy breaking is noticeably weaker, especially at $L \gtrsim 50$. Given the large sample variance associated with the lowest multipoles, the limiting source of information in the degenerate direction in the $\Omega_K - \sum m_\nu$ plane comes from the unlensed CMB rather than the lensing information. Hence, the effect of lens sample covariance is smaller in this case.

Finally, for these issues that relate to parameter degeneracies, it is important to remember that external information from measurements beyond the CMB, for example from baryon acoustic oscillations, can break these degeneracies and allow more of the information on $C_L^{\phi\phi}$ (especially that at $L > 500$) to be used for parameter constraints.

3.4 Effective likelihood for model building

Given the nearly multivariate normal posterior probability of the effective parameters $d_a = \{\tilde{\theta}_A, \Theta^{(i)}\}$, we can use a single MCMC analysis to compress the whole CMB power spectra data into 11 numbers for the mean values $\bar{d}_a$ and the 11×11 covariance matrix of d_a. These

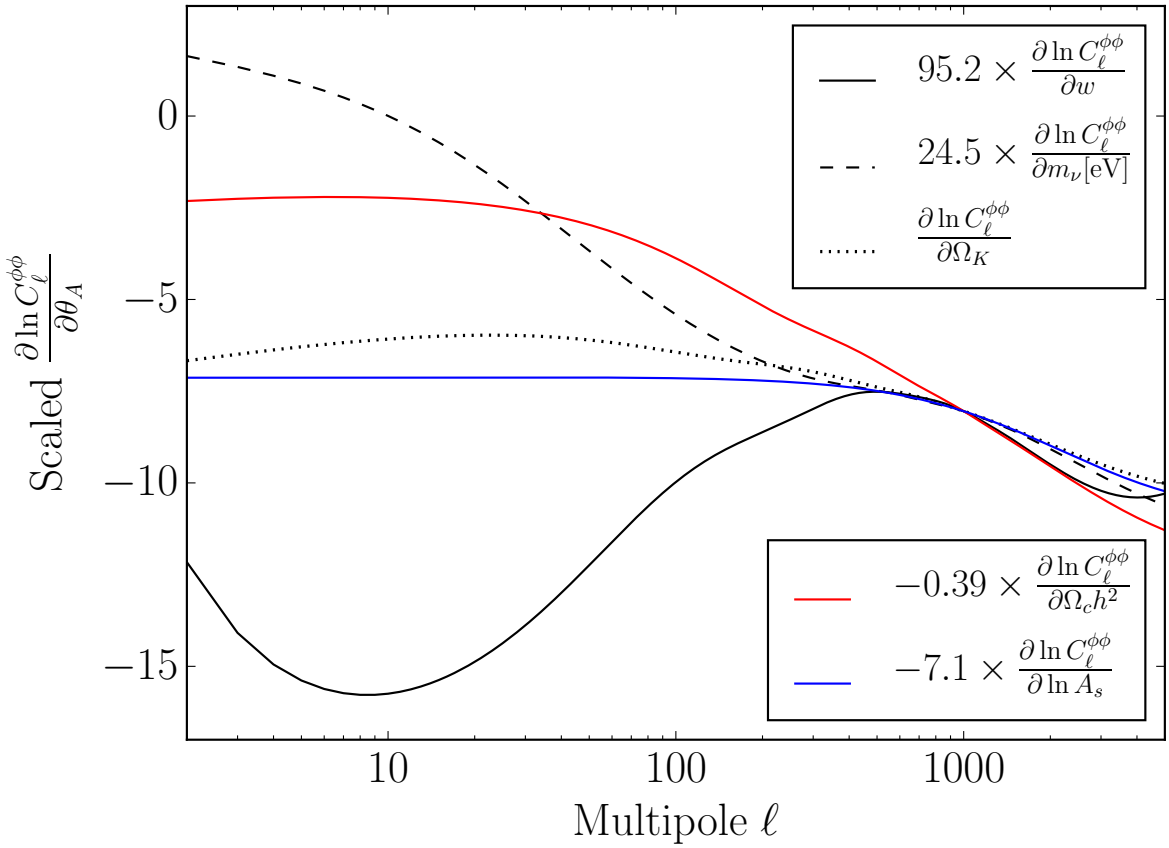

Figure 3.6: Derivatives of $\ln C_\ell^{\phi\phi}$ with respect to cosmological parameters $w, \sum m_\nu, \Omega_K, \Omega_c h^2$, $\ln A_s$ normalized at $\ell = 1000$ to highlight degeneracies. These derivatives are taken at fixed acoustic scale θ_*.

can be used to form an effective likelihood function $\mathcal{L}_{\rm eff}(\bar{d}_a|\theta_A)$ defined as

$$-2\ln\mathcal{L}_{\rm eff} = \sum_{ab}[\bar{d}-d(\theta_A)]_a(\mathrm{Cov}_d^{-1})_{ab}[\bar{d}-d(\theta_A)]_b. \tag{3.8}$$

Here $d_a(\theta_A)$ models the expectation values for the data $\bar{d}_a$ as a function of the cosmological parameters θ_A of a given cosmological model. This effective likelihood can be now used to probe a broad class of cosmological models without any explicit use of the raw CMB power spectra data by specifying $d_a(\theta_A)$ for each such model. Class of models for which this approach is effective contains not just ΛCDM+w and ΛCDM+$\sum m_\nu$ considered here but also models which are indistinguishable from ΛCDM at recombination and for which CMB lensing is the dominant source of information on the physics beyond ΛCDM. For example, many models of dark energy and modified gravity fall into this class, if we are willing to ignore the extra information coming from the integrated Sachs-Wolfe effect and other secondaries. In principle, the technique can be extended to incorporate such effects by extending the set of unlensed parameters $\tilde{\theta}_A$.

In the context of model building, one can envision a scenario where ΛCDM parameters produce a poor effective likelihood for the data and motivate extensions beyond ΛCDM. The effective likelihood can then be used as a quick spot check as to whether the given extension improves the fit.

Let us illustrate this technique on ΛCDM+w and ΛCDM+$\sum m_\nu$. First, it is necessary to find the functional dependence of d_a on the cosmological parameters θ_A. The values of the unlensed parameters $\tilde{\theta}_A$ for $A \in \{\theta_*, \Omega_c h^2, \Omega_b h^2, n_s, \ln A_s, \tau\}$ are the same as the true cosmological parameters θ_A, while the values of the lensing principal components $\Theta^{(i)}$ can be determined directly from the definition (3.20) given $C_L^{\phi\phi}(\theta_A)$ alone. The full parameter space of the given extension can then be explored with an MCMC in the general case where $d_a(\theta_A)$ is nonlinear across the allowed region of the parameter space as in the ΛCDM+w extension. In a case such as ΛCDM+$\sum m_\nu$, where the mapping can be linearized, it is possible to get

a good estimate of parameter constraints even without performing any additional MCMC.

In Fig. 3.7 we show comparison of ΛCMD+w parameter constraints obtained in the analysis presented in the previous paragraph against results of the standard MCMC analysis. Because the mapping onto the effective parameter space is non-linear, it is necessary to perform an additional MCMC run. Note that this mapping alone accounts for most of the non-normal posterior probability in the (ω_c, w) plane despite being based on a normal distribution for the effective parameters. It slightly underestimates the lower limit on w, presumably due to the neglect of the integrated Sachs-Wolfe effect in the unlensed parameters. For ΛCDM+$\sum m_\nu$, the agreement between the simplified and standard analyses is even better.

3.5 Lensing consistency checks

The ability to directly measure $C_L^{\phi\phi}$ from the CMB power spectra allows us to check consistency of lensing in the CMB data. In this section we comment on various approaches utilizing this possibility.

3.5.1 Internal consistency of a model

One possible test of lensing consistency is based on comparing lensing potential measured directly from the data – in practice through the lens PCs $\Theta^{(i)}$ – against what is expected in a given cosmological model based on constraints of the unlensed parameters $\tilde{\theta}_A$. This test mainly checks the internal consistency of the model assumptions. In the next chapter we demonstrate a practical application of this approach using the Planck satellite data.

3.5.2 Comparing data sets

Direct measurements of the gravitational lensing potential also allow us to check mutual lensing consistency between CMB temperature and polarization power spectra and those

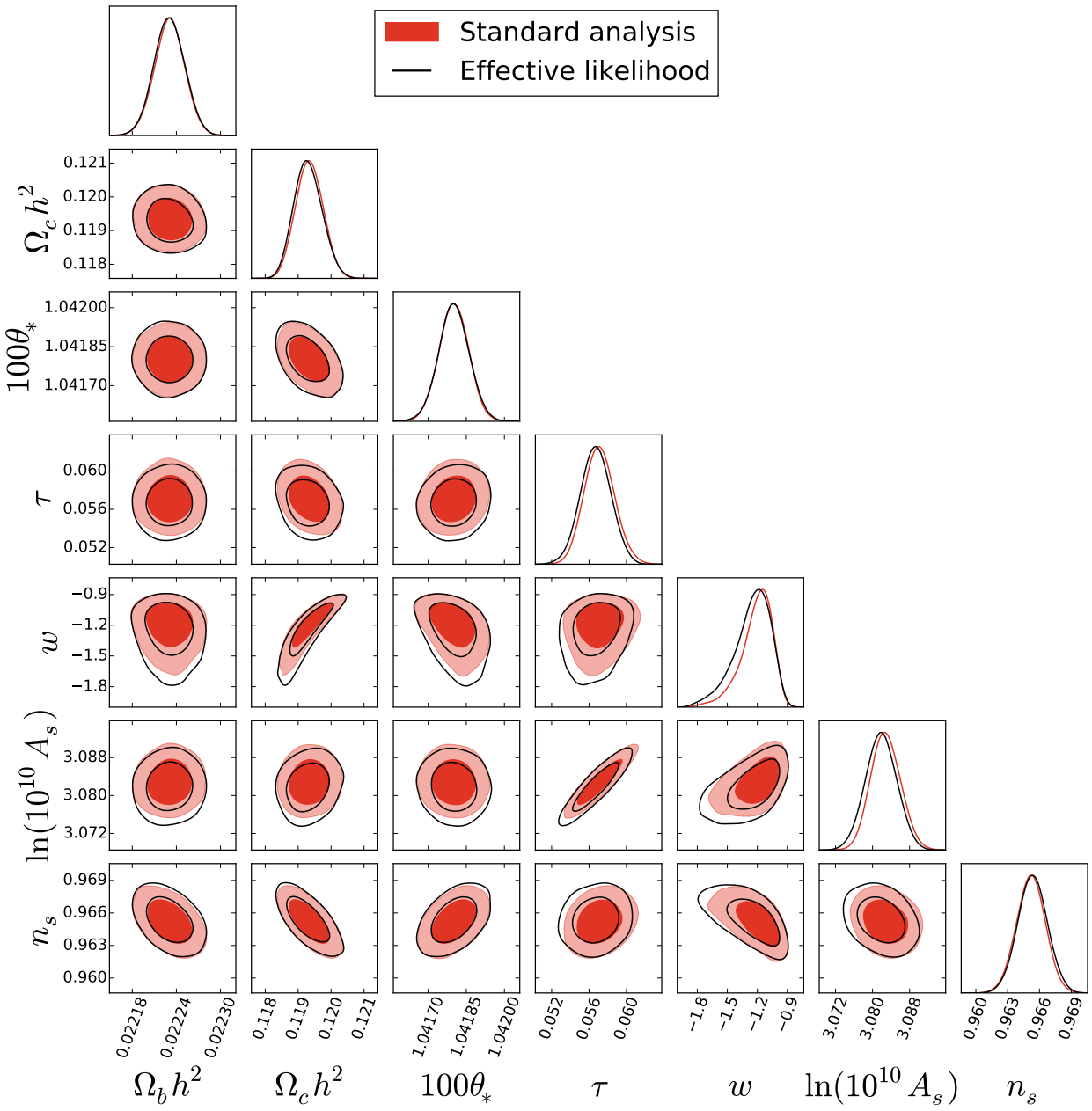

Figure 3.7: Comparison of constraints on ΛCDM+w parameters from the standard analysis (red shaded) with results of an approximate analysis based on the effective likelihood of $\{\Theta^{(i)}, \tilde{\theta}_A\}$ instead of the raw CMB data (black).

from lensing reconstruction by comparing constraints on the lens PCs $\Theta^{(i)}$ from these two sources of information. Further subdivisions of the data, such as comparing constraints from C_ℓ^{TT} and C_ℓ^{BB}, are possible and provide additional checks. If discrepancies are found, they may indicate systematic errors in the experiment or the data analysis technique. By checking for consistency at the power spectra level, one can provide proof against such problems before making incorrect cosmological inferences. As we show in the next chapter, Planck satellite lensing reconstruction and power spectra data are mutually inconsistent with moderate statistical significance.

3.5.3 Maximally covarying modes

In principle, the most inclusive lensing consistency test between the XY and lensing reconstruction data would be to compare their respective constraints on $\Theta^{(i)}$ in a multidimensional space, taking into account mutual correlations between these measurements. However, most of the power of this consistency check will be carried by the "consistency modes", which are the $\ln C_L^{\phi\phi}$ modes – linear combinations of the lens parameters p_α (3.1) – whose measurements are the most affected by the cross-correlation between XY and lensing reconstruction. These are the modes which are the most limited by the common sample variance of the lenses and thus provide the cleanest consistency check. By construction, these consistency modes are (at the Fisher forecast level) uncorrelated and can be thus investigated independently, which allows for a simpler analysis. In this section we show their construction and properties for an experiment observing the full sky.

To find these consistency modes we use the Karhunen-Loève (KL) transform. We consider two versions of the Fisher matrix for p_α,

$$F_{\alpha\beta}^{\text{lenses}} = \sum_{\substack{\ell,\ell' \\ xy,wz}} \frac{\partial C_\ell^{xy}}{\partial p_\alpha} \left(\text{Cov}_{\ell\ell'}^{xy,wz}\right)^{-1} \frac{\partial C_{\ell'}^{wz}}{\partial p_\beta} \tag{3.9}$$

and

$$F^{-,\mathrm{lenses}}_{\alpha\beta} = F^{\mathrm{lenses}}_{\alpha\beta}\Big|_{\mathrm{Cov}^{XY,\phi\phi}_{\ell\ell'}=0}, \tag{3.10}$$

the same construction but with the $\mathrm{Cov}^{XY,\phi\phi}$ covariance artificially set to zero. The corresponding covariance matrices are

$$\begin{aligned} \mathrm{Cov}^{\mathrm{lenses}}_{\alpha\beta} &= [F^{\mathrm{lenses}}_{\alpha\beta}]^{-1} & (3.11)\\ \mathrm{Cov}^{-,\mathrm{lenses}}_{\alpha\beta} &= [F^{-,\mathrm{lenses}}_{\alpha\beta}]^{-1}. & (3.12) \end{aligned}$$

We can now perform a KL transformation by finding all solutions to the generalized eigenvalue problem

$$\sum_\beta \mathrm{Cov}^{\mathrm{lenses}}_{\alpha\beta} v^{(k)}_\beta = \sum_\beta \lambda^{(k)} \mathrm{Cov}^{-,\mathrm{lenses}}_{\alpha\beta} v^{(k)}_\beta. \tag{3.13}$$

Here $v^{(k)}_\beta$ and $\lambda^{(k)}$ are the KL eigenvectors and eigenvalues. The KL transform of the measurements

$$\Psi^{(k)} = \sum_\alpha v^{(k)}_\alpha p_\alpha \tag{3.14}$$

provides a representation that is uncorrelated, or statistically orthogonal, with respect to both covariance matrices since solutions to (3.13) are simultaneously orthogonal with respect to the metrics defined by the covariance matrices

$$\begin{aligned} \mathrm{Cov}_{\Psi^{(k)}\Psi^{(l)}} = \sum_{\alpha\beta} v^{(l)}_\alpha \mathrm{Cov}^{\mathrm{lenses}}_{\alpha\beta} v^{(k)}_\beta &= \lambda^{(k)}\delta_{kl},\\ \mathrm{Cov}^{-}_{\Psi^{(k)}\Psi^{(l)}} = \sum_{\alpha\beta} v^{(l)}_\alpha \mathrm{Cov}^{-,lenses}_{\alpha\beta} v^{(k)}_\beta &= \delta_{kl}. \end{aligned} \tag{3.15}$$

We order $\lambda^{(k)}$ to be decreasing with k and hence in the ratio of the variances between the two, i.e. the degradation in the constraints due to $\mathrm{Cov}^{XY,\phi\phi}_{\ell\ell'}$. Note that this differs from the principal component basis in that it rank orders modes by whether the joint measurements are noise or lens sample variance dominated rather than by total variance from XY.

The KL eigenvectors are not necessarily mutually orthonormal in the ordinary Euclidean sense,

$$\sum_{\alpha} v_{\alpha}^{(l)} v_{\alpha}^{(k)} \neq \delta_{kl}, \tag{3.16}$$

as are the eigenvectors in the principal component representation. Consequently, the forward and inverse KL transforms are distinct:

$$p_{\alpha} = \sum_{k} w_{\alpha}^{(k)} \Psi^{(k)}, \tag{3.17}$$

where $w_{\alpha}^{(k)}$ is the matrix inverse of $v_{\alpha}^{(k)}$ rather than its transpose. As a function of the α index, $v_{\alpha}^{(k)}$ represents how strongly individual p_{α} contribute to the kth KL mode whereas $w_{\alpha}^{(k)}$ represents how the kth KL mode is distributed onto the original modes. They can have very different shapes in α. We always use the forward KL transform and $v_{\alpha}^{(k)}$ in the following discussion to avoid confusion.

We find two strongly degraded modes with

$$\begin{aligned} \lambda^{(1)} &= 1.86, \\ \lambda^{(2)} &= 1.39. \end{aligned} \tag{3.18}$$

These modes would be better constrained if there were no $XY, \phi\phi$ covariances, which agrees with the intuitive expectation that neglecting mutual covariances would lead to double counting of the lensing information. The corresponding eigenvectors $v_{\alpha}^{(1,2)}$ are plotted in Figure 3.8. All other modes are only mildly affected and have eigenvalues between 0.93 and 1.08. This is consistent with our previous findings that the XY power spectra measure two lensing modes with precision comparable to the sample variance of the lenses (see Fig. 3.4).

We see that measurements of the amplitude of the first mode $\Psi^{(1)}$ are degraded by almost a factor of two. This means that constraint on this mode obtained from the XY lensed power spectra alone are comparable to a constraint from the reconstructed lensing potential

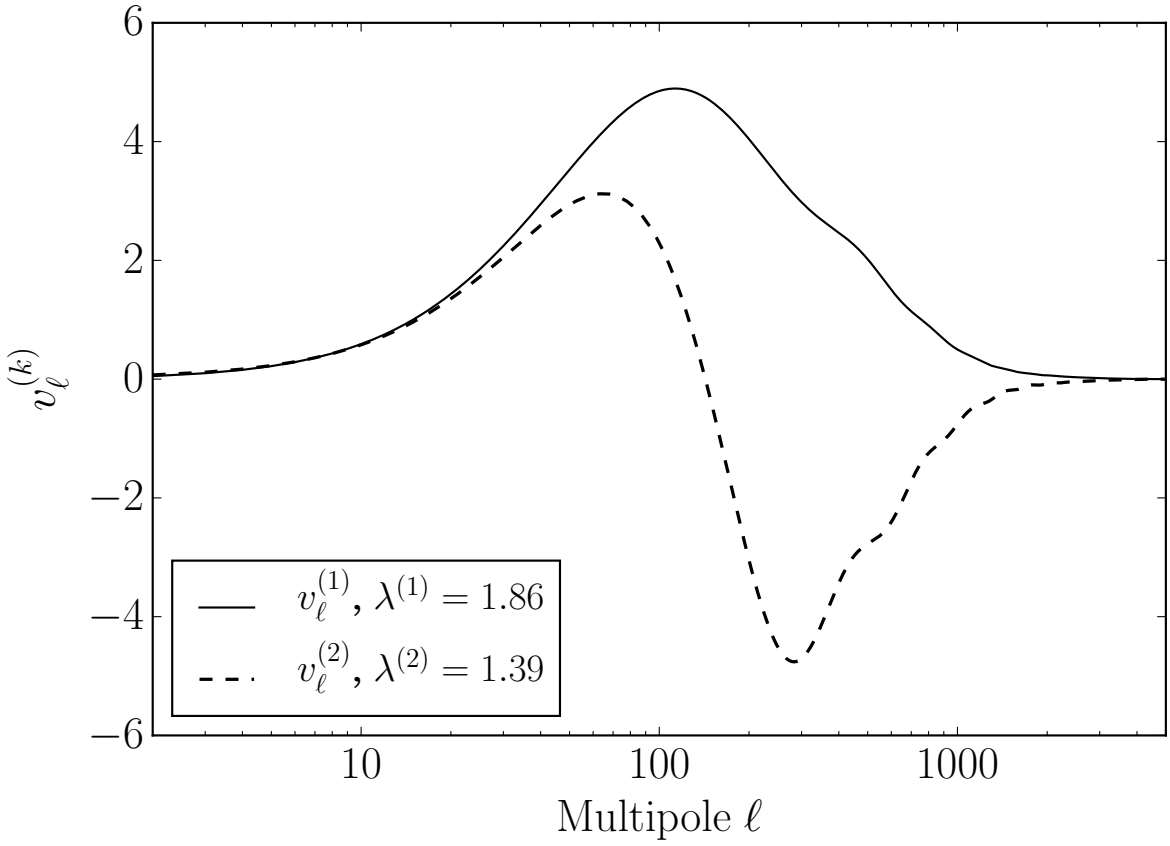

Figure 3.8: KL components of the lensing potential most affected by the covariances $\mathrm{Cov}^{XY,\phi\phi}$ of CMB fields with the reconstructed lensing potential. By neglecting these covariances, constraints on the corresponding amplitude $\Psi^{(k)}$ would be overly optimistic due to double counting of lensing information.

alone but that these two different measurements are highly correlated. As we already argue above, this occurs because both these measurements have their variances dominated by the sample variance of the lenses. This sample variance is common to both measurements, which explains why the two variances are comparable and strongly correlated.

Table 3.1 summarizes how well we can constrain $\Psi^{(1)}$ under various assumptions and provides quantitative justification of these claims. The first two lines summarize the KL results – neglecting $\mathrm{Cov}^{XY,\phi\phi}$ leads to a double counting of the lensing information and overly tight constraints in the full dataset. Instead, we can constrain this mode separately from $\phi\phi$ and XY data with variances that are both comparable to those of the full dataset. The XY result is not a trivial consequence of the KL results since the KL modes are not specifically constructed to be statistically orthogonal with XY measurements alone. Because the XY power spectra provide only integrated constraints on $C_L^{\phi\phi}$, we again impose a mild theoretical prior of $\sigma_{p_\alpha} = 1$ to forbid numerical problems and degeneracies induced by unphysically large features in $C_L^{\phi\phi}$. The minimum variance unbiased linear estimators of $\Psi^{(1)}$ from the separate $\phi\phi$ and XY datasets have a correlation coefficient of 0.77, in agreement with values in Table 3.1.

Note that even when considering XY separately, we include all of the internal covariances induced by lens sample variance. Without the non-Gaussian covariances $\mathcal{N}$, $\sigma^2_{\Psi^{(1)}}$ decreases significantly and is unphysically smaller than the lens sample variance limit by more than a factor of 3. Finally we show that removing all of the non-Gaussian covariances in the full dataset leads to an even more extreme violation of the lens sample variance limit.

Because $\Psi^{(1)}$ is constrained by two independent but strongly correlated measurements, these measurements in principle provide an excellent systematic check on the experimental data that is nearly immune to sample variance and cosmological parameter uncertainties. This check could be very valuable in future experiments, which are likely to be foreground and systematics limited: comparing $\Psi^{(1)}$ measured from power spectra and reconstruction separately could serve as a simple check on data quality and reconstruction algorithms before

Table 3.1: Variance of KL consistency mode $\Psi^{(1)}$ obtained from various combinations of lensed CMB spectra XY and lens power spectra $\phi\phi$ measurements and assumptions about their variances and covariance.

Dataset	Covariance	$\sigma^2_{\Psi^{(1)}}$
$XY, \phi\phi$	$\mathrm{Cov}^{XY,\phi\phi}_{\ell\ell'} = 0$	1.00
$XY, \phi\phi$	Full	1.86
$\phi\phi$	Full	1.96
XY[a]	Full	2.26
$\phi\phi$	Sample variance	1.74
XY[a]	Gaussian	0.52
$XY, \phi\phi$	Gaussian	0.29

[a] With a mild theoretical prior $\sigma_{p_\alpha} = 1$.

performing the delensing operation. Identical conclusions are to a lesser degree valid also for $\Psi^{(2)}$, which could also serve as a weaker consistency check, but valuable in its own right for reasons we discuss below.

Next we test the robustness of these results to our assumptions. The eigenvectors $v^{(k)}$ and corresponding eigenvalues do not change appreciably if we discard in temperature and polarization information for $\ell < 30$, discard reconstruction information for $\ell > 3000$, or include polarization information out to $\ell < 5000$. Unlike cosmological parameter inferences that involve breaking parameter degeneracies involving the standard ΛCDM parameters, $A_s, \tau, \Omega_c h^2$, this consistency test involves just the lensing information. In principle, the development of more sophisticated lens reconstruction algorithms beyond the damping tail may in the future allow additional consistency tests with XY power spectra at $\ell > 3000$. However, this information does not significantly impact the $\Psi^{(1)}$ consistency test since it involves lens power on comparably high ℓ scales. The impact of neglecting $C_\ell^{T\phi}, C_\ell^{E\phi}$ should also not be significant, because unlike $v^{(1,2)}$ they are only significant at the lowest multipoles.

The most important assumption in this construction is that we can independently consider the information about the unlensed CMB and the lens power spectra. While this is a good assumption in the extended ΛCDM parameter space for the full data set including both

XY power spectra and the lensing reconstruction, it is less true when considering the lensed CMB XY spectra alone if spatial curvature is allowed to vary. Increasing Ω_K impacts the unlensed CMB through $\tilde{\Omega}_K$ in a manner similar to the smoothing of the acoustic peaks by lensing [43]. Moreover, its impact on lensing through $p_\alpha(\Omega_K)$ is to decrease the amplitude of power (see Fig. 3.6), and so the overall sensitivity to curvature is degraded. Furthermore, the total impact of curvature on the lensed power spectrum becomes nearly degenerate with effects of the neutrino mass [43]. On the other hand, BB partially breaks the degeneracy as it is not generated by curvature.

To investigate how severe these degeneracies are in the XY dataset, we compare forecasted errors on $\Psi^{(1,2)}$ with fixed vs. marginalized $\tilde{\theta}_A$ (assuming ΛCDM+$\sum m_\nu + w + \Omega_K$) in Table 3.2. As before, we assume a mild theoretical prior $\sigma_{p_\alpha} = 1$.

When $\tilde{\Omega}_K$ is held fixed, the variances of both $\Psi^{(1)}$ and $\Psi^{(2)}$ are negligibly increased by marginalizing the remaining 8 extended ΛCDM parameters. When $\tilde{\Omega}_K$ is also marginalized the variance of $\Psi^{(1)}$ changes only by $\sim 10\%$ but that of $\Psi^{(2)}$ is close to doubled. This mirrors the fact that changing $\Psi^{(1)}$ changes BB significantly more – relative to the rest of the observables – than $\Psi^{(2)}$ does and cannot be mimicked by curvature in the unlensed spectra. We conclude that $\Psi^{(1)}$ provides a robust consistency test for lensing in the full ΛCDM+w+Ω_K+$\sum m_\nu$ context whereas inconsistencies in $\Psi^{(2)}$ between XY and $\phi\phi$ measurements may indicate a finite spatial curvature. Violations of consistency in $\Psi^{(1)}$ would indicate systematics and foregrounds in the measurement or new physics at recombination that mimics the effect of lensing. Either of these possibilities would lead to incorrect cosmological inferences and complicate delensing of the CMB if not discovered beforehand.

Measurements of the gravitational lensing potential from XY leads to many unconstrained but unphysical modes, which prevents us from constructing the consistency modes $\Psi^{(i)}$ directly from their definition (3.14) when doing an actual analysis. However, we can faithfully construct the consistency mode $\Psi^{(1)}$ using the 5 lowest order PC components introduced in Section 3.2, with the dominant contributions from the first two. The corresponding

Table 3.2: Variance of KL consistency modes $\Psi^{(1,2)}$ obtained from XY lensed CMB power spectra alone with and without unlensed CMB parameters $\tilde{\theta}_A$ marginalized; assuming ΛCDM+$\sum m_\nu + w + \Omega_K$. (With mild theoretical prior $\sigma_{p_\alpha} = 1$.)

	$\sigma^2_{\Psi^{(1)}}$	$\sigma^2_{\Psi^{(2)}}$
all $\tilde{\theta}_A$ fixed	2.26	4.13
8 marginalized, $\tilde{\Omega}_K$ fixed	2.27	4.35
all $\tilde{\theta}_A$ marginalized	2.52	7.34

expansion reads

$$\Psi^{(1)} = \sum_{i=1}^{5} \mathcal{T}_i \Theta^{(i)} \tag{3.19}$$

with $\mathcal{T}_i = \{32.3, -15.9, 0.330, 1.72, -0.608\}$. We have explicitly checked that truncating the remaining components has no significant effect on the results of the Fisher error analysis, for example those displayed in Table 3.2. Because of the truncation, the $\sigma_{p_\alpha} = 1$ prior plays little role and may be omitted. This construction therefore provides a practical means of measuring $\Psi^{(1)}$ from the XY data.

Notice also that this direction is mainly composed of $\Theta^{(1)}$ and $\Theta^{(2)}$ in nearly the same combination that is maximally affected by non-Gaussian lens sample variance (Fig. 3.5). While being limited by the lens sample variance is detrimental to cosmological parameter constraints, for consistency tests this is advantageous because lens sample variance drops out when comparing measurements on the same patch of sky.

On MCMC simulations of lensed CMB we can check that this truncation can work in a more realistic setting. In Fig. 3.9, we compare posterior mean values of $\Psi^{(1)}$ as calculated from (3.19) determined from 50 simulated power spectra using MCMC against values of $\Psi^{(1)}$ determined directly from a known realization of the lensing potential, which can be thought of as a limiting case of lensing potential measurement with no instrumental noise. The latter

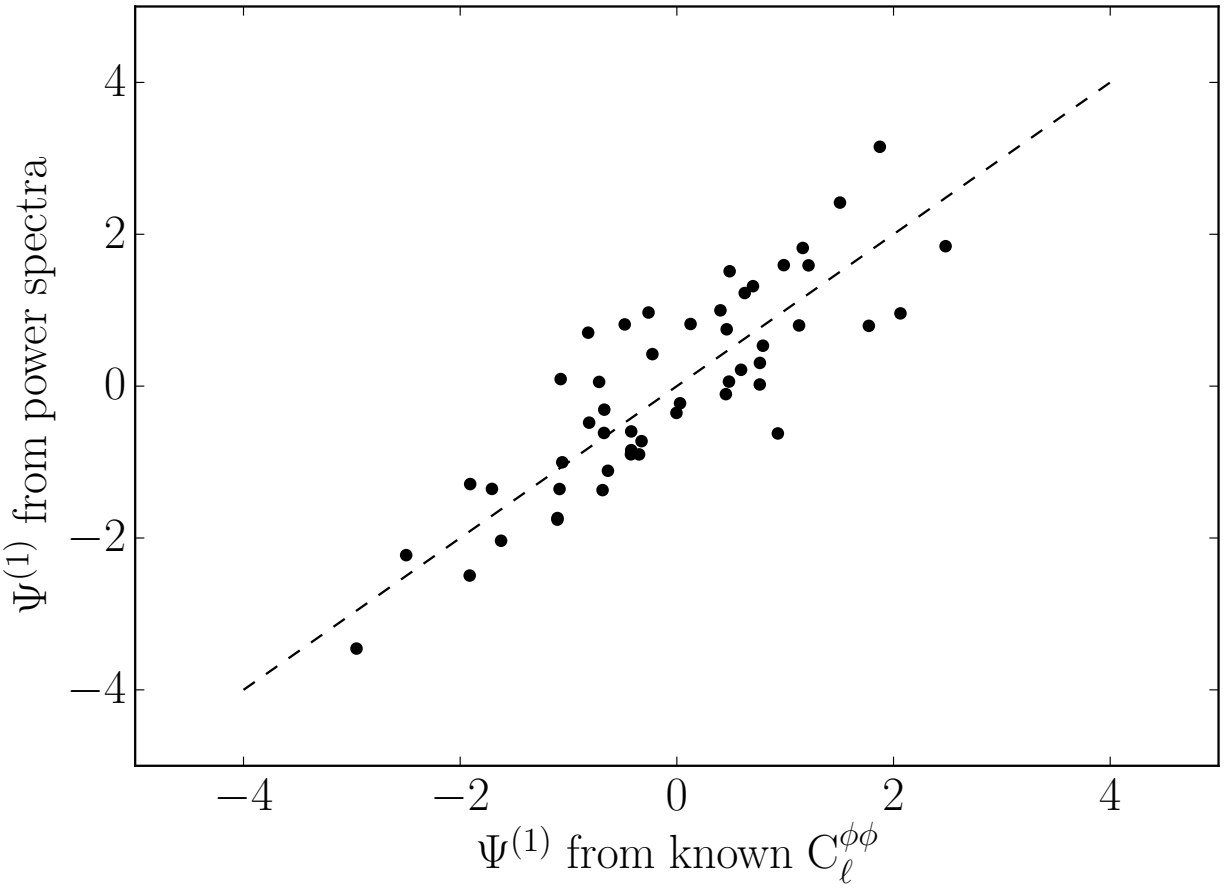

Figure 3.9: Consistency mode $\Psi^{(1)}$ as determined from posterior mean values in 50 simulated lensed power spectra through MCMC analysis against values determined from known realizations of the lensing potential (see text for details). The dashed line represents points where the two determinations are equal.

approach estimates $\Theta^{(i)}$ from simulated $C_L^{\phi\phi}$ using an unbiased estimator

$$\Theta_{\rm est}^{(i)} = \sum_L K_L^{(i)} \left(\ln C_L^{\phi\phi} - \langle \ln C_L^{\phi\phi} \rangle \right), \tag{3.20}$$

where $\langle \cdot \rangle$ is expectation value over realizations, and combines the results according to (3.19). We leave comparison with $\Theta^{(i)}$ obtained from actual lensing reconstruction of the simulated data for a future work. The observed correlation is indeed very tight; residual scatter in Fig. 3.9 is caused by instrumental noise and variance of the unlensed CMB which affect the power spectrum measurement.

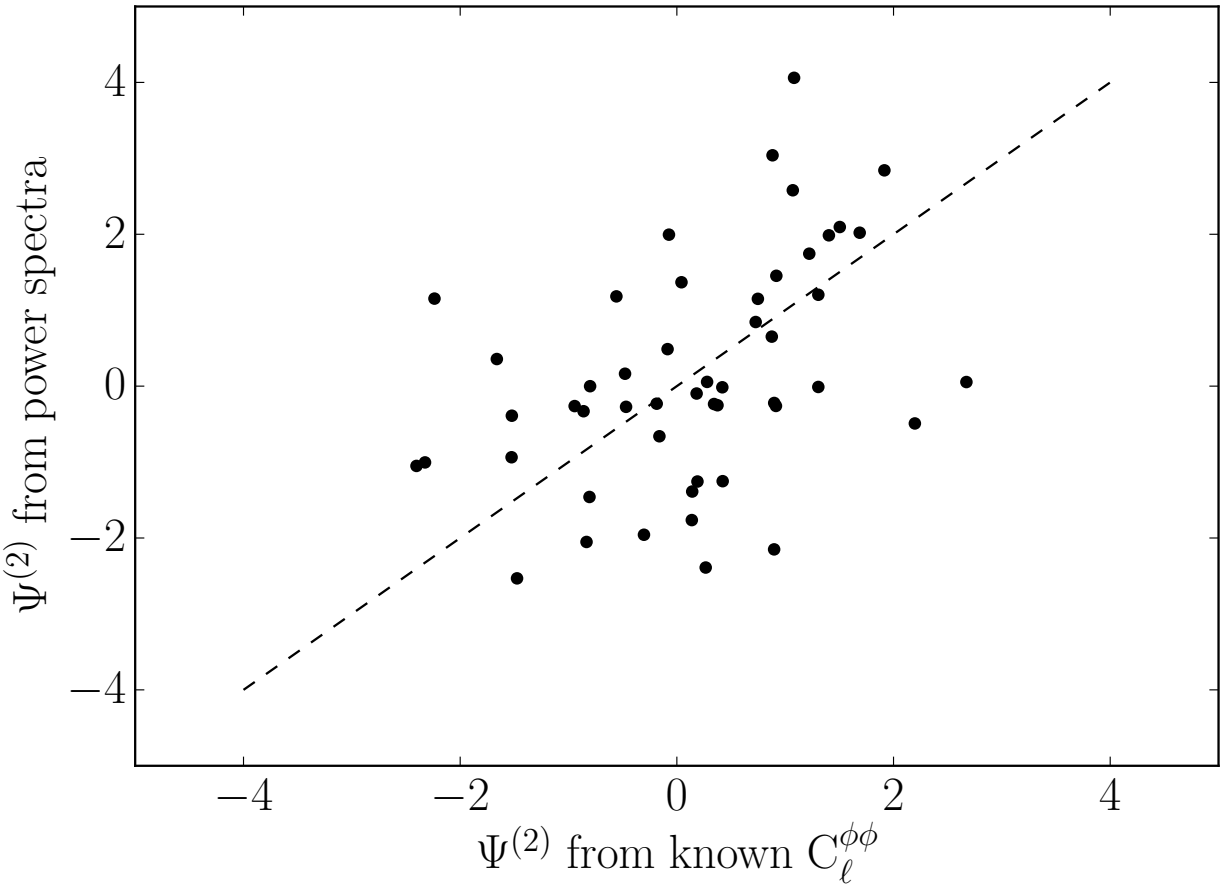

Figure 3.10: Same as Fig. 3.9 but for the consistency mode $\Psi^{(2)}$.

The second combination of $C_L^{\phi\phi}$ that can serve as a similar consistency check $\Psi^{(2)}$ can be expanded in the lens PCs as

$$\Psi^{(2)} = \sum_{i=1}^{5} \mathcal{U}_i \Theta^{(i)} \tag{3.21}$$

with $\mathcal{U}_i = \{31.3, 17.6, 10.4, 0.945, -1.10\}$. As argued above, this consistency check is slightly weaker than the test using $\Psi^{(1)}$ due to the larger impact of noise and sample variance of the unlensed CMB. This weakening can be seen in Fig. 3.10, where we compare values of $\Psi^{(2)}$ determined from 50 simulated power spectra against values from known realization of the lensing potential.

Notice also that there is no indication of bias in the power spectrum estimate of the two consistency modes in Figs. 3.9, 3.10. To better quantify this, in Figure 3.11 we show product

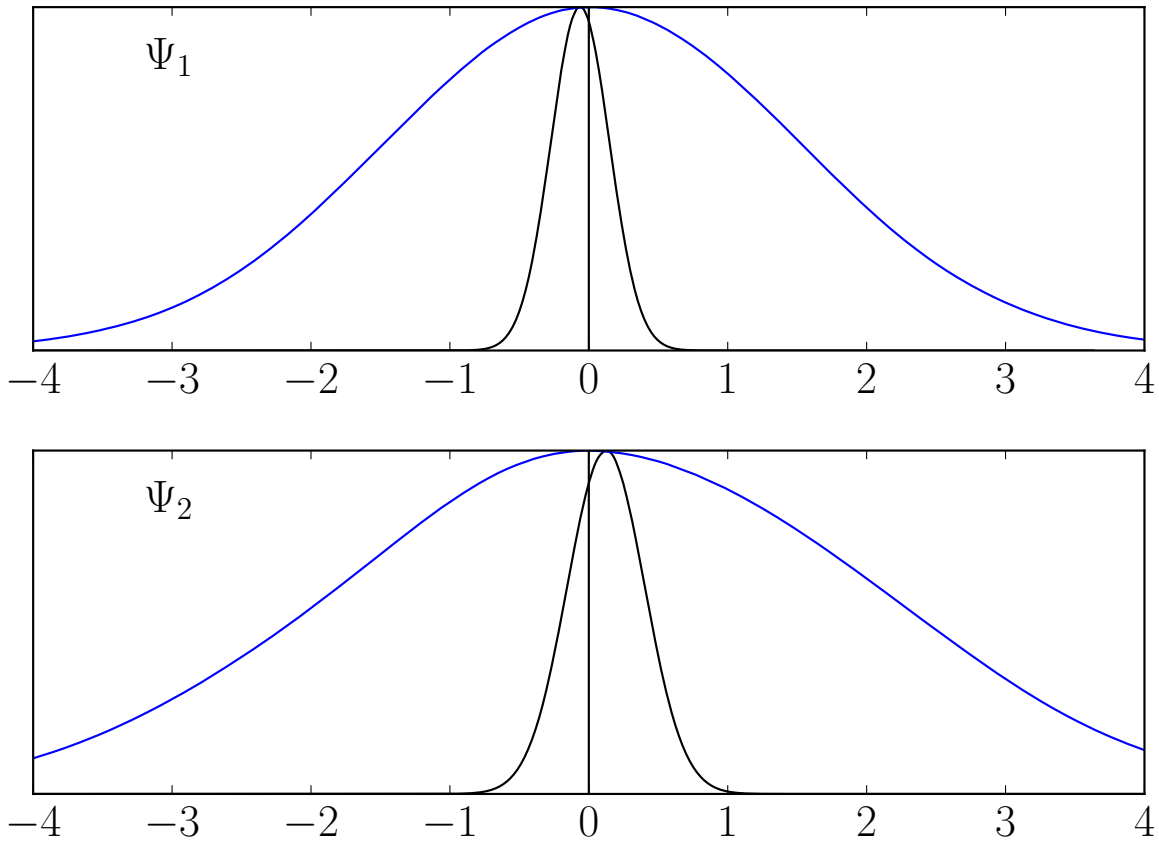

Figure 3.11: Joint posterior of the consistency parameters $\Psi^{(1)}$ and $\Psi^{(2)}$ (black) as the product of 50 individual posterior distributions from independent all-sky simulations. Compared against the width of a single posterior (blue) there is no indication of bias with respect to the fiducial value $\Psi^{(i)} = 0$ at a fraction of the standard deviation.

of 50 posteriors for measurements of $\Psi^{(1)}, \Psi^{(2)}$ as determined from our MCMC simulations and the determination is indeed unbiased; from the power spectra side there does not seem to be any problem for the consistency check.

We also find that $\Psi^{(1)}$ is almost uncorrelated with the ΛCDM parameters describing the unlensed power spectra; the largest correlation coefficient we find is $R = -0.03$ and occurs between $\Psi^{(1)}$ and $\widetilde{\Omega_b h^2}$. The other consistency mode is slightly more correlated with the unlensed parameters; the most correlated with $\Psi^{(2)}$ are $\tilde{\theta}_*$ with correlation coefficient $R = 0.12$ and $\widetilde{\Omega_b h^2}$ with $R = 0.08$.

Failure of the consistency check could indicate an unlensed spectrum that is not described

by the flat ΛCDM parameters. Above it was shown that the second consistency mode $\Psi^{(2)}$ is correlated with the spatial curvature given their similar effects on the acoustic peaks. We run a single MCMC analysis in which we added $\tilde{\Omega}_K$ to the unlensed parameters and confirm this finding; there is a strong correlation between $\tilde{\Omega}_K$ and $\Psi^{(2)}$ with correlation coefficient $R = -0.62$. In a non-flat Universe analyzed as flat this would lead to failure in the consistency check as $\Psi^{(2)}$ would move from its true value to absorb the unaccounted for curvature. The main consistency mode, $\Psi^{(1)}$, is correlated with $\tilde{\Omega}_K$ at the $R = 0.29$ level and is a weaker check on curvature.

3.6 Discussion

In this chapter we introduce a technique in which the information from the unlensed CMB power spectra and from the lensing potential $C_L^{\phi\phi}$ are considered independently, allowing us to directly measure the gravitational lensing potential from the data. We explain how to use principal component analysis to encode the lensing information using a small number of lens principal components $\Theta^{(i)}$.

On 50 simulated CMB data sets we test our MCMC-based analysis pipeline, not finding any significant bias in either $\Theta^{(i)}$ or the unlensed parameters $\tilde{\theta}_A$. The lensing principal components $\Theta^{(i)}$ are found to be only weakly correlated, both mutually and with the unlensed counterparts $\tilde{\theta}_A$ of the ΛCDM parameters. The major effect of the non-Gaussian covariance is degradation of constraints on the two leading lensing principal components, $\Theta^{(1)}$ and $\Theta^{(2)}$ (see Fig. 3.4). This explains the parameter constraint degradations seen in the previous chapter - in each investigated cosmological model there is a parameter combination which is predominantly limited by the low ℓ lensing information, or in other words which has large lens sample variance relative to other sources of noise. Neglecting non-Gaussian terms in the data covariance effectively neglects this source of noise, which misleads the parameter constraints.

Constraints on $\Theta^{(i)}, \tilde{\theta}_A$ can also be used for model building purposes given their simple

multivariate normal form. As illustrated using the dark energy equation of state, one can rapidly explore lensing constraints on extensions to ΛCDM using an effective likelihood for these parameters without recourse to the original CMB power spectrum data or experimental specifics.

The possibility to directly measure the gravitational lensing potential from the data allows various consistency checks, either internal to a given data set or by comparing various data sets. We check that the combinations of $\Theta^{(i)}$ which form the most stringent consistency tests between lensing reconstruction and power spectra data, $\Psi^{(1)}$ and $\Psi^{(2)}$, satisfy theoretical expectations. Most importantly, their values determined from lensed power spectra using MCMC analyses are strongly correlated with the values determined from the known realization of $C_L^{\phi\phi}$. They are also unbiased and their effect on the lensed power spectra is nearly uncorrelated with the effects of the unlensed parameters $\tilde{\theta}_A$ from the ΛCDM family. Failure of any of these consistency tests may indicate new physics beyond flat ΛCDM, as we show on an example of spatial curvature.

CHAPTER 4

PLANCK LENSING TENSIONS

In this chapter we apply techniques to check lensing consistency introduced in the previous chapter to the Planck satellite data. We start by listing the data sets used and explaining small differences of the present analysis from those of the previous two chapters. After that we describe the various lensing constraints and we end by evaluating significance of the tensions found in the data. As Planck satellite is not able to measure the gravitational lensing potential with precision close to the lens sample variance, we can safely neglect the effects of the non-Gaussian covariances discussed in Chapter 2.

4.1 Analysis details

In this section we summarize the data used in this chapter and present the fiducial cosmology and principal components $\Theta^{(i)}$ used in the analyses that follow.

4.1.1 Data sets and MCMC

For the analyses in this chapter we use the publicly released Planck 2015 likelihoods[1] for the power spectra of the CMB temperature, polarization and of the gravitational lensing potential reconstructed from their maps as summarized in Table 4.1. Joint use of multiple likelihoods will be denoted by a plus sign connecting them. For the analyses using only the lensing reconstruction likelihood `PP`, correction for the $N^{(0)}, N^{(1)}$ biases is performed using the best fit power spectra to `TT+lowTEB` likelihoods assuming the six parameter ΛCDM model. The likelihood `liteTT`, which we use for the lens principal component construction and checking robustness of the results below, is a high-ℓ temperature likelihood, with the foreground parameters pre-marginalized over. Otherwise, we marginalize over the standard foreground parameters with their default priors, where applicable.

1. https://www.cosmos.esa.int/web/planck/pla

Table 4.1: Planck likelihoods used in this work

Label	Power spectra	ℓ-range	Name
`TT`	TT	$\ell \geq 30$	`plik_dx11dr2_HM_v18_TT`
`TTTEEE`	TT,TE,EE	$\ell \geq 30$	`plik_dx11dr2_HM_v18_TTTEEE`
`lowT`	TT	$\ell < 30$	`commander_rc2_v1.1_l2_29_B`
`lowTEB`	TT,TE,EE,BB	$\ell < 30$	`lowl_SMW_70_dx11d_2014_10_03_v5c_Ap`
`PP`	$\phi\phi$	$40 \leq \ell \leq 400$	`smica_g30_ftl_full_pp`
`liteTT`	TT	$\ell \geq 30$	`plik_lite_v18_TT`

For the analyses themselves we again use the MCMC code CosmoMC to sample the posterior probabilities in the space of cosmological parameters. Each of our chains has a sufficient number of samples such that the Gelman-Rubin statistic $R - 1$ [42] falls below 0.01.

4.1.2 Fiducial cosmology

In this chapter we use a different fiducial cosmology with respect to which we define $\Theta^{(i)}$, to be closer to the cosmology preferred by the Planck data. The fiducial cosmological model is taken from the best fit flat ΛCDM cosmological model, determined from `TT+lowTEB` likelihoods assuming no primordial tensor modes and minimal mass neutrinos ($\sum m_\nu = 60\,\mathrm{meV}$). To reflect the latest results on the optical depth to recombination τ [44], we set τ to the value from that work and decrease A_s to keep $A_s e^{-2\tau}$ constant. A lower A_s tends to exacerbate the preference for anomalously high lensing in the temperature power spectrum within the ΛCDM context but here serves only as the baseline fiducial model against which to define $\Theta^{(i)}$. Values of the corresponding cosmological parameters are listed in Table 4.2.

4.1.3 Principal components

To determine significance of the Planck lensing tensions, we use the technique to directly measure $C_L^{\phi\phi}$ that was introduced in the previous chapter. As before, we parameterize the

Table 4.2: ΛCDM parameters and their fiducial values for the lens PC construction. (In ΛCDM, these parameters also imply a Hubble constant of $h = 0.6733$.)

Parameter	Fiducial value
$100\ \theta_*$	1.041
$\Omega_c h^2$	0.1197
$\Omega_b h^2$	0.02223
n_s	0.9658
$\ln(10^{10} A_s)$	3.049
τ	0.058

gravitational lensing potential in terms of a small number of effective parameters $\Theta^{(i)}$ as

$$C_L^{\phi\phi} = C_{L,\mathrm{fid}}^{\phi\phi} \exp\left(\sum_{i=1}^{N} K_L^{(i)}\, \Theta^{(i)}\right), \tag{4.1}$$

while parameterizing the unlensed CMB power spectra using the six parameters $\tilde{\theta}_A$ that do not affect the lensing potential and determine the unlensed CMB in the same way as in ΛCDM.

Because the Planck satellite measurements have instrumental noise levels above those of the proposed CMB-S4 experiment, we in this chapter choose a different set of principal components than the one used in the previous chapter. We now choose $K_L^{(i)}$ such that $\Theta^{(i)}$ correspond to the N principal components of the gravitational lensing potential best measured by the Planck lensed TT power spectrum. We determine them from the data covariance matrix provided with the Planck likelihood `liteTT` using a Fisher matrix construction; the resultant eigenmodes $K_L^{(i)}$ are shown in Fig. 4.1. The lowest variance mode peaks around $L = 100$ and is much better constrained than the second best constrained component; the Fisher matrix forecast predicts a factor of ~ 50 in the ratio of variances. This is largely because Planck data do not strongly constrain the BB power spectrum [43] or temperature multipoles above $\ell \approx 2000$, which are sensitive to smaller scale lenses. Because $K_L^{(i)}$ are smooth functions of L, we again discretize $C_L^{\phi\phi}$ into bins of width $\Delta L = 5$. Unless otherwise specified, we retain $N = 4$ PCs in order to fully characterize all sources of lensing

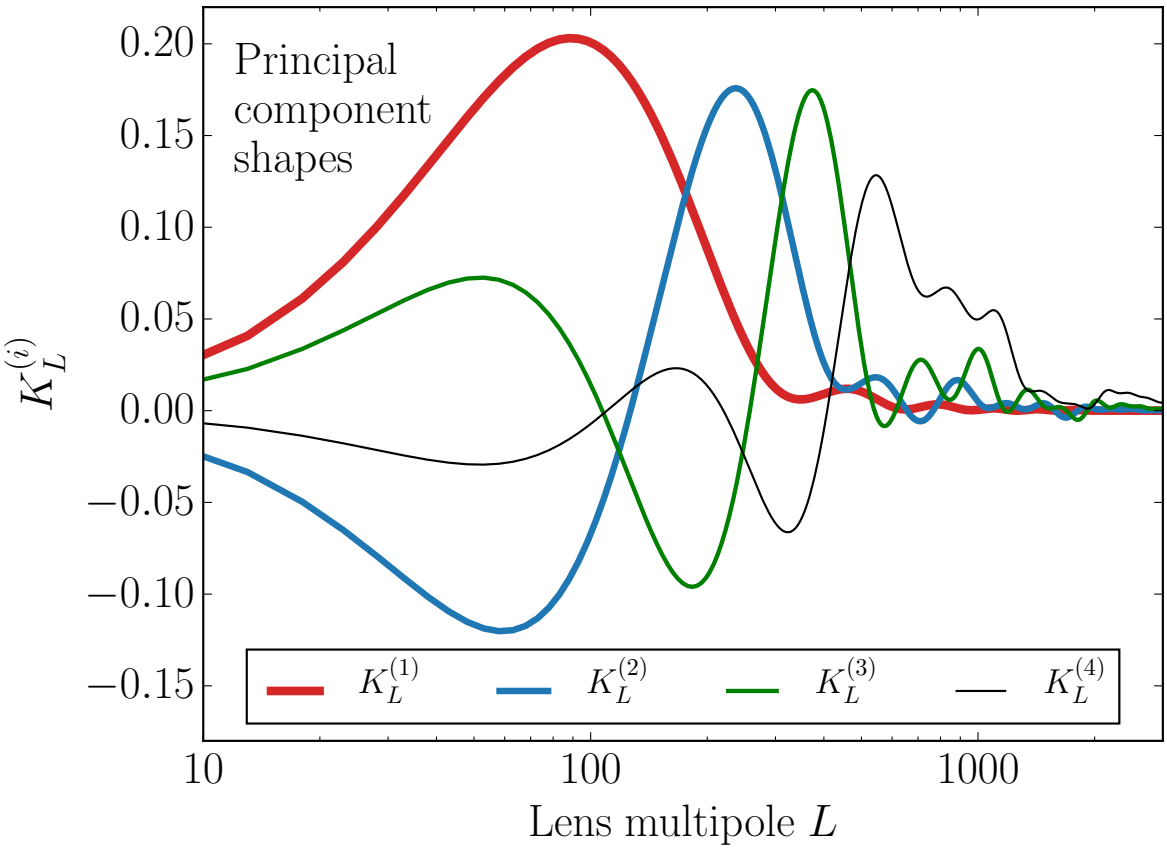

Figure 4.1: Functions $K_L^{(i)}$ corresponding to the four principal components of the lens potential best measured by the Planck lensed TT power spectrum, determined from the `liteTT` likelihood.

information (see Section 4.2.1).

4.2 Model-independent lensing constraints

Measuring the lens principal components from the Planck temperature, polarization and lensing reconstruction power spectra provides a new means of extracting and comparing the various sources of lens information in the CMB. This comparison, introduced in Chapter 3, presents a direct and model-independent consistency test of the lensing information and in the ΛCDM model context enables an internal consistency check of the ΛCDM parameters inferred from CMB power spectra information from recombination and from lens information.

This is particularly relevant given the known preference for excess lensing in the Planck temperature data [51, 52].

We start by characterizing the information in the lensing reconstruction data, which also determines the number of lens principal components required for our comparative analysis. We then discuss constraints on $\Theta^{(i)}$ from the temperature and polarization power spectra and focus on the two leading principal components. We also derive $\Theta^{(i)}$ from the recombination or unlensed information in the power spectrum in the ΛCDM model as a check of its internal consistency. We finish by commenting on robustness of our results with respect to various analysis choices.

4.2.1 Reconstruction constraints

The principal component decomposition of the lens power spectrum described in Section 4.1.3 is optimized for the temperature power spectrum analysis but can also be used to analyze the reconstruction data. Even though we will be mainly interested in the first two components for comparisons with the other analyses, it is important to retain a sufficient number of higher components so that their marginalization does not affect the lower ones.

In practice we choose the number of principal components according to whether the data can constrain them better than a weak theoretical prior. We choose flat tophat priors on $\Theta^{(i)}$ within a range where the variation in $C_L^{\phi\phi}$ is within a factor of 1.5 of $C_{L,\rm fid}^{\phi\phi}$. These weak priors are meant to eliminate cases that would be in conflict with other measurements of large scale structure or imply unphysically large amplitude high frequency features in $C_L^{\phi\phi}$.

In Fig. 4.2 we show constraints from the lensing reconstruction likelihood `PP` on the first four $\Theta^{(i)}$ for the cases where we allow four or five lens PCs to vary. For $\Theta^{(3)}$ and $\Theta^{(4)}$ the edges of the box represent the prior and so the 4th component is nearly prior limited. Correspondingly, the addition of $\Theta^{(5)}$ does not significantly affect constraints on $\Theta^{(1)}$ and $\Theta^{(2)}$ which will be important for evaluation of the tensions in the data. We therefore standardize on four lens PCs unless otherwise specified, with higher lens PCs set to zero,

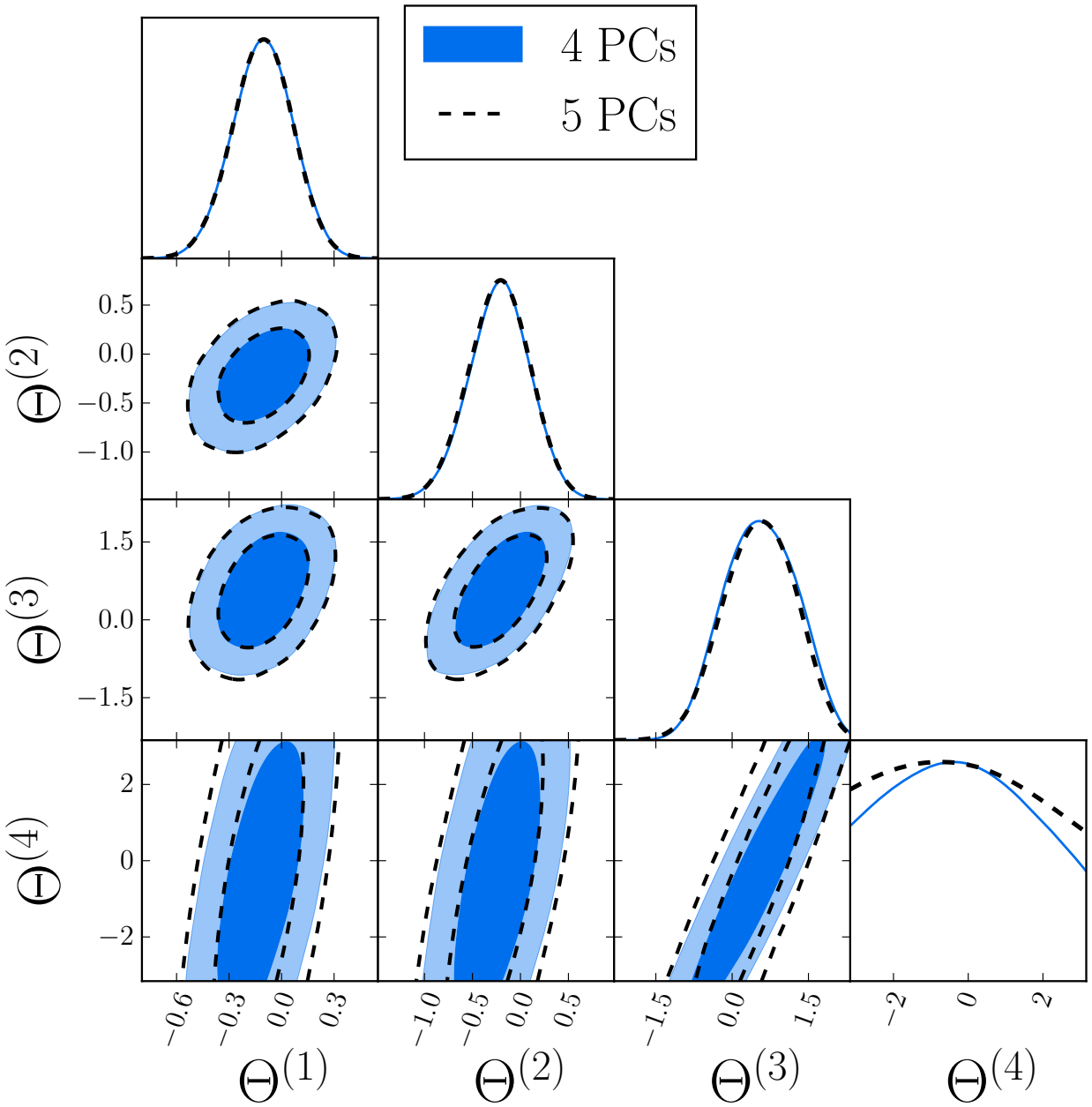

Figure 4.2: Lens reconstruction constraints from PP on lens PCs (68% and 95% CL). The analysis with the fiducial four PCs (blue solid) and with an additional fifth PC marginalized (dashed) give nearly identical results for the first two PCs. Higher PCs are fixed to zero, their fiducial value.

which is their fiducial value.

Another way to visualize why 4 PCs suffices is to construct the lens power spectrum out of them as

$$C_{L,\mathrm{filt}}^{\phi\phi} = C_{L,\mathrm{fid}}^{\phi\phi} \exp\left(\sum_{i=1}^{4} K_L^{(i)}\,\Theta^{(i)}\right). \tag{4.2}$$

and compare it to the lens reconstruction data itself. In Fig. 4.3, we show this comparison. The 4 PC construction represents smooth deviations that are allowed by the data. Fluctuations that are not represented by the functional form of the PCs shown in Fig. 4.1 are not captured by the construction, for example the fluctuation in the data around $L = 330$. Thus the PC construction does not represent direct, but rather filtered, constraints on $C_L^{\phi\phi}$. To compare PC constraints from other sources to the lens reconstruction constraints, it is important to compare their implications for $C_{L,\mathrm{filt}}^{\phi\phi}$ rather than $C_L^{\phi\phi}$ directly. This PC filter has the benefit of producing smooth functional constraints utilizing the full data set at the expense of highly correlating constraints at different multipoles.

4.2.2 Temperature constraints

We analyze the `TT+lowTEB` likelihood for 4 PCs with the weak theoretical priors discussed in the previous section. To focus on the region consistent with lens reconstruction, we impose an additional data-driven prior. As shown in the previous section, lensing reconstruction constrains $\Theta^{(1)}$ and $\Theta^{(2)}$ significantly better than the theoretical prior from the previous section, we thus consider restricting these two variables further. As we will see, $\Theta^{(1)}$ drives the tension between reconstruction and temperature constraints; for this reason we do not strengthen the prior on it. On the other hand, we restrict $\Theta^{(2)}$ to lie within six standard deviations from the mean value from the reconstruction analysis that considers 4 PCs. We retain this prior even for analyses in which $\Theta^{(4)}$ is fixed to its fiducial value. We shall see that the tension between power spectra and lensing reconstruction information on lensing is weaker than 6σ and so this prior does not artificially increase the tension. It therefore just

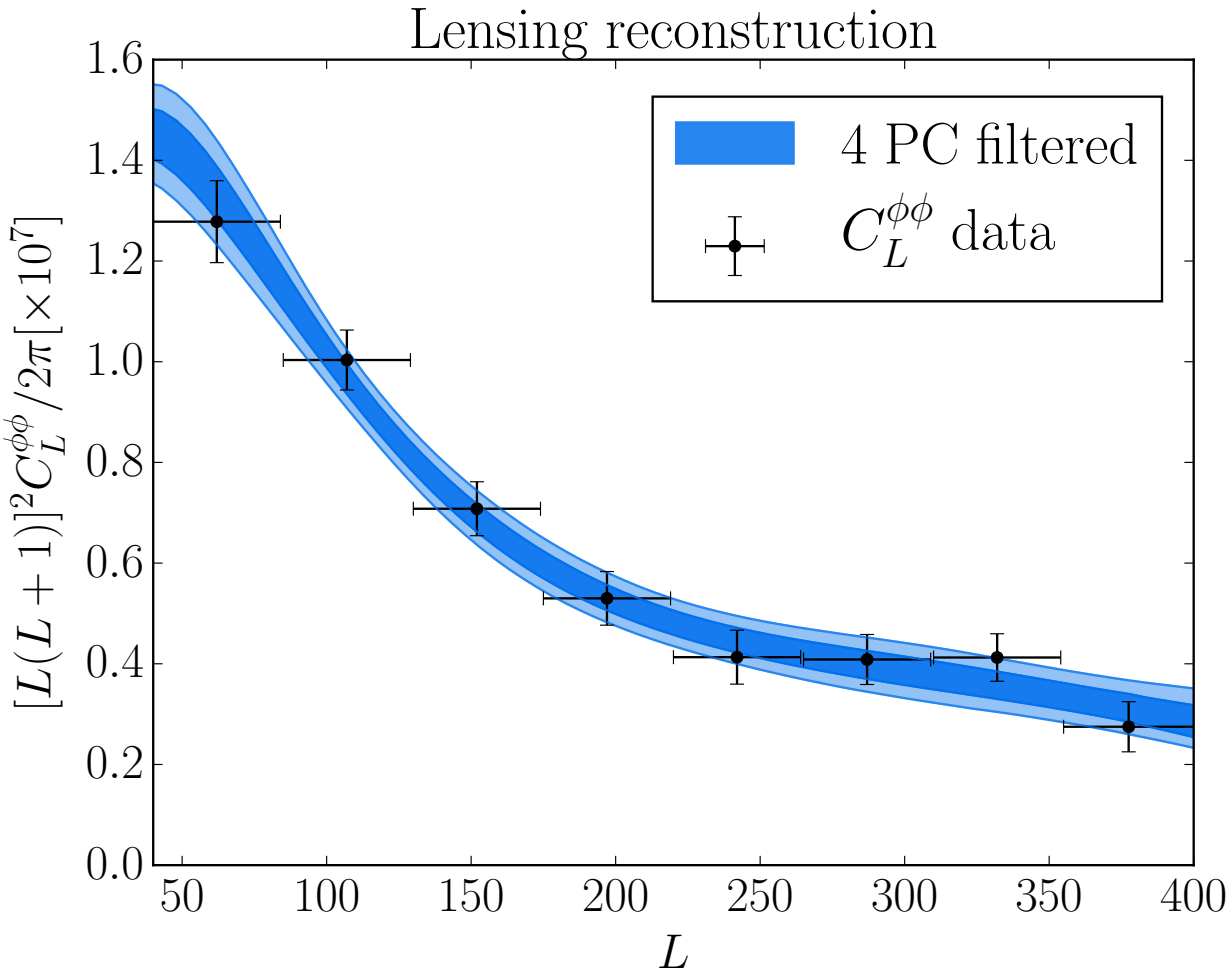

Figure 4.3: Lens reconstruction constraints from PP on the lens power spectrum filtered through the 4 PC analysis $C^{\phi\phi}_{L,\mathrm{filt}}$ (blue, 68% and 95% CL). The points correspond to the measured Planck values included in the PP likelihood. Although the points are only weakly correlated, PC filtering through Eq. (4.2) utilizes all data points for each multipole leading to a smoother but correlated constraint.

excludes the parameter space that would be grossly ruled out by reconstruction data and is used mostly for visualization purposes.

As expected, `TT+lowTEB` data constrain mainly one principal component with $\Theta^{(2)}$ limited by the priors and $\Theta^{(3)}$ and $\Theta^{(4)}$ completely dominated by them. In Fig. 4.4 we show the constraints (red contours) in the $\Theta^{(1)} - \Theta^{(2)}$ plane out to the edge of the $\Theta^{(2)}$ prior. Because the PCs were constructed from a Fisher forecast, the constrained direction is nearly but not perfectly aligned with $\Theta^{(1)}$, leaving a slight correlation between the two parameters. In Fig. 4.5 we show that the degenerate direction for the `TT+lowTEB` analysis corresponds approximately to constant $C^{\phi\phi}_{123}$, whereas contours of constant $\Theta^{(1)}$ correspond approximately to $C^{\phi\phi}_{127}$ as determined by the zero crossing of $K^{(2)}_L$ in Fig. 4.1.

For comparison we in Fig. 4.4 also show the constraints from lens reconstruction (blue contours). The two constraints are in tension with each other in that the two contours only overlap in their 95% CL regions. Moreover, this tension is model independent: no change in the shape of $C^{\phi\phi}_L$ allowed by the 4 PCs can resolve it.

We can also visualize the `TT+lowTEB` constraint on $C^{\phi\phi}_L$ as filtered through the first 4 PCs via Eq. (4.2); for the ease of comparison we show fractional difference from the fiducial model. In Fig. 4.6 we show that posterior constraints from the `TT+lowTEB` data are stronger than the prior mainly around $L \sim 120$ while at high $L \gtrsim 250$ the constraints are prior dominated. Note that the prior is skew positive allowing a tail to high $C^{\phi\phi}_L$ where the probability drops slowly. The large values of $\Theta^{(1)}$ that the data prefer can therefore easily push the 95% CL region of the posterior beyond that of the prior, especially around $L \sim 200$.

In Fig. 4.7 (top panel) we compare these posterior constraints on $C^{\phi\phi}_{L,\mathrm{filt}}$ from the `TT+lowTEB` to those from `PP`. The reconstruction data favors less power around $L \sim 120$. Although changes in the shape of $C^{\phi\phi}_L$ can bring agreement between the two away from this regime, tension remains there independent of the model. We have explicitly checked that increasing the theoretical priors does not aggravate this tension, despite the fact that the upper bounds from the posterior and the prior around $L \sim 120$ coincide in Fig. 4.6.

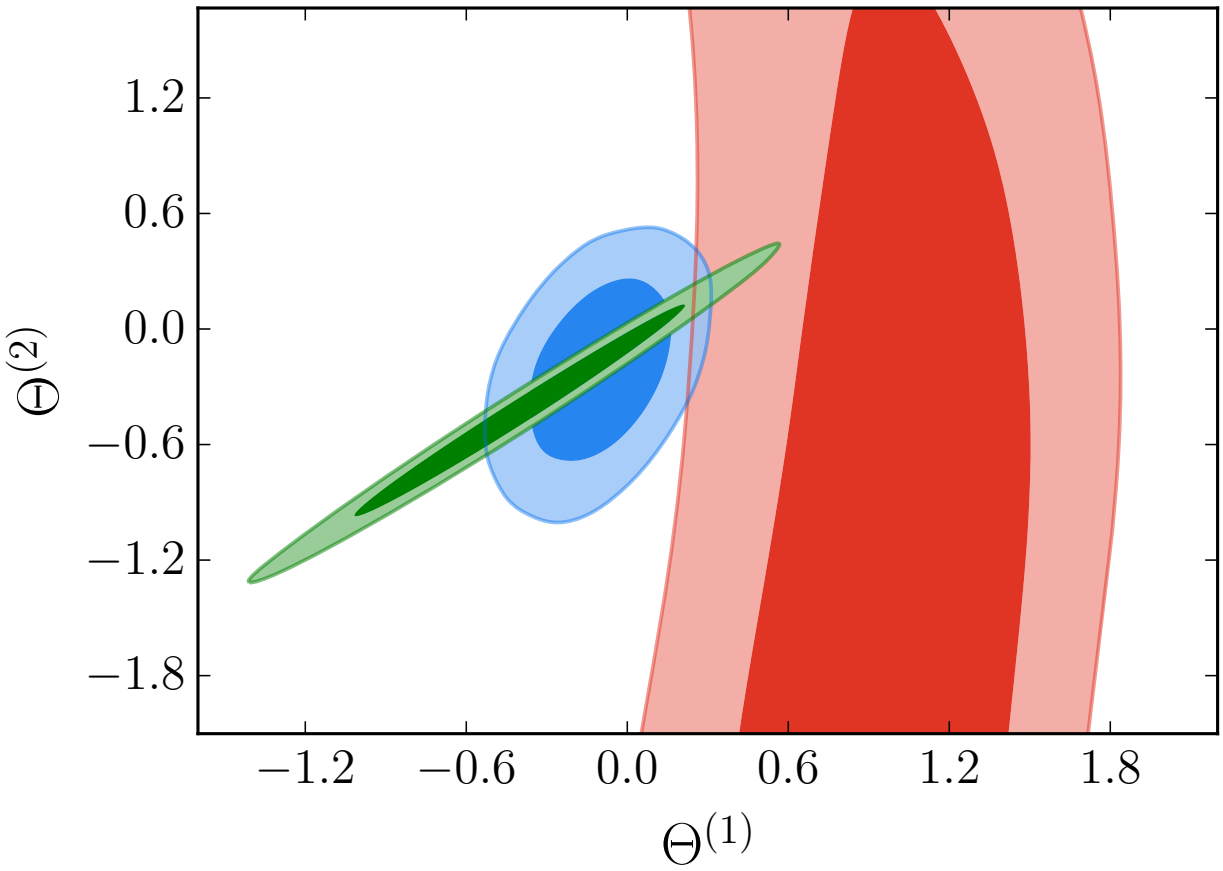

Figure 4.4: CMB power spectrum constraints on lens PCs $\Theta^{(1)}$ and $\Theta^{(2)}$ from `TT+lowTEB` (red, 68% and 95% CL) compared with lens reconstruction `PP` from Fig. 4.2 (blue) and ΛCDM predictions based on unlensed parameters $\tilde{\theta}_A$ from `TT+lowTEB` (green). The fiducial 4 PC analysis is used in all cases.

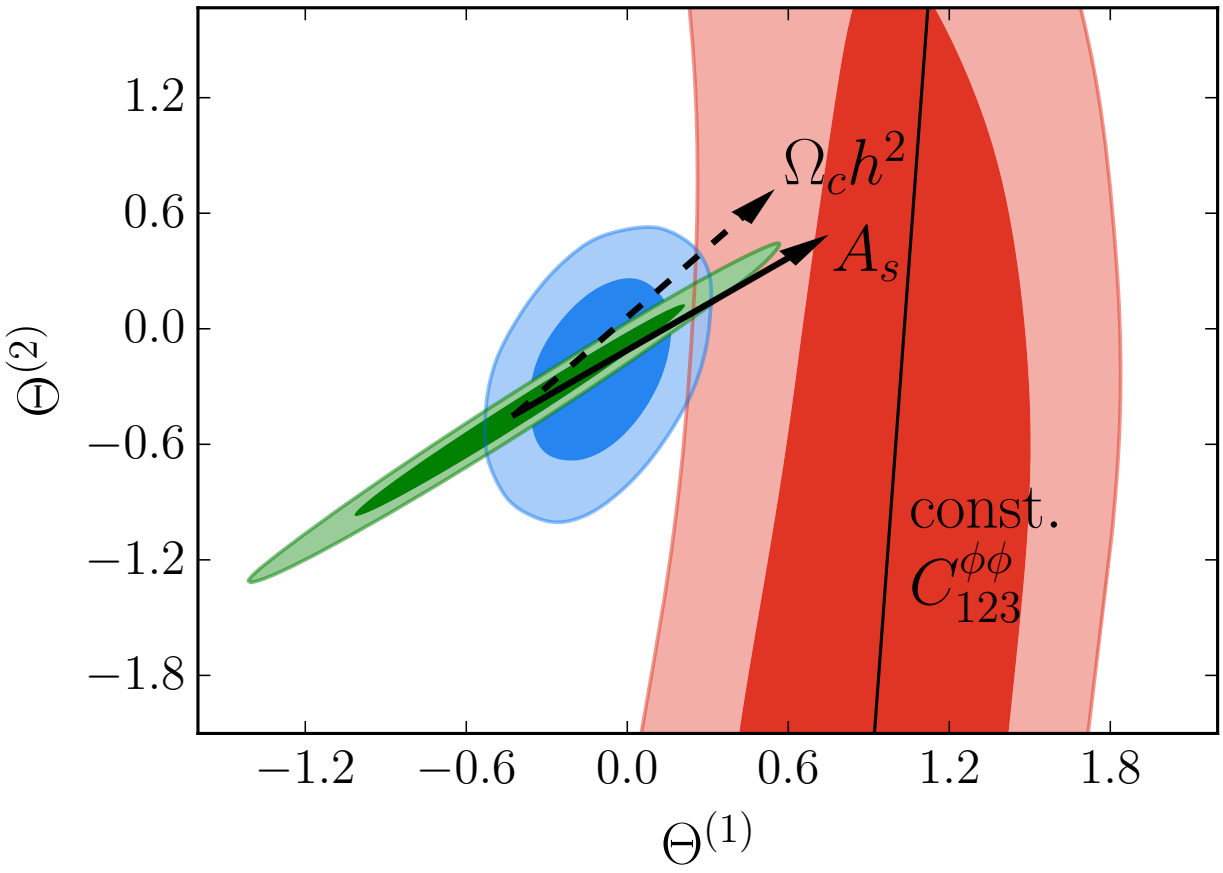

Figure 4.5: Physical interpretation of constrained directions from Fig. 4.4. The line approximates the degeneracy direction of the `TT+lowTEB` (red) contour and correspond to a line of constant $C_{123}^{\phi\phi}$. Arrows shows changes in $C_L^{\phi\phi}$ caused by increasing A_s (solid) and $\Omega_c h^2$ (dashed) in ΛCDM while keeping the other parameters in Tab. 4.2 fixed.

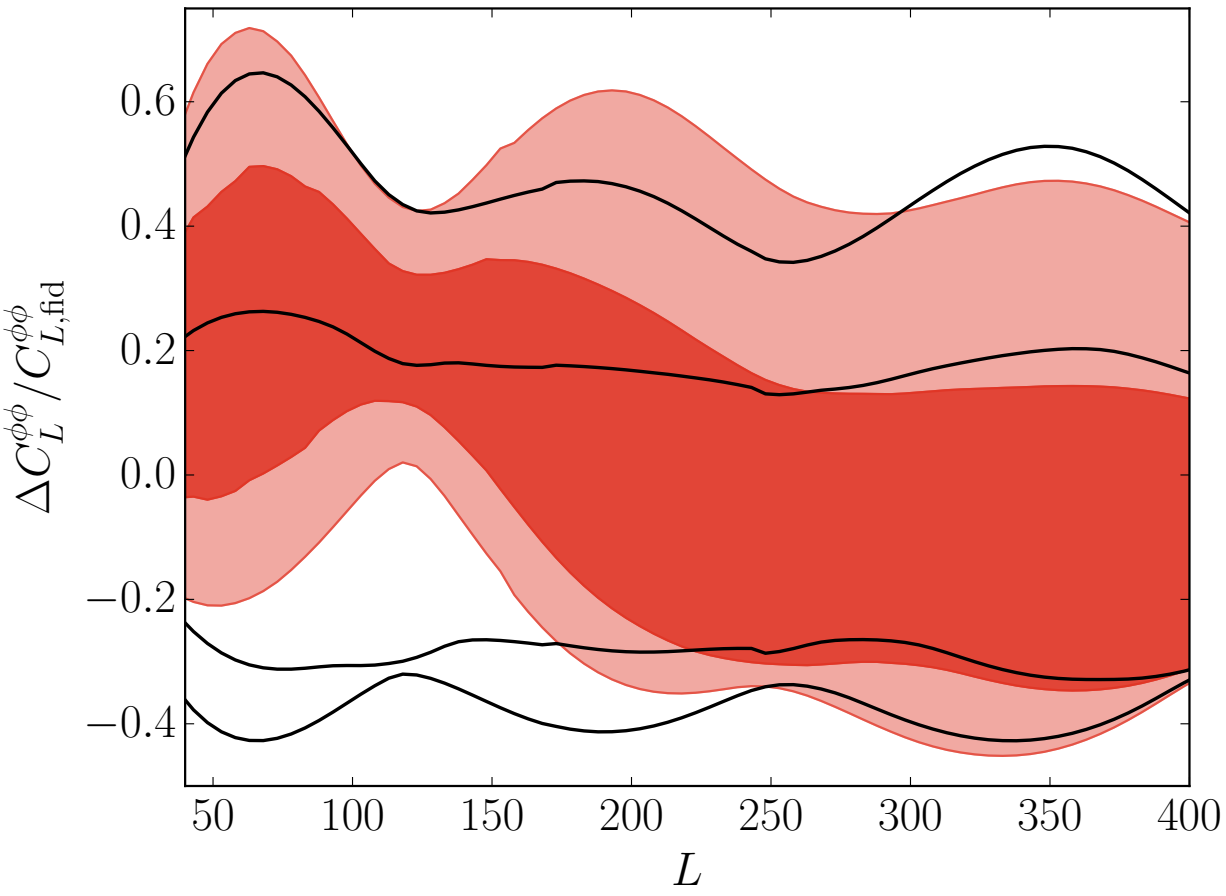

Figure 4.6: CMB power spectrum posterior constraints on fractional deviations in the 4 PC filtered lens power spectrum from the fiducial model $\Delta C_L^{\phi\phi}/C_{L,\mathrm{fid}}^{\phi\phi}$ (red, 68% and 95% CL). Compared with the prior constraints (black, same CL), the data are informative mostly around $L \sim 120$, favoring high lensing power, and above $L \sim 250$ the prior dominates.

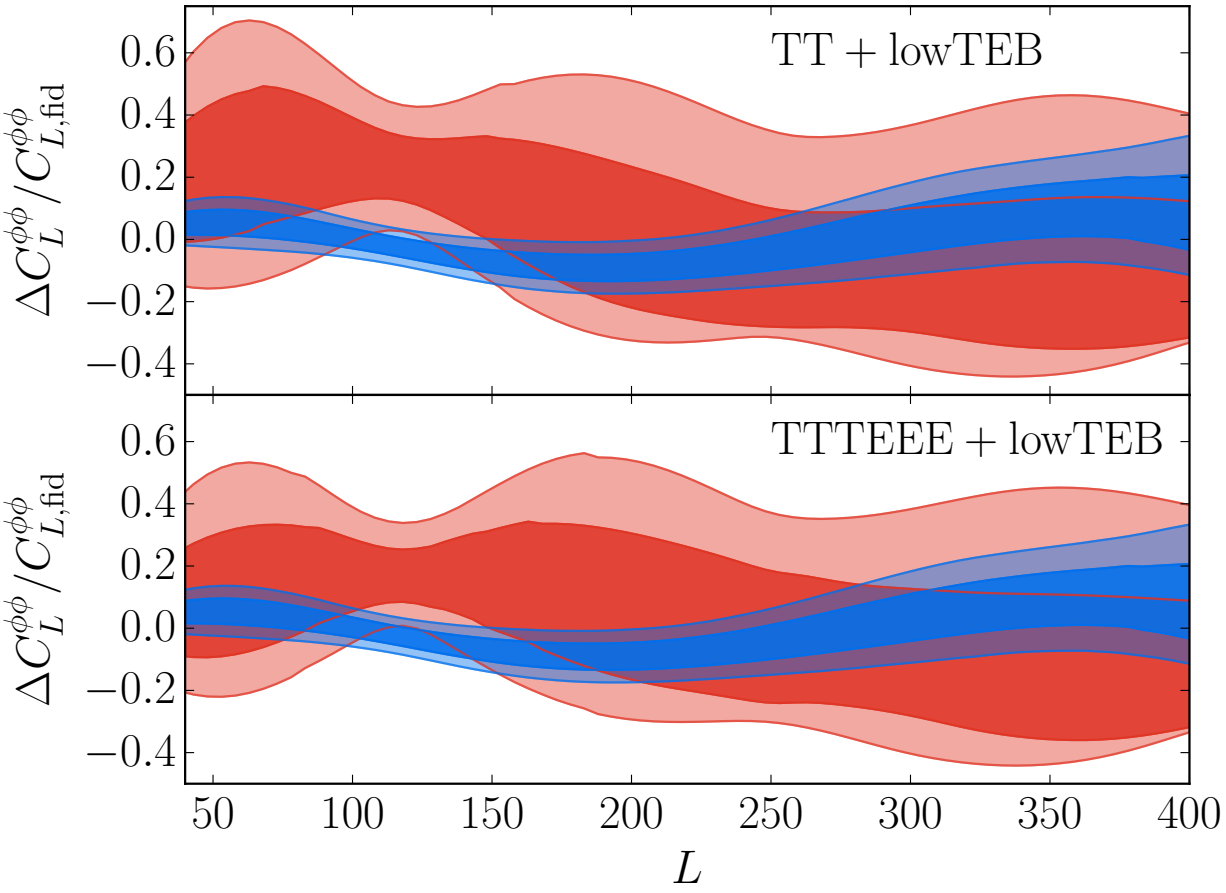

Figure 4.7: CMB power spectrum constraints on the filtered $\Delta C_L^{\phi\phi}/C_{L,\mathrm{fid}}^{\phi\phi}$ as in Fig. 4.6 compared with that of lens reconstruction from Fig. 4.3 (blue). Top panel shows constraints from `TT+lowTEB` and bottom panel from `TTTEEE+lowTEB` which adds high-ℓ polarization.

Within the ΛCDM we can further study the origin of this tension. From the same `TT+lowTEB` analysis, we can predict $C_L^{\phi\phi}$ from information in the unlensed CMB power spectra at each sampled parameter point $\tilde{\theta}_A$ under the ΛCDM assumption. We can then translate this prediction into $\Theta^{(i)}$ by inverting Eq. (4.1). These ΛCDM predictions, shown as the green contours in Fig. 4.4, can be directly compared with the lensing PC measurements themselves. Some tension between the red and green contours is visible, as they overlap only at the $\sim 95\%$ confidence levels; this is the lensing PC version of the well-known A_L lensing anomaly in the high-ℓ TT data.

Unlike A_L, which only indirectly specifies $C_L^{\phi\phi}$ by changing its amplitude relative to the ΛCDM prediction point by point in its parameter space, PCs directly change the amplitude and shape of $C_L^{\phi\phi}$. This allows us to more directly quantify the origin of lensing tension. It is straightforward to trace back the origin of the ΛCDM degenerate direction in the $\Theta^{(1)} - \Theta^{(2)}$ plane: arrows in Figure 4.5 show how these two parameters change when we increase values of A_s and $\Omega_c h^2$ (at fixed θ_* and other parameters; constructed from the partial derivatives listed in Tab. 4.3), which within ΛCDM are the two parameters with dominant effects on $C_L^{\phi\phi}$. Given current constraints on τ, the degenerate direction is mainly aligned with that of A_s, with a smaller contribution from $\Omega_c h^2$. On the other hand, the lensing PC constraints from `TT+lowTEB` mainly reflect $\Theta^{(1)}$ and are driven by the $L \sim 125$ region of the lens power spectrum that is best measured by the TT spectrum. Though they are lens model independent, the lens reconstruction constraints are in good agreement with the ΛCDM constraints in green. Furthermore, the near alignment of the directions of the ΛCDM constraints and the reconstruction constraints (blue) also suggest that the tension with power spectrum constraints (red) cannot be significantly relieved by going beyond ΛCDM.

We can also compare the temperature power spectrum of the maximum likelihood ΛCDM model with that of the maximum likelihood model with lens PCs to see what part of the temperature power spectrum data drives this preference for anomalous lensing; we show

Table 4.3: Dependence of $C_L^{\phi\phi}$ on selected ΛCDM parameters

	$\Theta^{(1)}$	$\Theta^{(2)}$
$\partial\Theta^{(i)}/\partial(\Omega_c h^2)$	82.0	99.1
$\partial\Theta^{(i)}/\partial \ln A_s$	7.45	5.95

cases where either one or four lens PCs are varying from their fiducial values. In Fig. 4.8, we show the residuals relative to the best fit ΛCDM model scaled by the cosmic variance errors per multipole,

$$\sigma_\ell^{TT} = \sqrt{\frac{2}{2\ell+1}} C_\ell^{TT}, \tag{4.3}$$

evaluated at the fiducial ΛCDM model. Notice the Planck data are binned and so the standard deviations of the data can be smaller than σ_ℓ^{TT}. When searching for the best fit PC model, we fix the foreground parameters to their best fit ΛCDM values from the `TT+lowTEB` likelihood, for which the visualization of the Planck data points were derived. In the lower panel of Fig. 4.8, we then show the cumulative improvement over ΛCDM in $2\Delta \ln \mathcal{L}$ of the fit as a function of the maximum ℓ.[2] The total reaches $2\Delta \ln \mathcal{L} = 6.0$ at the highest multipole employed in the analysis when allowing four lens PCs to vary. As is visible from the figure, $2\Delta \ln \mathcal{L} \approx 5$ of 6 comes from the first lens PC, in agreement with our previous statement that majority of the lensing information in the temperature power spectra is well captured by a single lensing component.

The data points show oscillatory residuals with respect to the ΛCDM model in the ℓ range 1250–1500 that indicate smoother acoustic oscillations (see also [53, 54]). Correspondingly, the largest part of the improvement arises through fitting these residuals by increasing the smoothing due to lensing, though notable contributions come from the `lowTEB` part of the likelihood. The latter is associated with the ability to lower TT power at $\ell \lesssim 30$.

These improvements allowed by releasing $C_L^{\phi\phi}$ from its ΛCDM value also lead to shifts in cosmological parameters; these shifts are summarized in Figure 4.9, for the case where the

2. Due to different binning schemes used by the Planck collaboration for their best fit TT power spectrum and binned TT likelihood, we use the unbinned Planck TT likelihood to obtain this plot.

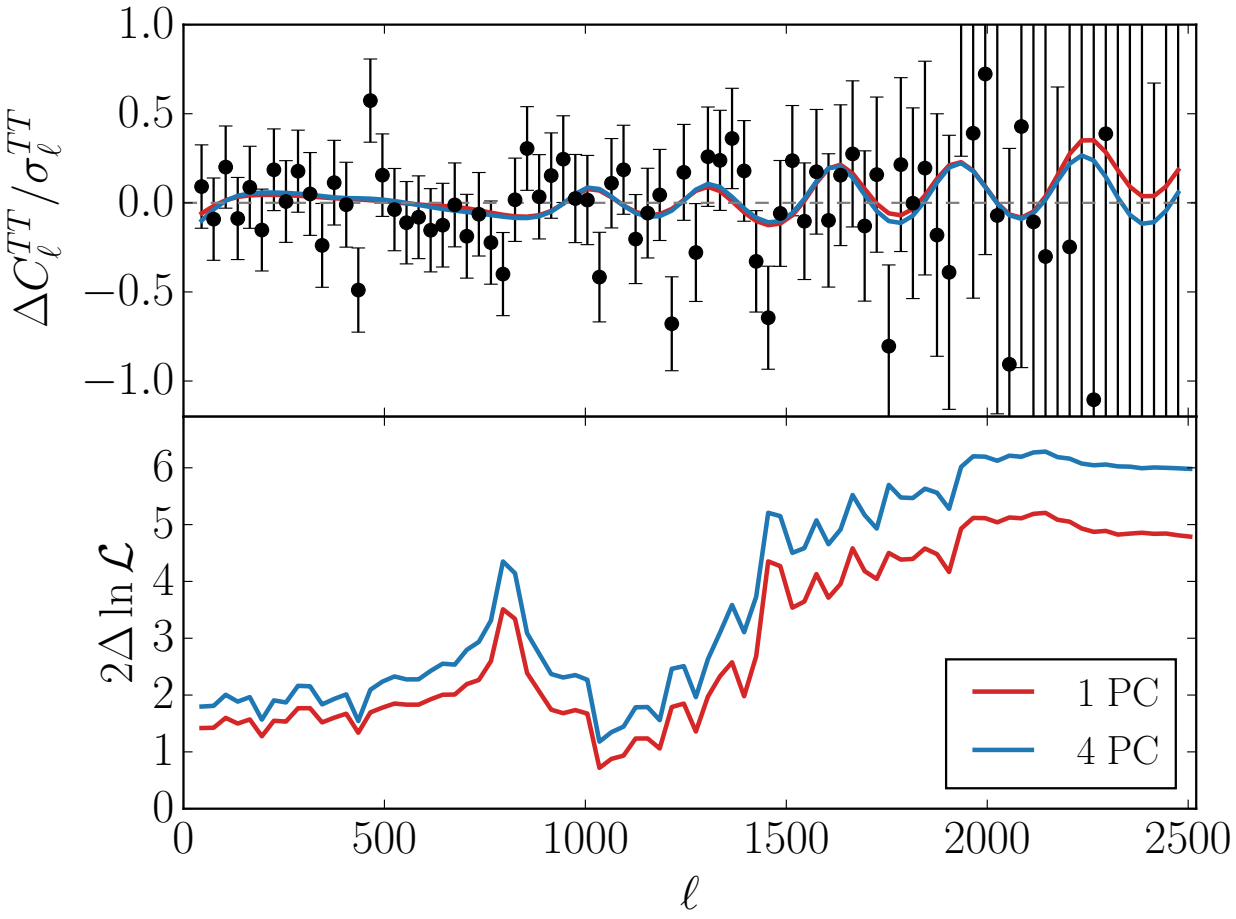

Figure 4.8: Top: Residuals between Planck temperature power spectrum measurements and the best fit ΛCDM model given the `TT+lowTEB` likelihood (points, scaled to cosmic variance errors per multipole σ_ℓ^{TT}). The blue (red) line shows the best fit once we allow four (one) lensing PCs to vary, with fixed foregrounds. Bottom: improvement in the cumulative $2\ln\mathcal{L}(\leq \ell)$ over ΛCDM for the same models showing that most of the improvement is from the first PC and corresponds to smoother acoustic peaks in the $\ell \sim 1250 - 1500$ range.

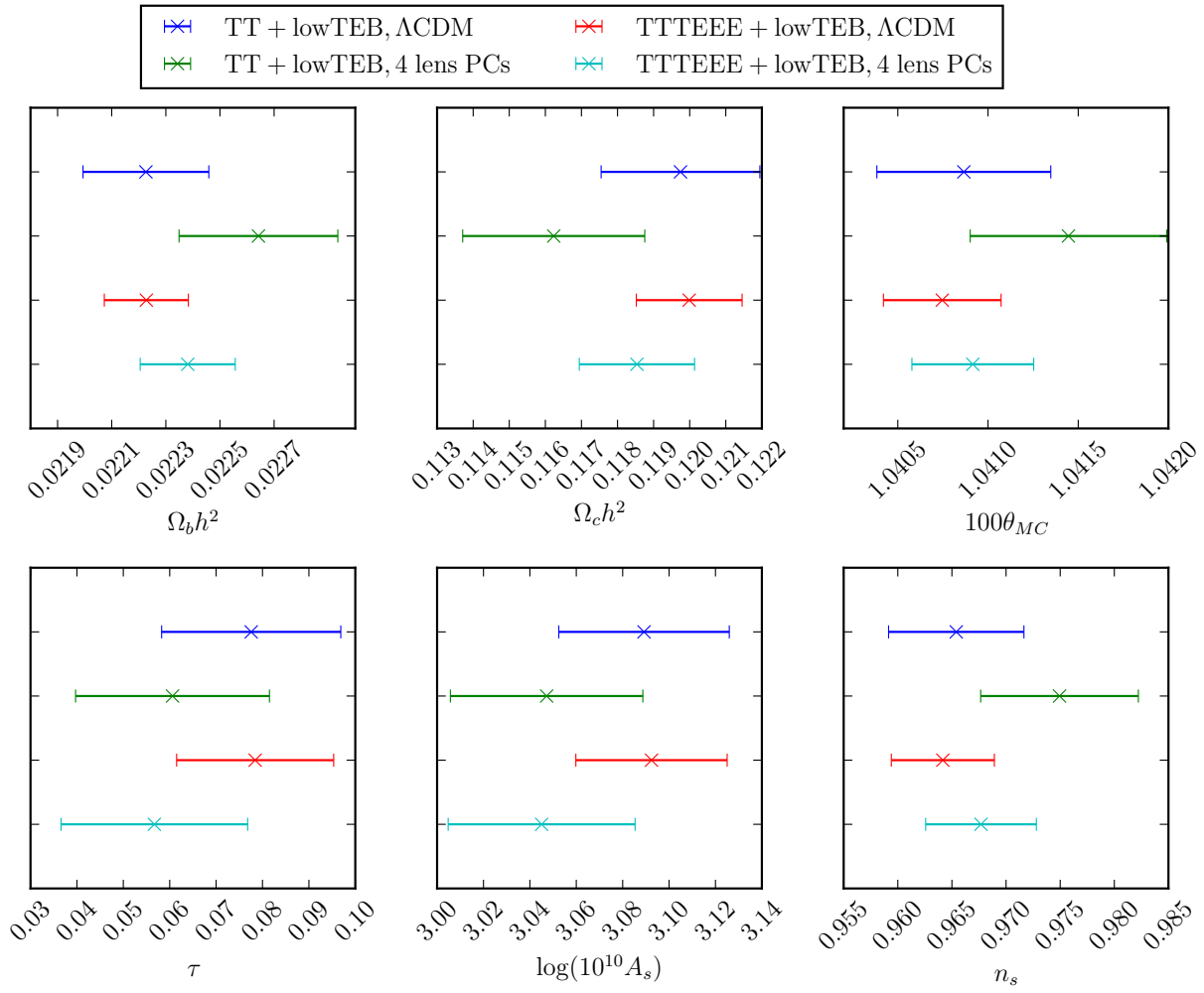

Figure 4.9: Cosmological parameters constraints from `TT+lowTEB` and `TTTEEE+lowTEB` with the fiducial lensing 4 PC analysis (green, cyan) compared with ΛCDM (blue, red). The former correspond to constraints on $\tilde{\theta}_A$ from the unlensed power spectra.

foreground parameters are again allowed to vary. In ΛCDM, preference for fitting the oscillatory residuals pushes values of $\Omega_c h^2$ and A_s up, which then forces other ΛCDM parameters to compensate. In the PC case, lensing parameters $\Theta^{(i)}$ play this role and allow $\Omega_c h^2, A_s$ to drop. This drop and the associated changes in other parameters allows for a lower low-ℓ TT power with respect to the acoustic peaks and therefore also allows a better fit to the anomalously low TT power at $\ell \lesssim 30$. In models with the ΛCDM expansion history such a drop also simultaneously raises H_0 to (69.1 ± 1.2) km/s/Mpc and can help relieve tension with the local distance ladder measurements [6].

Taken at face value, these mild tensions and their alleviation with lensing PC parameters would motivate explorations of additional physics at low z which modify the lens potential. However, independent of the model for the lens potential, tension with lensing reconstruction remains.

4.2.3 Polarization constraints

Next, we add the high-ℓ polarization constraints using the `TTTEEE+lowTEB` likelihood; the various constraints on $\Theta^{(1,2)}$ are shown in Fig. 4.10. The 2015 Planck polarization data is known to be subject to systematics that make lensing conclusions unstable [52] and thus we consider their addition separately.

The main change is a shift in the contours to lower values of $\Theta^{(1)}$ but with tighter errors. This shift is driven by the C_ℓ^{TE} data; lensing constraints from C_ℓ^{EE} are notably weaker and additionally favor even more lensing than C_ℓ^{TT} does [52]. With polarization, the tension between CMB power spectra and lens reconstruction constraints only mildly relaxes. This is because of the combination of the shift and the smaller errors in Fig. 4.10. In Fig. 4.7 (bottom), we also show the impact of adding polarization data on the filtered $C_L^{\phi\phi}$ constraints. Correspondingly, polarization data only mildly decreases the significance of tension around $L \sim 125$.

The internal tension between temperature-polarization power spectra and the ΛCDM prediction in green relaxes somewhat more. This is because polarization favors the high $\Omega_c h^2$ values of the best fit ΛCDM model to `TT+lowTEB` (as shown in Fig. 4.9) due to unusually strong TE constraints in the region around $\ell \sim 200$ [54]. This preference is in a region that is relatively unaffected by lensing and so remains after releasing $C_L^{\phi\phi}$. Raising $\Omega_c h^2$ in ΛCDM has the effect of increasing lensing making the temperature-polarization power spectra and ΛCDM somewhat more consistent.

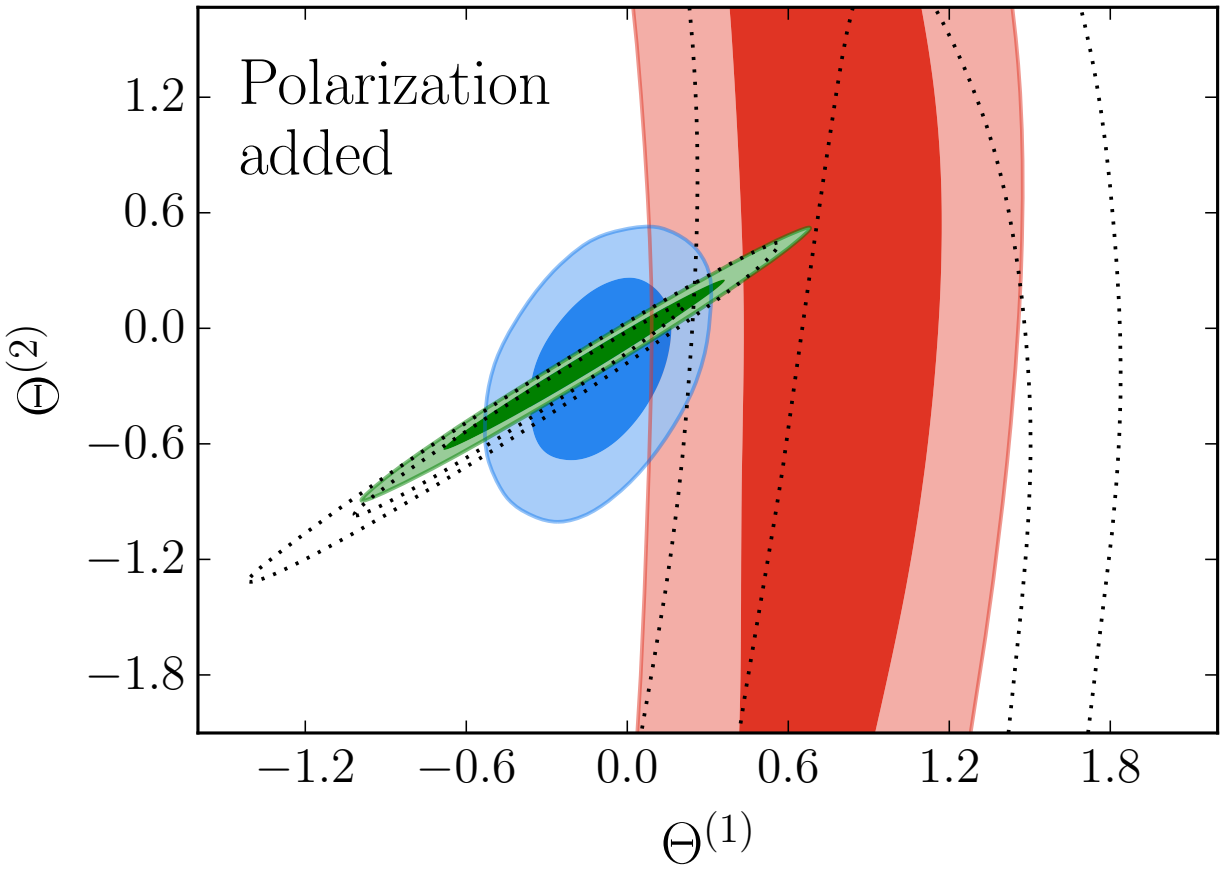

Figure 4.10: Impact of high-ℓ polarization on PC constraints from Fig. 4.4 (repeated with dotted contours for comparison). While tension between the `TTTEEE+lowTEB` (red) and the ΛCDM results (green) weakens slightly, its tension with `PP` remains nearly the same due to its shift and reduced errors in the $\Theta^{(1)}$ direction.

4.2.4 Robustness tests

To check that the results are stable with respect to the considered number of lens PCs, we repeat our analysis with $\Theta^{(4)}$ fixed to its fiducial value. In Fig. 4.11 (top) we show that this does not significantly alter the various constraints on $\Theta^{(1)}, \Theta^{(2)}$ based on `TT+lowTEB` and `PP`. The same conclusion holds when polarization data are added.

We also repeat our analysis with a stronger theoretical prior (with four lens PCs varying) – for $\Theta^{(3)}$ and $\Theta^{(4)}$ we restrict the variation in $C_L^{\phi\phi}$ to be within a factor of 1.4 of $C_{L,\rm fid}^{\phi\phi}$, instead of our default 1.5, while we demand $\Theta^{(2)}$ to be within five standard deviations from the mean value determined from the `PP` likelihood. In Fig. 4.11 (bottom) we show that impact of the theoretical prior on the tension is negligible.

In our analysis we have so far fixed the unlensed CMB to the power spectra allowed by ΛCDM. Given the lensing model-independence of the tension, it is also interesting to ask whether additional physics at recombination can relax it. We can never completely eliminate this possibility for resolution of tension with our methodology, as effects of this new physics might mimic lensing in the CMB power spectrum while not affecting the higher point moments important in lens reconstruction. On the other hand, we can show that the additional physics cannot be simply a change in the effective number of light relativistic species $N_{\rm eff}$. When adding this parameter to the unlensed parameters $\tilde{\theta}_A$ and marginalizing over it, we find that the tension between high-ℓ TT and lensing reconstruction constraints and the internal lensing tension are both still present and similarly significant.

4.3 Significance of the tensions

Having illustrated the existence of lensing tensions in the Planck CMB data, we now turn to quantifying their significance. We start by defining a robust single statistic to compare between the various sources of lensing information. We then discuss the significance of the model-independent tension between lensing constraints from Planck temperature/polarization

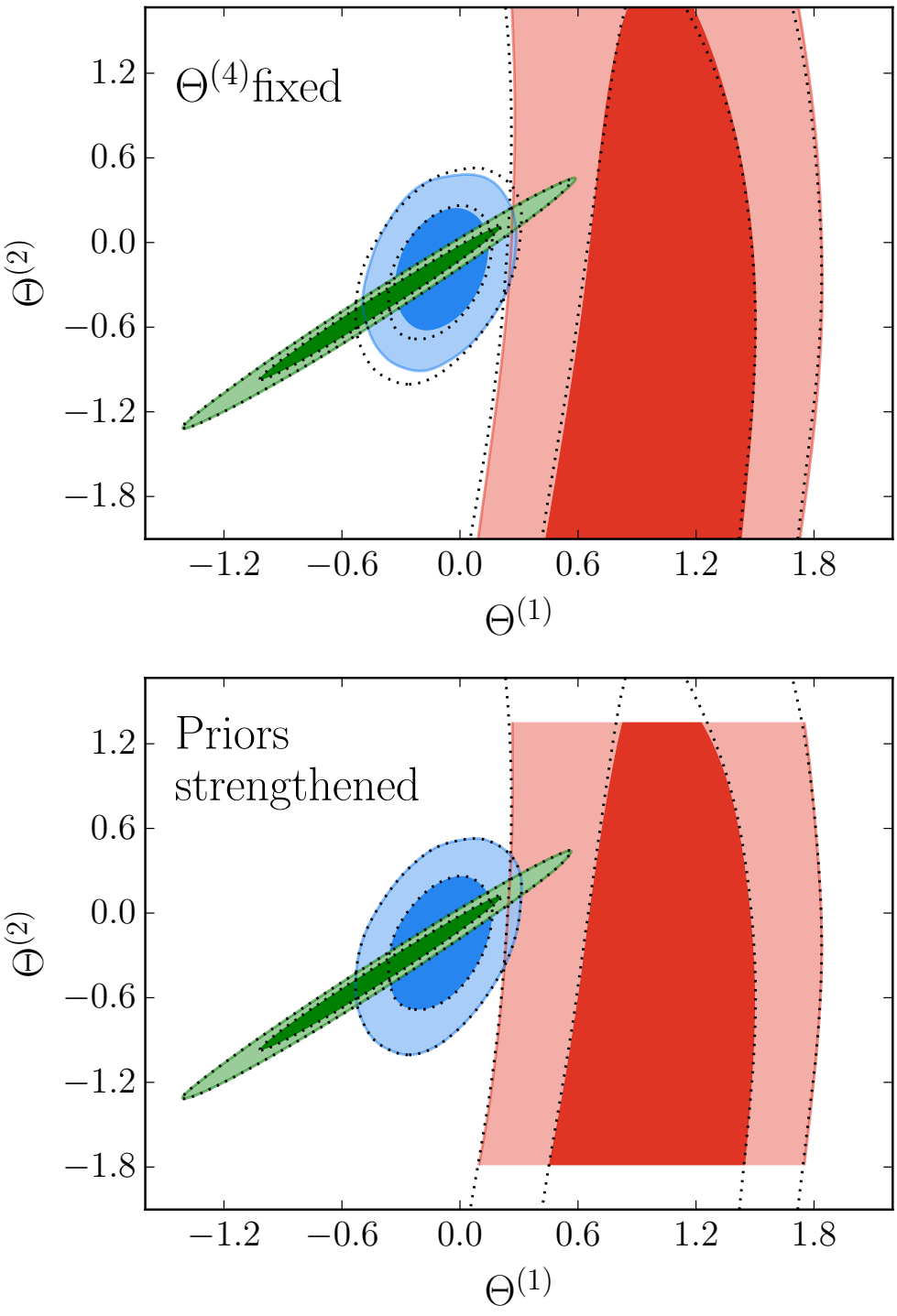

Figure 4.11: Robustness checks on PC constraints from Fig. 4.4 (repeated with dotted contours for comparison). Top: $\Theta^{(4)}$ fixed to its fiducial value instead of marginalized over. Bottom: stronger theoretical prior on $\Theta^{(i)}$ (see the text). Neither change significantly impacts tension between the lensing measurements.

power spectra and lens reconstruction. After that we focus on a special case of ΛCDM with a freely floating amplitude of the lensing potential, which allows us to compare with previous literature and address the significance of the internal tensions between ΛCDM lensing constraints from within the CMB power spectra alone.

4.3.1 Tension statistics

In order to quantify the tension simply and cleanly, we seek to find a single auxiliary parameter whose distribution reflects the best constraints and is as close as possible to Gaussian in each of the lensing measurements. For two such measurements, a natural tension statistic to use is the shift in the means $|\mu_1 - \mu_2|$. To the extent that the parameter posteriors are Gaussian distributed, the shift itself is predicted to be Gaussian distributed with a variance that is the sum of the two variances, $\sigma^2 = \sigma_1^2 + \sigma_2^2$. Therefore, the significance of the measured shift in units of σ is given by

$$T = \frac{|\mu_1 - \mu_2|}{\sqrt{\sigma_1^2 + \sigma_2^2}}. \tag{4.4}$$

To choose the parameter itself, note that the main source of tension is the first principal component $\Theta^{(1)}$ (see Fig. 4.4). However, to have the posterior distributions well approximated by Gaussian distributions, we instead choose

$$W \equiv \exp\left(K_{123}^{(1)}\Theta^{(1)}\right). \tag{4.5}$$

W is independent of the higher lens PCs, as these are not constrained by the temperature and polarization power spectra and thus do not add to the tension.

The scaling factor $K_{123}^{(1)}$ makes W the ratio of the 1 PC filtered and fiducial $C_L^{\phi\phi}$ evaluated at $L = 123$ (see Eq. (4.2)). As we will see, the main benefit of W, or in general a smoothly filtered version of $C_L^{\phi\phi}$, is that it represents a weighted average in L of the data even though it appears to be evaluated at a fixed L. As such it employs the constraining power of the full range of the data. This leads to a powerful and robust tension statistic.

Table 4.4: Tension significances when comparing W constraints from a reference data set to CMB power spectra constraints

ref. data	$C_L^{\phi\phi}$ freedom	TT+lowTEB	TTTEEE+lowTEB
PP	4 PCs	2.4	2.2
PP	amplitude $\mathcal{A}$	2.4	2.4
$\tilde{\theta}$ unlensed	amplitude $\mathcal{A}$	2.4	2.1

This should be contrasted with $C_{123}^{\phi\phi}$ itself or more generally the power spectrum at any single multipole L. Its value depends sensitively on the higher PCs, which increasingly fit noise fluctuations, and so represent an ineffective tension statistic when they are included. With our standard 4 PC analysis, this is not a significant problem for $C_{123}^{\phi\phi}$ itself as we shall see in the next section, but by defining tension in W we make it robust to higher PCs as well and immune to reoptimizing the effective multipole for each case.

4.3.2 Model-independent tension

In Fig. 4.12, we compare posterior distributions for W determined from CMB power spectra through the TT+lowTEB, TTTEEE+lowTEB likelihoods to that determined from reconstruction through the PP likelihood; the two types of distributions overlap only in the tails. Gaussians with the same means and variances describe even these overlap regions accurately, which justifies the use of the tension statistic T. The tension between TT+lowTEB and PP determinations of W is significant at 2.4σ; adding polarization data decreases the tension to 2.2σ. We summarize significance of various tensions in Table 4.4.

We now consider several robustness checks on this tension. Using the high-ℓ TT likelihood liteTT with marginalized foregrounds instead of TT in the analysis leads to the same tension significance of 2.4σ. When the data-driven prior on $\Theta^{(2)}$ of six standard deviations from the PP constraint is dropped, the tensions relax both by about 0.1σ. This is caused by the small curvature of the posterior in the $\Theta^{(1)} - \Theta^{(2)}$ plane, visible for example in the red contour in Fig. 4.10, which leads to an increased overlap with the lensing reconstruction constraints after the projection onto W.

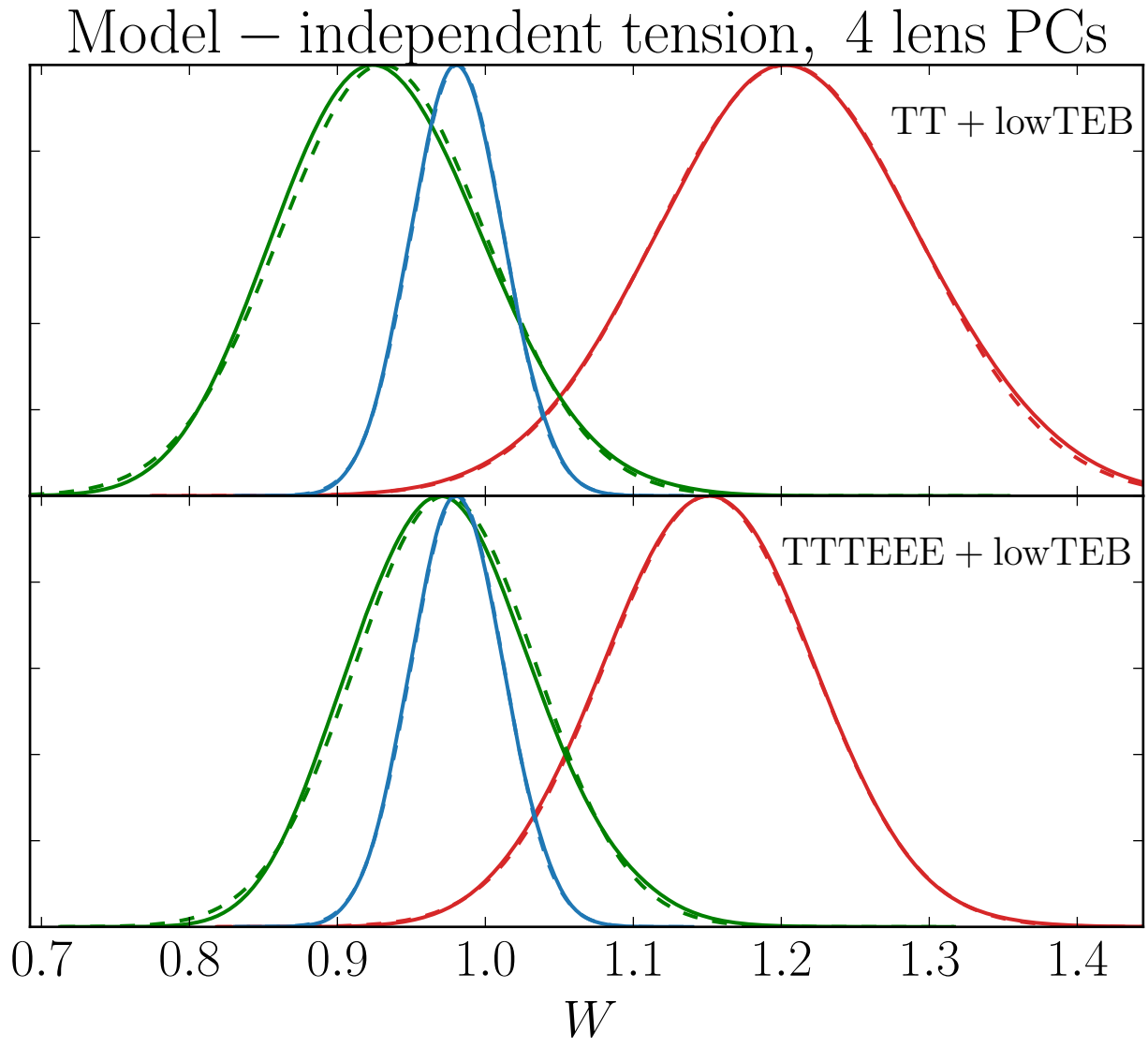

Figure 4.12: Posterior probability distribution for the lensing tension parameter W as determined from the fiducial 4 PC analysis of lens reconstruction `PP` (blue), and CMB power spectra `TT+lowTEB` (red, top) and `TTTEEE+lowTEB` (red, bottom). In green we show constraints on W derived from $\tilde{\theta}_A$, obtained under the assumption of ΛCDM from either `TT+lowTEB` or `TTTEEE+lowTEB`. Dashed lines show Gaussian distributions with the same means and variances.

Next we consider robustness to the constraint on the reionization optical depth τ. The upcoming final release of Planck data is expected to improve and potentially change these constraints. Furthermore, constraints on τ depend on the form assumed for the ionization history that is taken to be step-like in the standard analysis [45, 46]. By isolating the information on the lens power spectrum itself, our tension statistic should be immune to such changes. To quantify the impact of possible future changes in the likelihood, we reevaluate the tension statistic where instead of using `TT+lowTEB` we constrain W using `TT+lowT`, together with a τ prior of width 0.02, centered on either 0.04, 0.06 or 0.08. In all three cases the tension changes by less than 0.02σ from the original result obtained using `TT+lowTEB`. Our conclusions are thus robust to the low-ℓ polarization data and likelihoods. Contrast this with the scaled ΛCDM approach where τ changes the lens power spectrum against which A_L is measured from the temperature power spectrum and lens reconstruction data respectively, leading to sensitivity of A_L constraints to reionization assumptions.

The significance of the tension between `TT+lowTEB` (or `TTTEEE+lowTEB`) and `PP` determinations of W does not notably change when we decrease the freedom in varying $C_L^{\phi\phi}$ by retaining a smaller number of lens PCs in the analysis (see Fig. 4.13).

Finally, it is possible to demonstrate why W is more robust than $C_L^{\phi\phi}$ at some L that has not been specifically optimized for the model-independent lensing test. First, we can take the full 4 PC filtered construction of $C_L^{\phi\phi}$ depicted in Fig. 4.7. We show the resulting tension as a function of L in Fig. 4.14 (black curves) between `PP` and `TT+lowTEB` (or `TTTEEE+lowTEB`). The tension T in $C_L^{\phi\phi}$ constraints at $L \sim 120$ is similar to that in W. On the other hand, choosing other values of L could substantially degrade the ability to identify tension in these cases where the shape of $C_L^{\phi\phi}$ is allowed to vary.

Likewise, an alternate choice of L can make the tension statistic more dependent on the number of lens PCs allowed to vary. In Fig. 4.14, we also show the results of analyses with 1,2 or 3 lens PCs allowed to vary, where $C_L^{\phi\phi}$ is filtered with the same number of PCs. Again, away from $L \sim 120$ the tension significance can vary widely.

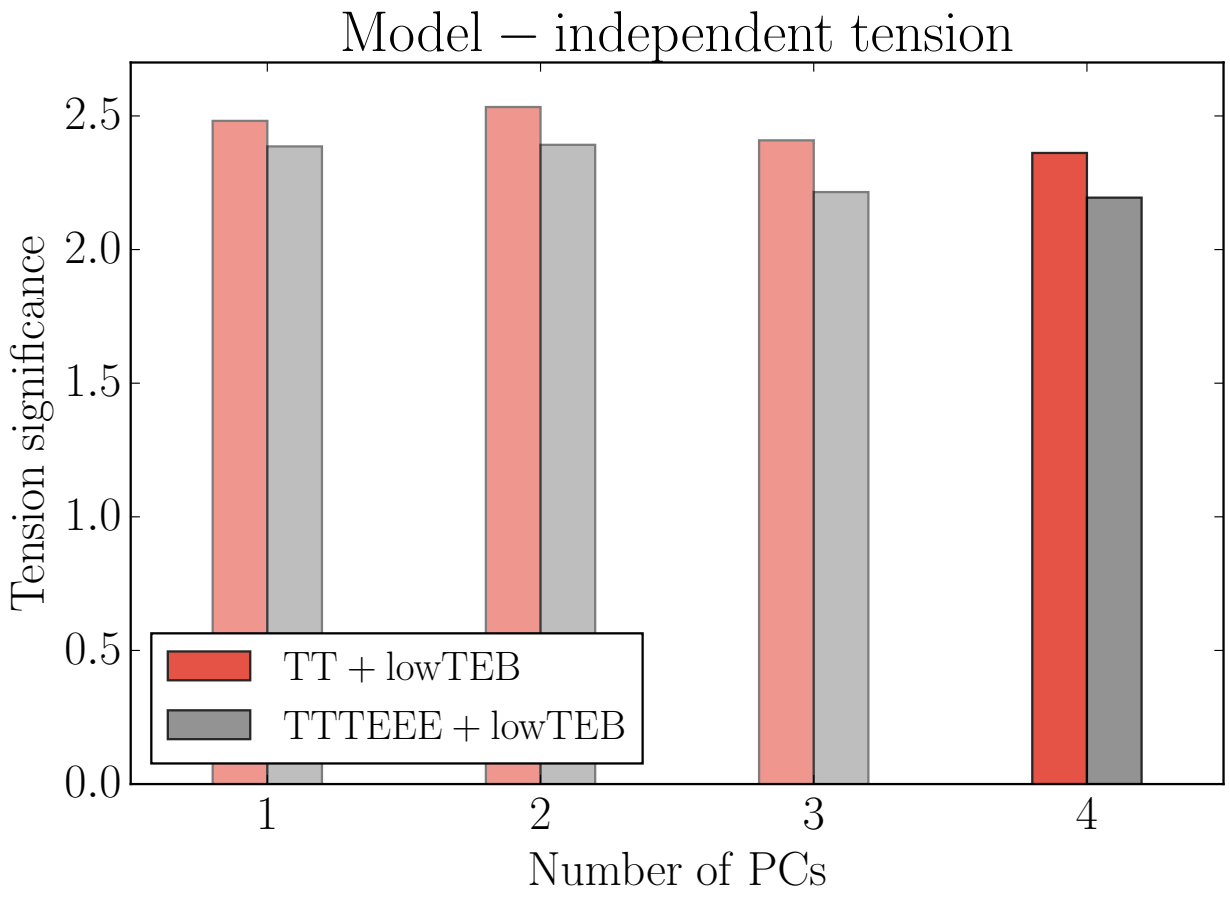

Figure 4.13: Significance of the model-independent tension between `PP` and `TT+lowTEB` (red) or `TTTEEE+lowTEB` (gray) determinations of W, as a function of the number of the lensing PCs which are allowed to vary. The tension significance is measured in units of σ, the expected root mean square of the distance between the means. Our default result that uses the 4 PCs is highlighted.

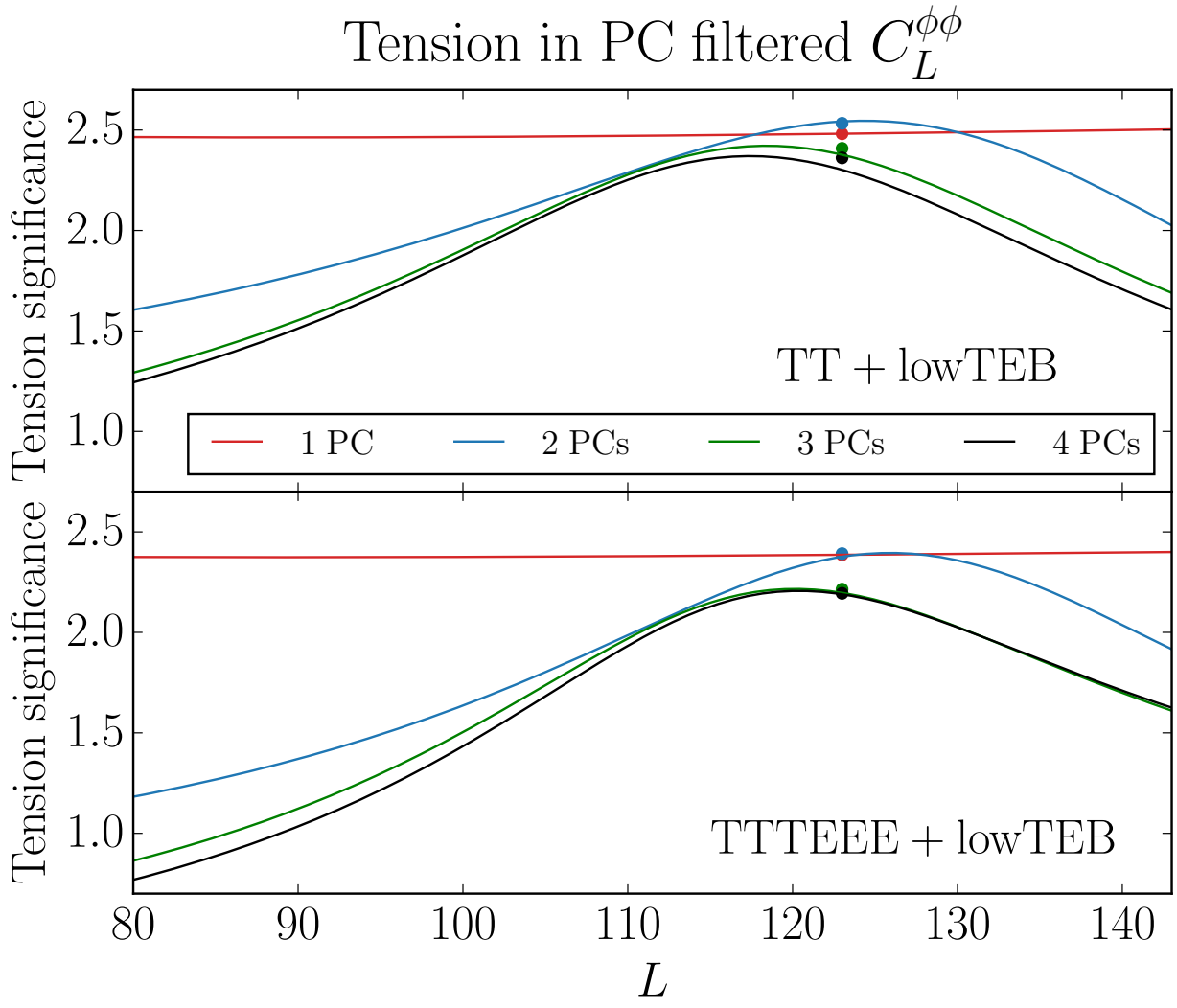

Figure 4.14: Tension significance for the PC filtered $C_L^{\phi\phi}$ from `PP` and `TT+lowTEB` (top) or `TTTEEE+lowTEB` (bottom) for various values of L and number of lensing PCs which are allowed to vary. The points represent significance of the model-independent tensions based on W; notice that for one lens PC the two tension statistics are identical at $L = 123$ by construction but that $C_L^{\phi\phi}$ at other values can substantially underestimate tension.

4.3.3 ΛCDM and amplitude changes

Besides the weak theoretical prior, the tension quoted in the previous section was derived without any constraints on the shape of the gravitational lensing potential. By allowing the largest possible freedom, it represents a lower limit on the tension present in the data; particular models can restrict this freedom and consequently lead to a larger significance of the tension. As a simple example and to connect with the earlier literature, we investigate here ΛCDM model with a freely floating amplitude of $C_L^{\phi\phi}$.

We therefore model the lensing potential as

$$C_L^{\phi\phi} = \mathcal{A} C_{L,\mathrm{fid}}^{\phi\phi}; \tag{4.6}$$

below we refer to this model as "fid + $\mathcal{A}$" but recall that the fiducial model is set by the best fit ΛCDM parameters in Tab. 4.2. Note that this is different from the standard A_L and $A_{\phi\phi}$[3] parameters in that the amplitude multiplies a fixed fiducial model. Constraints on W from these two data sets are shown in Fig. 4.15 (top). Comparing these two constraints leads to a tension of 2.4σ, the same as the model-independent tension derived in the previous section. When adding polarization data, the tension evaluates to the same 2.4σ, slightly more than the model-independent value; see Fig. 4.15 for changes in the posteriors. Comparing instead constraints on $\mathcal{A}$ directly leads to the same tension significance both with and without polarization. The good agreement with constraints on $\mathcal{A}$ gives further evidence that W is a powerful and robust tension indicator, even though it is constructed from a single PC.

With W we can also compare the predictions from the unlensed parameters $\tilde{\theta}_A$ in the same fid+$\mathcal{A}$ context. These correspond to the green curves in Fig. 4.15 and when compared with their red counterparts evaluate to internal tensions significant at 2.4σ for `TT+lowTEB`, respectively 2.1σ for `TTTEEE+lowTEB`.

Within the fid+$\mathcal{A}$ model considered here, constraints on any $C_L^{\phi\phi}$ show the same sig-

3. $A_{\phi\phi}$ is a parameter that scales the lensing potential used in the `PP` but not the one used in the `TT` likelihood.

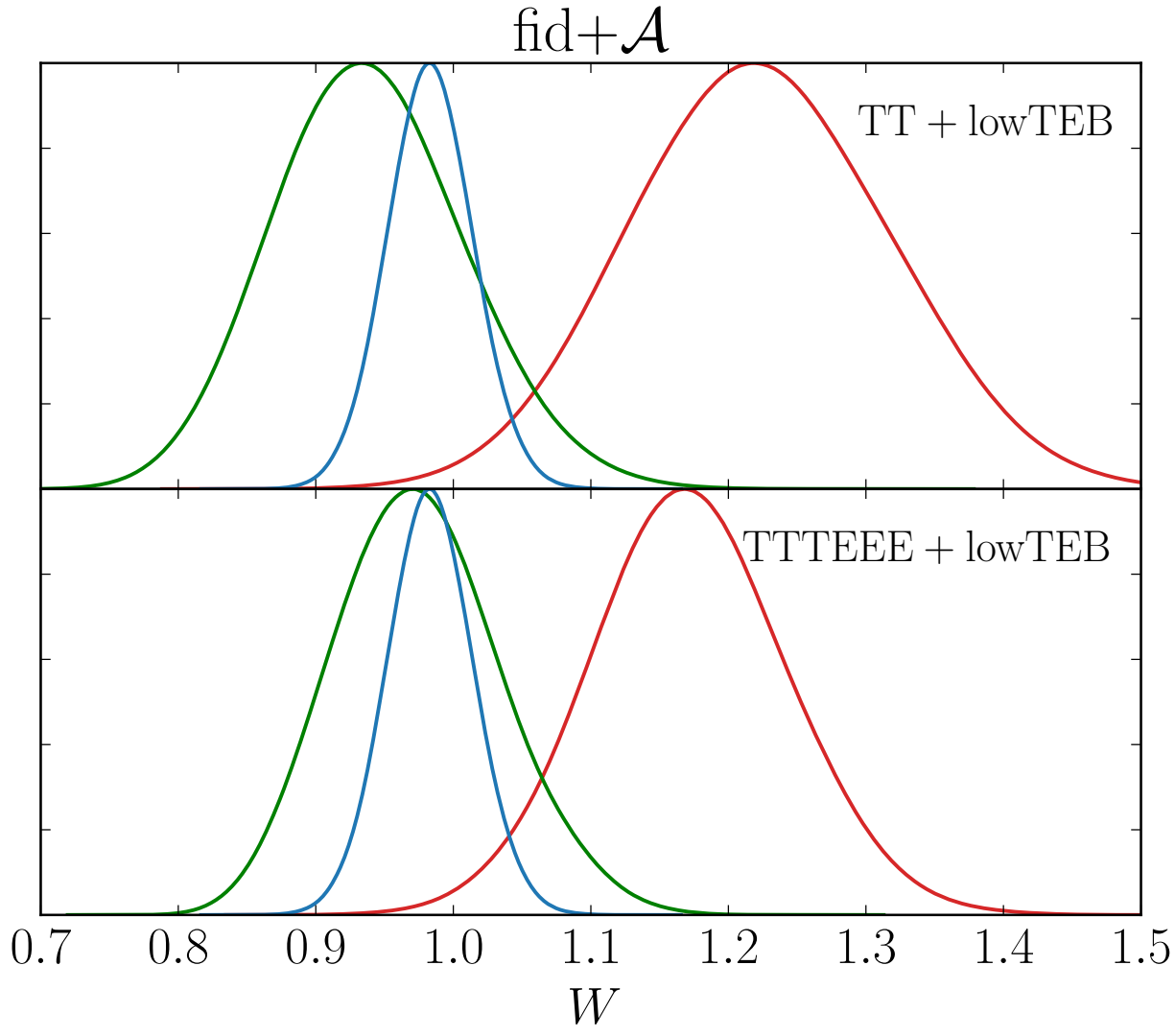

Figure 4.15: Posterior probability distributions for the lensing tension parameter W as in Fig. 4.12 but allowing only for amplitude changes with the fid+$\mathcal{A}$ model.

nificance of the tension as $\mathcal{A}$ (see Fig. 4.16, solid vs. dashed lines). Nonetheless, there are subtleties in using $C_L^{\phi\phi}$ itself as a tension indicator beyond $\mathcal{A}$, even for parameterizations that are motivated by ΛCDM. As we argued above, to quote tension in $C_L^{\phi\phi}$ measurements, one has to exactly specify how much freedom in the lensing potential is allowed; in the PC case, this turns into a sensitivity to the number of PCs involved.

For variations motivated by ΛCDM, one has to carefully specify which parameters are allowed to independently vary between the reconstruction and CMB power spectra analyses. For example, let us take the case of comparing the temperature power spectrum `TT+lowT` and lens reconstruction measurements as commonly considered in the literature. For the former case we further take the usual ΛCDM+A_L approach which allows some variation in the shape of the lensing power spectrum through the cosmological parameters. Without the low-ℓ polarization data, we must specify the prior on τ since it controls A_s through the measured amplitude of the temperature peaks. For definiteness let us take a Gaussian prior of $\tau = 0.07 \pm 0.02$.

Given reconstruction data alone, ΛCDM allows both amplitude and larger shape changes since the cosmological parameters are not constrained by CMB power spectra. For definiteness, let us take the joint posterior of the ΛCDM parameters $\ln A_s, n_s, \Omega_c h^2, \Omega_b h^2$ with Gaussian priors $\Omega_b h^2 = 0.0223 \pm 0.0009$ and $n_s = 0.96 \pm 0.02$. Constraints on $C_L^{\phi\phi}$ when allowing these variations are shown in Fig. 4.16 (red vs. blue contours). Note that as L decreases, these additional shape variations in $C_L^{\phi\phi}$ weaken the apparent tension.

When one compares constraints on $C_{100}^{\phi\phi}$, this is the technique used in Ref. [53][4]. At $L = 100$ the shape variation only has a mild effect that is further reduced by the shift in both contours so for $C_{100}^{\phi\phi}$ we retain a tension significance of 2.4σ.[5]

At lower L the shape variations become more important. On the lensing reconstruction side, the ΛCDM parameters are not well constrained and allow values that are inconsistent

4. Marius Millea, private communication

5. The small difference from the value 2.3σ quoted in Ref. [53] can be caused by different analysis choices.

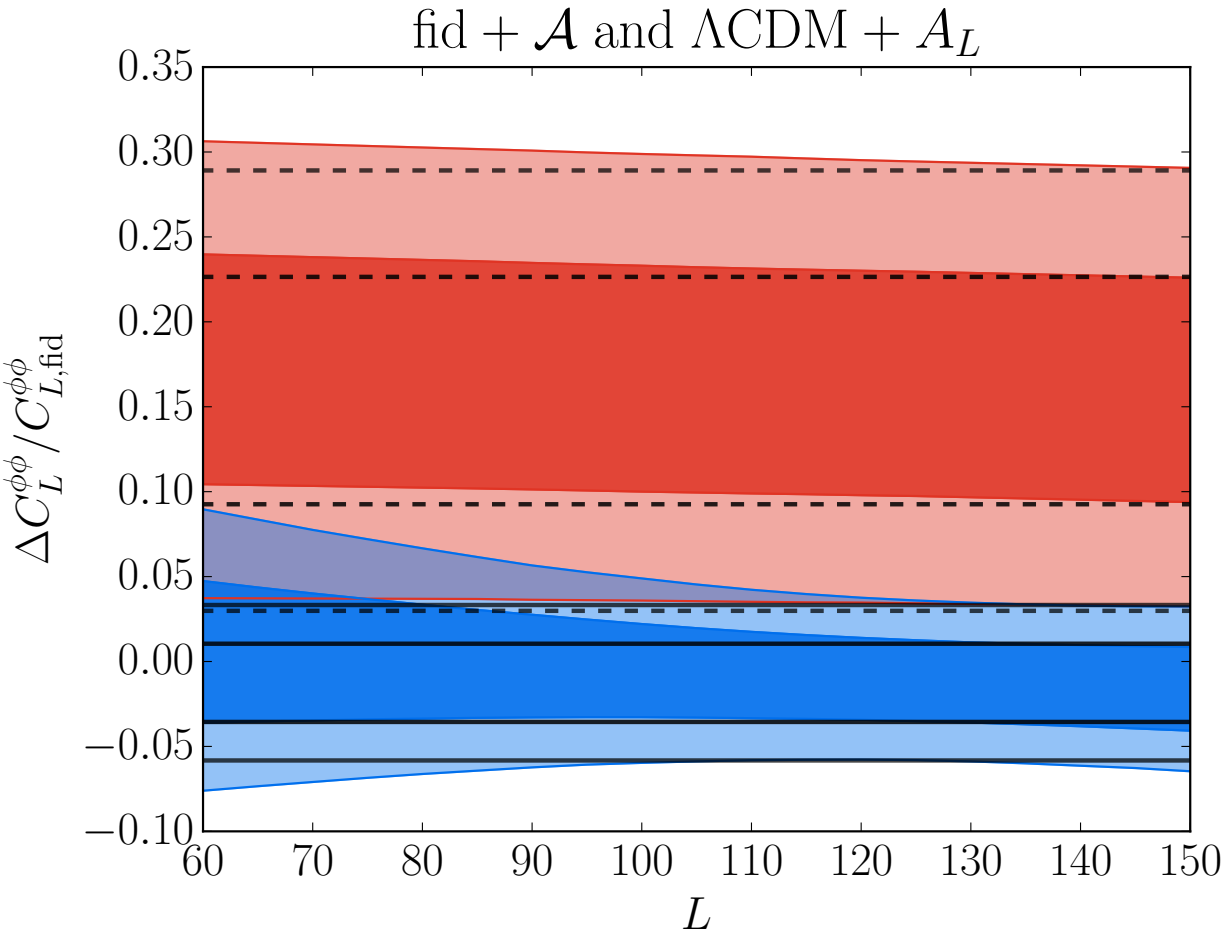

Figure 4.16: Constraints on $\Delta C_L^{\phi\phi}/C_{L,\mathrm{fid}}^{\phi\phi}$ as in Fig. 4.7, but for amplitude and ΛCDM shape variations. The black lines show results from `TT+lowTEB` (dashed) or `PP` (solid) within the fid+$\mathcal{A}$ for amplitude variations. Filled contours are determined from `TT+lowT` within ΛCDM+A_L with a τ prior (red) and separately from `PP` with ΛCDM freedom on the amplitude and shape but with fixed τ, θ_* and a prior on $\Omega_b h^2$ and n_s (blue). Constraints, especially at low L from the latter, depend on which ΛCDM parameters are allowed to separately vary.

with the unlensed CMB; this leads to the shape variations noticeable at low L in Fig. 4.16. Had we allowed even larger freedom in $C_L^{\phi\phi}$ by changing say the prior on n_s on the reconstruction side, the apparent tension would further degrade. On the `TT+lowT` side the ΛCDM parameters are very well constrained, leaving less of an effect on the shape of $C_L^{\phi\phi}$ and the contours mostly reflect uncertainty in the amplitude through A_L. However, when more freedom is granted to the lensing potential, the apparently strong constraints at low L degrade (see Fig. 4.7), also decreasing the tension. It is thus important to carefully specify the model freedom in using $C_L^{\phi\phi}$ as a statistic. This problem is largely removed by using W which has the same meaning in all models.

4.4 Discussion

In this chapter we use the technique developed in the previous chapter to illuminate the so-called "lensing tensions" in the Planck CMB data. By modeling the principal components of the lens potential $C_L^{\phi\phi}$ given the Planck CMB power spectra, we isolate the one aspect that is constrained by the data in a model independent way. We then compare this constraint to results from lens reconstruction through the 4 principal components that it constrains to test whether variations in $C_L^{\phi\phi}$ beyond ΛCDM can relax tension between the two different sources of lensing information.

We show that the tension remains between the temperature and lensing reconstruction determinations of $C_L^{\phi\phi}$ even beyond ΛCDM. Previous studies of the Planck lensing anomaly [52, 53, 55, 51] considered only the addition of changes in the amplitude of the gravitational lensing potential from ΛCDM predictions. Our technique extends these studies and clarifies the nature of the tension by extracting direct constraints on $C_L^{\phi\phi}$, which obviates the need for directly specifying ΛCDM parameters in interpreting tension, and allowing shape variations from ΛCDM.

Even allowing for shape and amplitude variations beyond ΛCDM, the tension between temperature and lensing reconstruction remains at a level of 2.4σ, essentially the same as

with amplitude variations alone. The significance decreases mildly to 2.2σ when polarization data are taken into account unlike in the case of amplitude variations; this drop is driven by preference of the TE data for less lensing.

We evaluate these tension significances by using a simple difference of the means statistic tension on a simple function of the first principal component. For the Planck 2015 data which measure only a single aspect of lensing from CMB power spectra, this provides a simple but powerful, robust, and lensing model independent quantification of tension. Our technique can be easily applied to future CMB data sets, where more and mutually correlated aspects are measured, with a suitable generalization of tension statistics (e.g. [56]).

This tension is driven by the multipole range $\ell \sim 1250 - 1500$ in the TT data which prefers smoother acoustic peaks than predicted by the standard physics at recombination and lensing reconstruction. While new physics at recombination could in principle relieve tension, it cannot be relieved by adjusting the relativistic degrees of freedom through $N_{\rm eff}$.

By separating information in the lensed CMB power spectra into lensing and unlensed components, we also enable a consistency check on the ΛCDM cosmological model. Because the ΛCDM prediction based on constraints to the unlensed CMB is consistent with the lensing reconstruction constraints, the internal consistency check fails at similar significance as the comparison of the temperature – lensing reconstruction determinations of lensing potential. Addition of polarization data again decreases the significance of the tension, more so this time due to preference for high $\Omega_c h^2$ in the TE data.

While these tensions may point to systematic errors or a statistical fluke that is resolved by more data and improved data reduction, our technique of extracting direct constraints on the lensing potential from CMB power spectra data should continue to provide a robust and powerful tool for testing the consistency of ΛCDM and searching for new physics in the future.

CHAPTER 5

CONCLUSIONS

With increased precision of the CMB measurements, it will become important to consider sample variance of the gravitational lenses when analyzing the data. In Chapter 2 we show how this effect affects cosmological parameter constraints and point out that neglecting it can lead to problems for concordance studies. As a byproduct, we develop and test an analysis pipeline that takes the lens sample variance effects into account and goes from simulated CMB maps all the way to the cosmological parameter constraints.

Chapter 3 shows how to separate information from the gravitational lensing and from the unlensed CMB spectra and how to compactly describe most of this information in terms of a small number of parameters and their Gaussian likelihood. This separation can be used not only to explain the lens sample variance effects on cosmological parameter constraints, but also to check consistency of the gravitational lensing in the CMB data as it allows direct, model-independent, measurements of $C_L^{\phi\phi}$.

Finally, in Chapter 4 we apply this technique to measure gravitational lensing potential to probe lensing consistency of the Planck satellite data. Even when allowing an arbitrary gravitational lensing potential, we still find tensions significant at more than 2σ level. Without large modifications, similar analyses can be applied to other current and future CMB datasets, providing a useful check for residual systematics and new physics.

APPENDIX A

LENSPIX MODIFICATIONS

To simulate lensed CMB data we modify publicly available code Lenspix [40]. In this code the unlensed CMB is first evaluated on a high resolution equicylindrical grid. The lensed CMB is then evaluated on a lower resolution Healpix grid [57] through a remapping by a deflection field, determined by a gradient of the lensing potential ϕ. Values of the unlensed CMB at points which are remapped onto the Healpix grid points are obtained using a bi-cubic interpolation from the high resolution grid. Our simulations are run with precision parameters `nside` $= 4096$ and `lmax` $= 8000$.

The precision with which the code calculates the lensed power spectra depends on the point density of the high resolution grid, which is parameterized by an oversampling factor `interp_factor`. Simulations with `interp_factor` ~ 2, which were the largest we could originally run on a single node of our computer cluster due to limited memory, lead to lensed CMB power spectra biased at high ℓ. Such bias leads to ~ 0.2 standard deviations shift in the likelihood function in the $\ln A_s$ direction (with other cosmological parameters fixed); we did not investigate other parameters in depth but in general parameters constrained by high ℓ data are sensitive to this bias.

This power spectra bias can be quantified by a parameter

$$\xi = \frac{C^{TT}_{3000}\Big|_{\phi=0} - \tilde{C}^{TT}_{3000}}{\tilde{C}^{TT}_{3000}}, \tag{A.1}$$

relative difference at $\ell = 3000$ of the temperature power spectrum C^{TT} "lensed" in Lenspix by a zero-deflection field and the unlensed temperature power spectrum $\tilde{C}^{TT}$. If interpolation was exact ξ would vanish. However, the unlensed and lensed CMB are evaluated at different grids and interpolation leads to numerical bias even when there is no lensing present. This bias appears to be – up to cosmic variance – independent of the cosmology and comparable in temperature and polarization. It typically grows with investigated multipole, for comparison

we therefore choose the largest data multipole considered for XY power spectra, $\ell = 3000$.

To overcome the large ξ bias and avoid the related shifts in the likelihood function, we modify the code such that it works only with smaller portions of the high resolution map of unlensed CMB at any given time and never stores the whole map in memory. This allows us to run with higher values of `interp_factor` and achieve smaller values of ξ.

We further replace the original high precision calculation of partial derivatives of the unlensed CMB variables, which is part of the Lenspix interpolation algorithm, by a less precise (for a given high resolution grid) but significantly faster routine. This enables us to obtain higher interpolation precision without sacrificing runtime by increasing the density of the high resolution grid of the unlensed CMB.

Finally, the precision of variables describing the angular positions of the points in the high resolution grid is increased to avoid certain artifacts in lensed CMB maps.

We compare values of ξ and runtime for several values of `interp_factor` with the original and simplified calculation of the partial derivatives in Fig. A.1. It is clear that although the original routine is superior for a fixed high resolution grid, for a fixed runtime it is advantageous to use a simpler partial derivative calculation and increase the density of the grid. Simulations used in this work were calculated with `interp_factor` $= 4$.

To judge agreement between the lensed power spectra from simulations and the theoretical expectation calculated by CAMB, we define bias variables

$$b_\ell^{XY} = \frac{\sum_{\ell'} \ell'(\ell'+1)\Delta C_{\ell'}^{XY}}{\sum_{\ell'} \ell'(\ell'+1) C_{\ell'}^{XY,\mathrm{fid}}}, \tag{A.2}$$

which can be evaluated for each simulated CMB sky. Here the sums go over a bin of width $\Delta\ell = 200$ centered on ℓ and $\Delta C_{\ell'}^{XY}$ is a difference between simulated and expected value of power spectra, defined in (2.10). In Fig. A.2 we plot average values of b_ℓ^{XY} from simulations for several values of ℓ; we show the levels of bias achieved with both the simulations settings used in this work and the original Lenspix code with `interp_fact` $= 2$. In the latter, a small

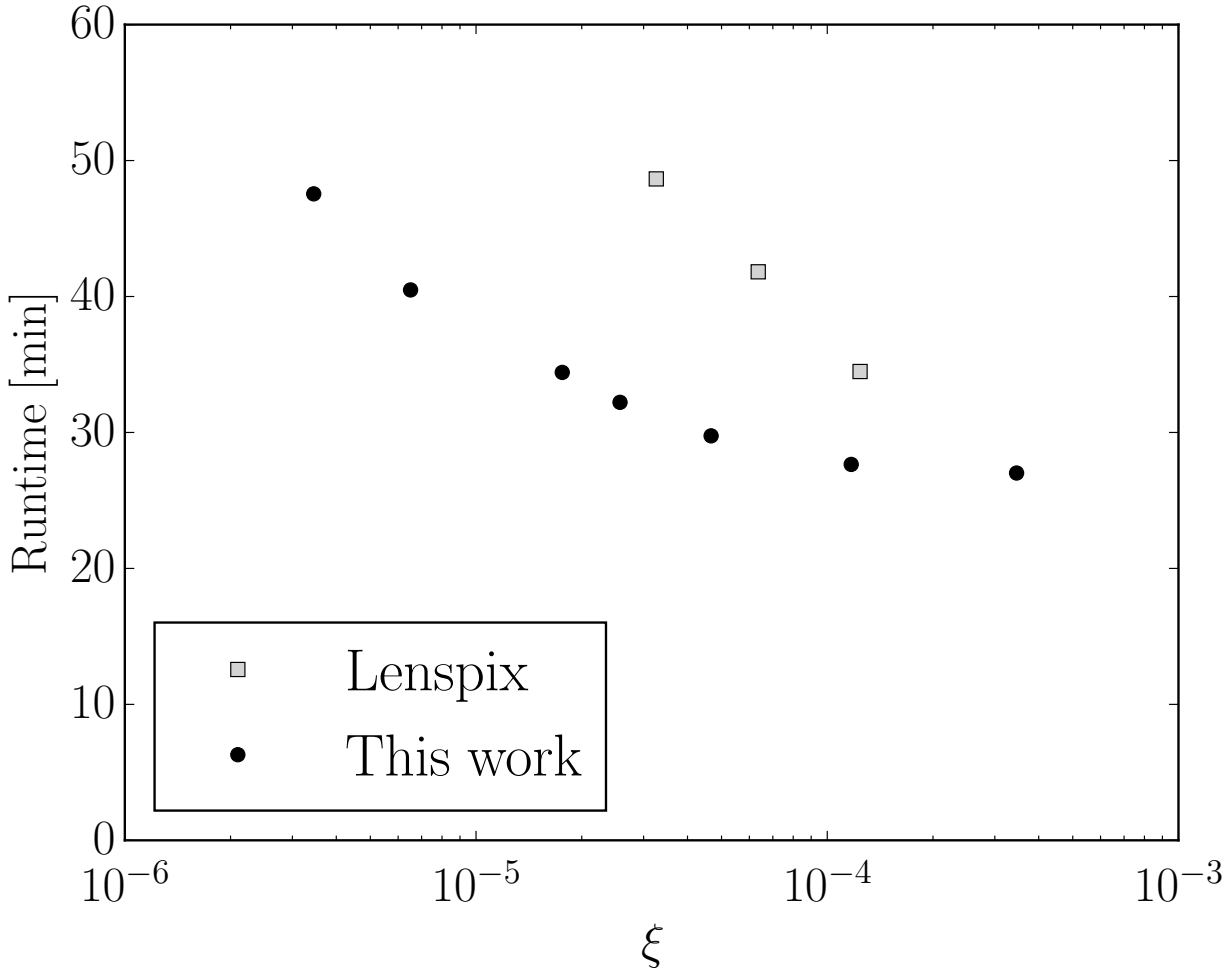

Figure A.1: Bias ξ caused by the interpolation part of the lensing algorithm and corresponding runtime for various values of the precision parameter `interp_factor`. Comparison of the Lenspix interpolation routine (gray squares, from right `interp_factor` values 2, 2.5 and 3) and our modifications (black dots, values 2, 2.5, 3, 3.5, 4, 5 and 6).

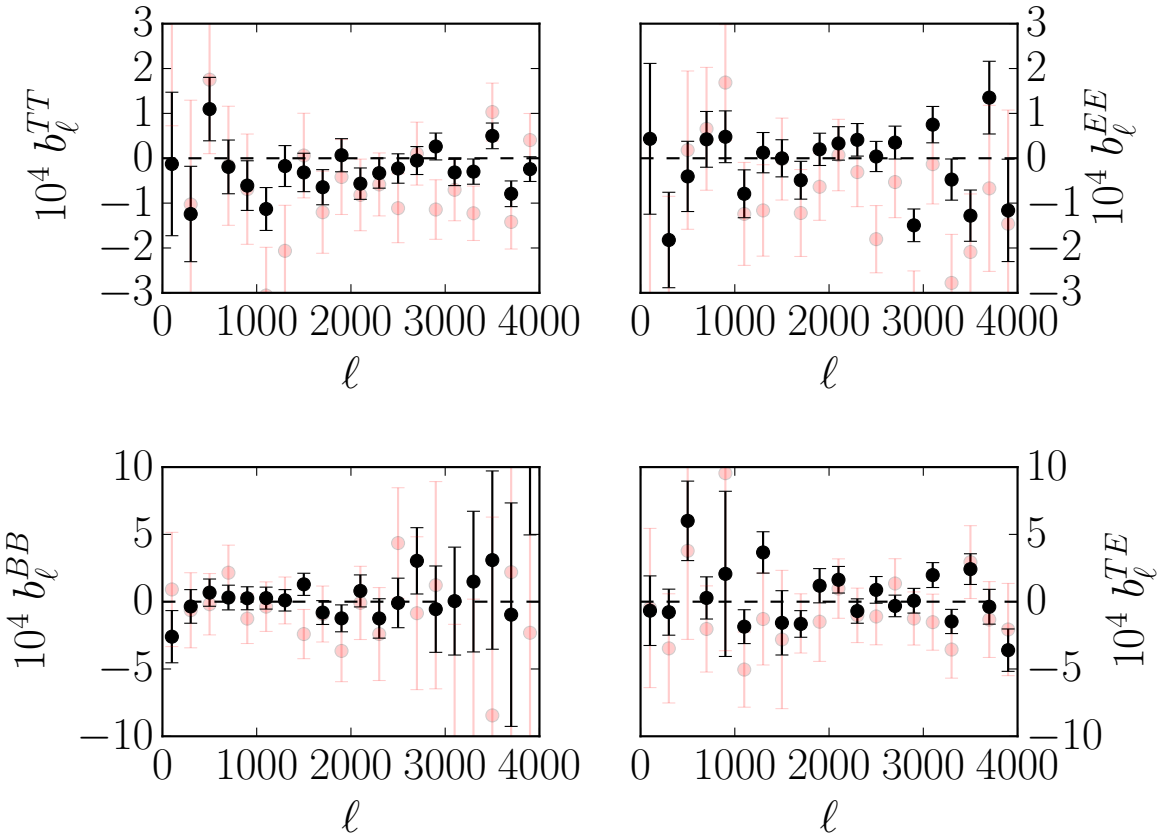

Figure A.2: Lensed power spectra bias b_ℓ^{XY} for several values of ℓ, averaged over 2000 lensed CMB simulations calculated with the precision settings used in this work (black). In red the same quantities determined from 400 lensed CMB simulations calculated with original Lenspix interpolation algorithm with `interp_factor` = 2. Error bars represent errors on the mean estimated from the simulated values.

bias is visible for $XY = TT, EE$.

APPENDIX B

SKY COVERAGE AND OPTICAL DEPTH

A ground-based CMB Stage 4 experiment is unlikely to usefully measure CMB temperature and polarization on the full sky. For that reason, in this Appendix we use a Fisher analysis to reexamine some of the results of Section 2.4 for an experiment which observes 40% of the sky and measures temperature and polarization power spectra in the multipole range $\ell = 30 - 3000$. We additionally neglect covariance induced by the sky mask by simply scaling the full sky covariance with the sky fraction. Information from the largest scales is represented by adding a Planck-like prior on τ, corresponding to a standard deviation of $\sigma_\tau = 0.01$.

As is to be expected, absence of the large scale measurements significantly degrades the absolute constraints on cosmological parameters. However, the relative effects of the non-Gaussian covariance do not become significantly more important. For example, degradation of the most affected parameter combination, as expressed through the ratio $\sigma_M^{\rm ng}/\sigma_M^{\rm g}$ in ΛCDM and analogous ratios for the other cosmological models, increases by less than 4% when omitting information from $\ell < 30$. The largest effect of this omission is in the $\tau - A_s$ plane. When large angle polarization data are improved over Planck, they further break the $A_s e^{-2\tau}$ degeneracy in the heights of the acoustic peaks. Without this improvement, lensing measurements become more competitive in breaking this degeneracy and consequently constraints on these two parameters are degraded by $\sim 10\%$ in all three cosmological models investigated in Section 2.4.

APPENDIX C

NUMBER OF LENSING PRINCIPAL COMPONENTS

Two considerations guide the choice of the number of principal components of the lensing potential to be measured from the lensed CMB power spectra. Keeping a larger number of PCs leads to a more accurate description of the lensed power spectra. On the other hand, increasing number of parameters slows down convergence of the MCMC calculations and requires physicality priors, since the higher PCs are more poorly constrained by definition. In this section we justify our choice of using five PCs for the analyses of our mock CMB-S4 experiment.

First, we look at the fidelity in reproducing lensing effects in the observed C_ℓ^{XY} power spectra. For definiteness, we perturb the fiducial $C_\ell^{\phi\phi}$ by a $\Delta C_\ell^{\phi\phi}$ which corresponds to shifts in the cosmological parameters given in Table C.1 (at fixed unlensed power spectra). This change represents a realistic change in the lensing potential which might be encountered in a real analysis, as cosmological model with parameters from Tab. C.1 is between 68% and 95% probability contours for ΛCDM+w model in the simulation investigated in Section 2.4.3. We chose the parameters such that they approximately lie on the degeneracy direction limited by the lensing information. For completeness and comparison to the results in the main text, the lensing principal components arising from this change are

$$\{\Theta^{(1)}, \ldots, \Theta^{(5)}\} = \{-0.012, 0.11, -0.011, -0.06, -0.012\}. \tag{C.1}$$

Note that the investigated parameter change is not aligned with change of M^w from (C.1), nor need it be since it represents the degeneracy direction rather than the direction most affected by lens covariance.

In top panel of Fig. C.1 we show the resulting C_ℓ^{BB} power spectrum calculated with lensing potential changed by the full $\Delta C_\ell^{\phi\phi}$ vs. when this change is approximated using the first $N \in \{0, 1, 2, 3, 4\}$ lensing PCs; the difference is too small to be visible directly and so

Table C.1: Shifts in the cosmological parameters used to probe approximations of the lensing potential in terms of lensing PCs

Parameter	Shift
h	0.175
$\Omega_c h^2$	-1.0×10^{-3}
$\Omega_b h^2$	3.5×10^{-5}
n_s	1.2×10^{-3}
A_s	-1.6×10^{-11}
τ	-2.2×10^{-3}
w	-0.52

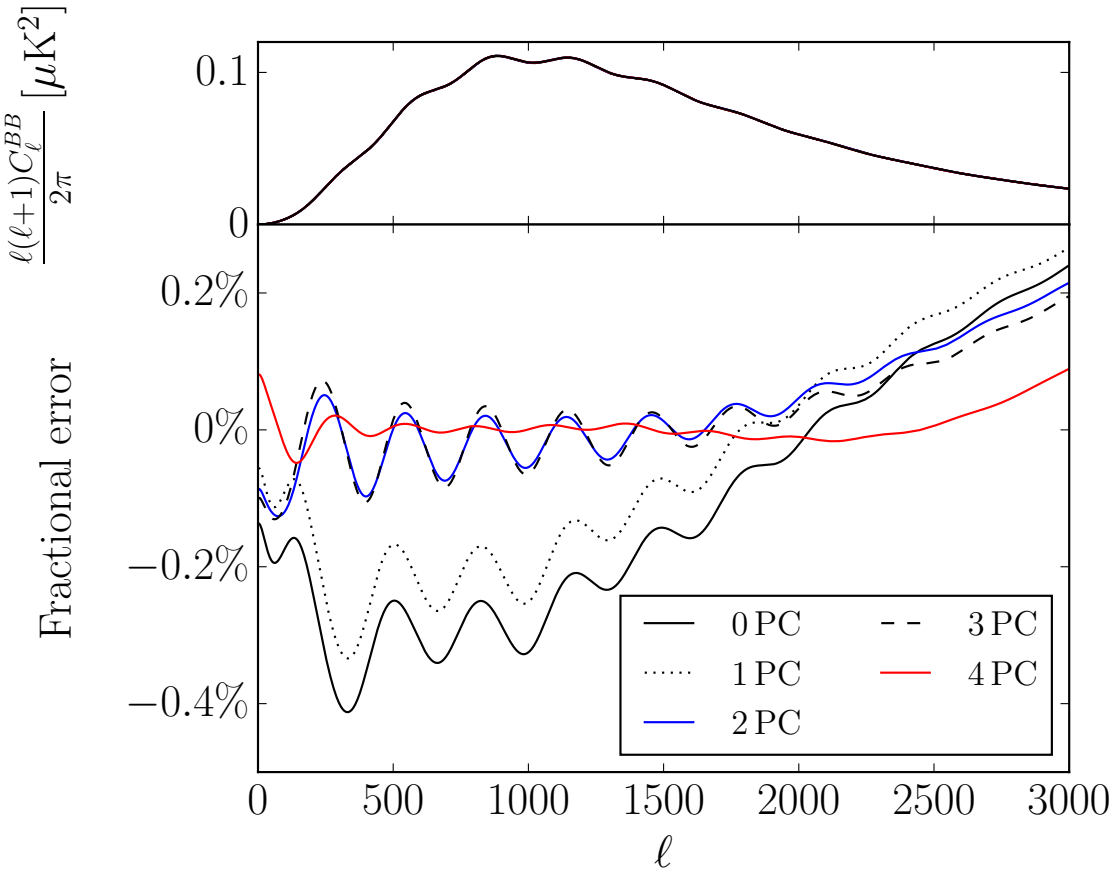

Figure C.1: Lensed C_ℓ^{BB} calculated with lensing potential increased by $\Delta C_\ell^{\phi\phi}$ which corresponds to parameter shifts listed in Tab. C.1 and its representation in terms of the first $N \in 0 \ldots 4$ PCs (top: absolute; bottom percent error between the two).

the bottom panel shows the percent error. Note that the smallness of these changes explains why in the main text approximations based on linearizing power spectra deviations and PC amplitudes are excellent even for relatively large cosmological parameter shifts.

Since the change in Eq. C.1 is dominated by $\Theta^{(2)}$, most of the improvement in fidelity comes when adding that component. In fact for this particular $\Delta C_\ell^{\phi\phi}$, first two PCs are sufficient to faithfully describe effects of lensing in TT, EE and TE power spectra extremely well. The next large jump in fidelity comes with the fourth PC which is associated with the high multipole range of BB in Fig. C.1. We checked several other choices of allowed $\Delta C_\ell^{\phi\phi}$ and for all of them four principal components lead to small errors on the power spectra level.

To quantify the total significance of the errors we construct

$$\chi^2_{\mathrm{PC},N} = \sum_{i,\,j} \delta D_i(N) \left(\mathrm{Cov}_{i,j}\right)^{-1} \delta D_j(N), \tag{C.2}$$

where for brevity we introduce $\delta D_i(N) = \delta C_\ell^{XY}(N)$, the power spectrum error caused by approximating $\Delta C_\ell^{\phi\phi}$ using the first N PCs, with i indexing all multipoles and power spectra types. As N increases, the PCs approximate the full effect of lensing better and $\chi^2_{\mathrm{PC},N}$ decreases. In Fig. C.2 we show this dependence; as we saw before, adding fourth PC leads to a significant improvement in our ability to capture the effects of gravitational lensing on the CMB. For some choices of $\Delta C_\ell^{\phi\phi}$, adding fifth PC improves $\chi^2_{\mathrm{PC},N}$ by a factor of a few on top of the $\sim$ hundred-fold improvement in $\chi^2_{\mathrm{PC},N}$ arising from using four PCs. For this work we decided to include fifth PC into the analysis as well, even though its inclusion is not expected to have any significant impact on the results.

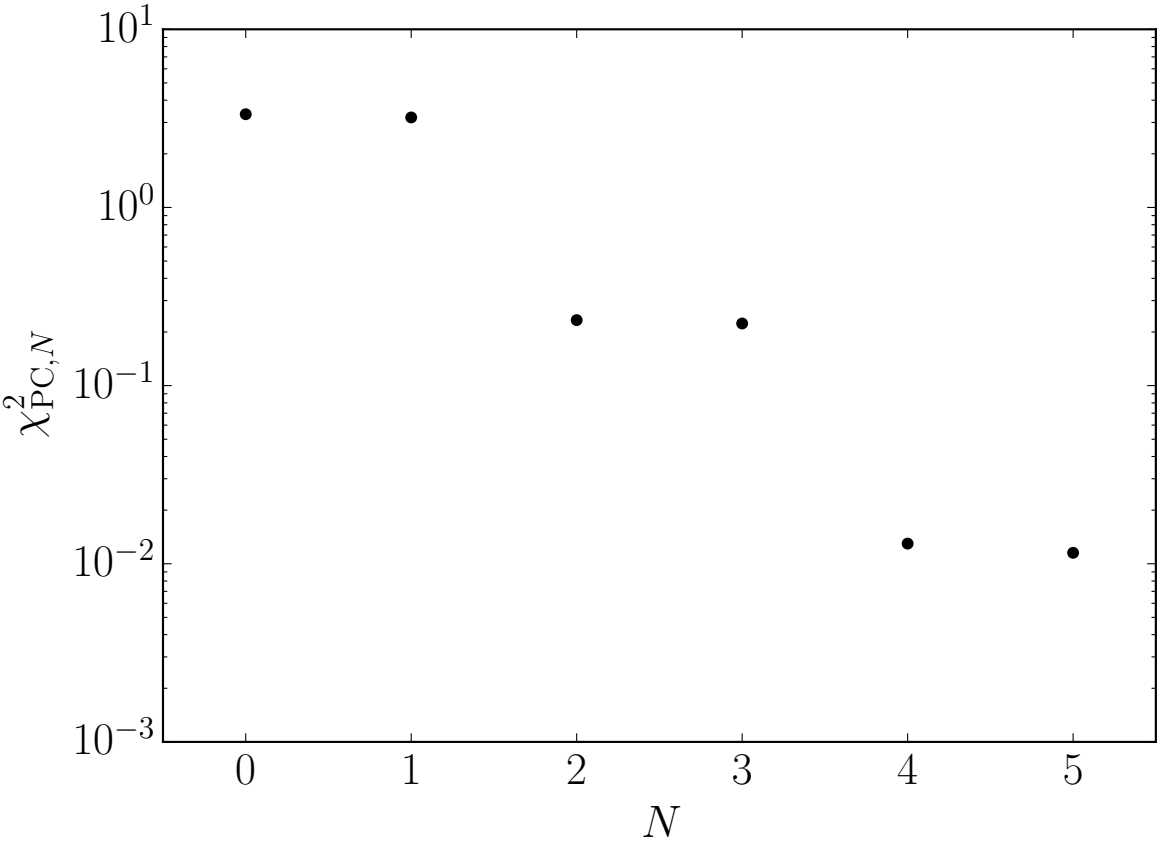

Figure C.2: Dependence of $\chi^2_{\mathrm{PC},N}$ (C.2), measure of error caused by approximating the lensing potential using first N principal component, on N. In this case $\Delta C_\ell^{\phi\phi}$ corresponds to parameter shifts listed in Tab. C.1.

REFERENCES

[1] Pavel Motloch, Wayne Hu, and Aurélien Benoit-Lévy. CMB Lens Sample Covariance and Consistency Relations. *Phys. Rev.*, D95(4):043518, 2017.

[2] Pavel Motloch and Wayne Hu. Lens covariance effects on likelihood analyses of CMB power spectra. *Phys. Rev.*, D96(10):103517, 2017.

[3] Pavel Motloch and Wayne Hu. Tensions between direct measurements of the lens power spectrum from Planck data. *Phys. Rev.*, D97:103536, 2018.

[4] Scott Dodelson. *Modern Cosmology*. Academic Press, Amsterdam, 2003.

[5] Antony Lewis and Anthony Challinor. Weak gravitational lensing of the cmb. *Phys. Rept.*, 429:1–65, 2006.

[6] A. G. Riess, S. Casertano, W. Yuan, L. Macri, J. Anderson, J. W. MacKenty, J. B. Bowers, K. I. Clubb, A. V. Filippenko, D. O. Jones, and B. E. Tucker. New Parallaxes of Galactic Cepheids from Spatially Scanning the Hubble Space Telescope: Implications for the Hubble Constant. *Astrophys. J.*, 855:136, March 2018.

[7] F. Koehlinger et al. KiDS-450: The tomographic weak lensing power spectrum and constraints on cosmological parameters. *Mon. Not. Roy. Astron. Soc.*, 471(4):4412–4435, 2017.

[8] R. Adam et al. Planck 2015 results. I. Overview of products and scientific results. *Astron. Astrophys.*, 594:A1, 2016.

[9] T. M. C. Abbott et al. Dark Energy Survey Year 1 Results: Cosmological Constraints from Galaxy Clustering and Weak Lensing. *arXiv*, astro-ph/1708.01530, 2017.

[10] Adam G. Riess et al. Observational evidence from supernovae for an accelerating universe and a cosmological constant. *Astron. J.*, 116:1009–1038, 1998.

[11] S. Perlmutter et al. Measurements of Omega and Lambda from 42 high redshift supernovae. *Astrophys. J.*, 517:565–586, 1999.

[12] Daniel Baumann. Inflation. In *Physics of the large and the small, TASI 09, proceedings of the Theoretical Advanced Study Institute in Elementary Particle Physics, Boulder, Colorado, USA, 1-26 June 2009*, pages 523–686, 2011.

[13] D. J. Fixsen. The Temperature of the Cosmic Microwave Background. *Astrophys. J.*, 707:916–920, 2009.

[14] Sudeep Das et al. Detection of the Power Spectrum of Cosmic Microwave Background Lensing by the Atacama Cosmology Telescope. *Phys. Rev. Lett.*, 107:021301, 2011.

[15] R. Keisler et al. A Measurement of the Damping Tail of the Cosmic Microwave Background Power Spectrum with the South Pole Telescope. *Astrophys. J.*, 743:28, 2011.

[16] P. A. R. Ade et al. BICEP2 / Keck Array VIII: Measurement of gravitational lensing from large-scale B-mode polarization. *Astrophys. J.*, 833(2):228, 2016.

[17] Blake D. Sherwin et al. Two-season Atacama Cosmology Telescope polarimeter lensing power spectrum. *Phys. Rev.*, D95(12):123529, 2017.

[18] P. A. R. Ade et al. Planck 2015 results. XV. Gravitational lensing. *Astron. Astrophys.*, 594:A15, 2016.

[19] Kendrick M. Smith, Oliver Zahn, and Olivier Dore. Detection of Gravitational Lensing in the Cosmic Microwave Background. *Phys. Rev.*, D76:043510, 2007.

[20] D. Hanson et al. Detection of B-mode Polarization in the Cosmic Microwave Background with Data from the South Pole Telescope. *Phys. Rev. Lett.*, 111(14):141301, 2013.

[21] R. Keisler et al. Measurements of Sub-degree B-mode Polarization in the Cosmic Microwave Background from 100 Square Degrees of SPTpol Data. *Astrophys. J.*, 807(2):151, 2015.

[22] Uros Seljak. Gravitational lensing effect on cosmic microwave background anisotropies: A Power spectrum approach. *Astrophys. J.*, 463:1, 1996.

[23] Matias Zaldarriaga. Lensing of the CMB: Non-Gaussian aspects. *Phys. Rev.*, D62:063510, 2000.

[24] Wayne Hu. Angular trispectrum of the CMB. *Phys. Rev.*, D64:083005, 2001.

[25] Wayne Hu and Takemi Okamoto. Mass reconstruction with cmb polarization. *Astrophys. J.*, 574:566–574, 2002.

[26] Kevork N. Abazajian et al. CMB-S4 Science Book, First Edition. *arXiv*, astro-ph/1610.02743, 2016.

[27] Takemi Okamoto and Wayne Hu. CMB lensing reconstruction on the full sky. *Phys. Rev.*, D67:083002, 2003.

[28] Christopher M. Hirata and Uros Seljak. Reconstruction of lensing from the cosmic microwave background polarization. *Phys. Rev.*, D68:083002, 2003.

[29] Kendrick M. Smith, Duncan Hanson, Marilena LoVerde, Christopher M. Hirata, and Oliver Zahn. Delensing CMB Polarization with External Datasets. *JCAP*, 1206:014, 2012.

[30] Marius Millea, Ethan Anderes, and Benjamin D. Wandelt. Bayesian delensing of CMB temperature and polarization. *arXiv*, astro-ph/1708.06753, 2017.

[31] Julien Carron and Antony Lewis. Maximum a posteriori CMB lensing reconstruction. *Phys. Rev.*, D96(6):063510, 2017.

[32] Marcel M. Schmittfull, Anthony Challinor, Duncan Hanson, and Antony Lewis. Joint analysis of CMB temperature and lensing-reconstruction power spectra. *Phys. Rev.*, D88(6):063012, 2013.

[33] Aurelien Benoit-Levy, Kendrick M. Smith, and Wayne Hu. Non-Gaussian structure of the lensed CMB power spectra covariance matrix. *Phys. Rev.*, D86:123008, 2012.

[34] L. Knox. Determination of inflationary observables by cosmic microwave background anisotropy experiments. *Phys. Rev. D*, 52:4307–4318, October 1995.

[35] Daniel Green, Joel Meyers, and Alexander van Engelen. CMB Delensing Beyond the B Modes. *JCAP*, 1712(12):005, 2017.

[36] Julien Peloton, Marcel Schmittfull, Antony Lewis, Julien Carron, and Oliver Zahn. Full covariance of CMB and lensing reconstruction power spectra. *Phys. Rev.*, D95(4):043508, 2017.

[37] Antony Lewis and Sarah Bridle. Cosmological parameters from cmb and other data: A monte carlo approach. *Phys. Rev. D*, 66:103511, Nov 2002.

[38] Kendrick M. Smith, Wayne Hu, and Manoj Kaplinghat. Weak lensing of the CMB: Sampling errors on B-modes. *Phys. Rev.*, D70:043002, 2004.

[39] Julien Peloton. private communication.

[40] Antony Lewis. Lensed CMB simulation and parameter estimation. *Phys. Rev.*, D71:083008, 2005.

[41] Antony Lewis and Sarah Bridle. Cosmological parameters from CMB and other data: A Monte Carlo approach. *Phys. Rev.*, D66:103511, 2002.

[42] Andrew Gelman and Donald B. Rubin. Inference from Iterative Simulation Using Multiple Sequences. *Statist. Sci.*, 7:457–472, 1992.

[43] Kendrick M. Smith, Wayne Hu, and Manoj Kaplinghat. Cosmological Information from Lensed CMB Power Spectra. *Phys. Rev.*, D74:123002, 2006.

[44] R. Adam et al. Planck intermediate results. XLVII. Planck constraints on reionization history. *Astron. Astrophys.*, 596:A108, 2016.

[45] Wayne Hu and Gilbert P. Holder. Model - independent reionization observables in the CMB. *Phys. Rev.*, D68:023001, 2003.

[46] Chen He Heinrich, Vinicius Miranda, and Wayne Hu. Complete Reionization Constraints from Planck 2015 Polarization. *Phys. Rev.*, D95(2):023513, 2017.

[47] R. Allison, P. Caucal, E. Calabrese, J. Dunkley, and T. Louis. Towards a cosmological neutrino mass detection. *Phys. Rev.*, D92(12):123535, 2015.

[48] J. Richard Bond. Signal-to-noise eigenmode analysis of the two year COBE maps. *Phys. Rev. Lett.*, 74:4369–4372, 1995.

[49] Emory F. Bunn and Naoshi Sugiyama. Cosmological constant cold dark matter models and the COBE two year sky maps. *Astrophys. J.*, 446:49, 1995.

[50] Michael S. Vogeley and Alexander S. Szalay. Eigenmode analysis of galaxy redshift surveys I. theory and methods. *Astrophys. J.*, 465:34–53, 1996.

[51] P. A. R. Ade et al. Planck 2013 results. XVI. Cosmological parameters. *Astron. Astrophys.*, 571:A16, 2014.

[52] P. A. R. Ade et al. Planck 2015 results. XIII. Cosmological parameters. *Astron. Astrophys.*, 594:A13, 2016.

[53] N. Aghanim et al. Planck intermediate results. LI. Features in the cosmic microwave background temperature power spectrum and shifts in cosmological parameters. *Astron. Astrophys.*, 607:A95, 2017.

[54] Georges Obied, Cora Dvorkin, Chen Heinrich, Wayne Hu, and Vinicius Miranda. Inflationary Features and Shifts in Cosmological Parameters from Planck 2015 Data. *Phys. Rev.*, D96(8):083526, 2017.

[55] G. E. Addison, Y. Huang, D. J. Watts, C. L. Bennett, M. Halpern, G. Hinshaw, and J. L. Weiland. Quantifying discordance in the 2015 Planck CMB spectrum. *Astrophys. J.*, 818(2):132, 2016.

[56] S. Kullback and R. A. Leibler. On information and sufficiency. *Ann. Math. Statist.*, 22(1):79–86, 03 1951.

[57] Krzysztof M. Gorski, Benjamin D. Wandelt, Frode K. Hansen, Eric Hivon, and Anthony J. Banday. The healpix primer. *arXiv*, astro-ph/9905275, 1999.